MOLECULAR ASPECTS OF FLOW-INDUCED CRYSTALLIZATION OF POLYPROPYLENE

Thesis by

Derek W. Thurman

In Partial Fulfillment of the Requirements for the

degree of

Doctor of Philosophy

CALIFORNIA INSTITUTE OF TECHNOLOGY

Pasadena, California

2006

(Defended November 29, 2005)

ACKNOWLEDGEMENTS

In the process of writing this thesis, I have taken the occasion to reflect upon my years of graduate study, as I imagine many scholars do. Several things stand out prominently amongst my memories: graduate school was much more intellectually and emotionally challenging than all my previous scholastic endeavors, I have never been surrounded by so many intelligent people, the weather in southern California is amazing, and never ship UPS. I am appreciative for all my experiences at Caltech, pleasant or otherwise, since it is not the events in life that shape our character but rather our reaction to them. I owe a debt of gratitude to each of those who influenced my outlook on life during the past six years (and beyond).

I will begin by recounting a pivotal moment in my education that initiated my pursuit of chemical science. My high school chemistry teacher pulled me aside one day during my senior year and inquired about my plans for a major field of study in college. He suggested that with an aptitude for math and science I should consider the study of chemistry and sent me on my way. I left that conversation with two things: a Troy ounce of silver pressed into a commemorative coin (a gift given to each of his senior students) and a direction for my intellectual pursuits. Mr. Powell, I have held on to both of those gifts to this day.

I was also greatly influenced by my undergraduate chemistry professors at Abilene Christian University: Dr. Eric Hardegree, Dr. Perry Reeves, Dr. Kim Pamplin, Dr. Charles Garner, and my research advisor, Dr. Greg Powell. I was so lucky to attend an institution where the professors take a personal interest in their students and maintain those relationships. Each of them contributed to my understanding of chemistry while fostering an appreciation for a balanced and thoughtful life enriched by more than career and intellectual pursuits.

I would like to acknowledge members of my research group and collaborators who have been particularly helpful during my time at Caltech: Guru Kumaraswamy, a previous graduate student who designed and built the apparatus that made my research possible; Jim Oberhauser, a post-doc who was invaluable during the beginning of my research; Motohiro

Seki, a visiting scientist from Mitsubishi Chemical Company who inspired in me a great appreciation for the Japanese people; Matt Moffitt, a post-doc collaborator from the University of Toronto; J.-P. Autran from Procter & Gamble, a valuable collaborative resource and supportive colleague; and Lucia Fernandez Ballester, a fellow grad student who has toiled beside me on the crystallization project for more than 4 years while graciously enduring a total of 75 days with me at the synchrotron. I would also like to thank all other group members, past and present, who may not have directly contributed to my research but generally made life in the Kornfield lab more enjoyable: Weijun Zhou, Giyoong Tae, Hee Hyun Lee, Mike Kempe, Wei Shen, Maria Lujan Auad, Rob Lammertink, Fred Tessier, Erica Thompson, Charles Nickerson, Rafael Verduzco, Mike Mackel, Matt Mattson, Ameri David, Suneel Kunamaneni, Ryan Turner, and Zuli Kurji. A special thanks to my officemates, Eric Pape and Neal Scruggs, who spent many hours discussing topics ranging from high tech to low brow.

I would not have gone far without the help of our group secretary, Anne Hormann. Her hard work, organization, and willingness to listening to my uninformed questions have never ceased to amaze me.

I am thankful for each of the members of my thesis committee for their willingness to consider my research and read my thesis: John Bercaw, Robert Grubbs, and William Goddard. I am especially grateful for my thesis advisor, Julia Kornfield. Her keen insight and ability to interpret data to reveal the underlying physical events have been a great boon to my research. Her high standards in research and writing have driven me to become a more clear and efficient communicator. If I had to do it all over, I would be glad to choose her group again.

The most influential people in my life are my parents. Their love and support has been unwavering. They always believed in me. Thanks, Mom and Dad.

Finally, I would like to thank my beautiful wife, Megan, for her patience and support. She has been so gracious during the sprint finish of my graduate school marathon. She has brought balance and perspective, always pointing me toward the final goal.

ABSTRACT

Polyolefins, semicrystalline polymers also known as thermoplastics, are highly desirable because of their material properties, low cost, and ease in processing. The flow and thermal history experienced during processing are known to affect dramatic changes in crystalline kinetics and morphology, dictating the final material properties of solidified products. However, the underlying physics that control crystalline orientation and kinetics is not well understood. To optimize processing conditions and maximize material performance, it is desirable to understand how the interplay of molecular character and flow conditions shape crystalline microstructure.

In the last decade, advances in catalyst technology have produced well defined materials enabling the systematic study of molecular influences on flow-induced crystallization. We investigate bimodal blends of polypropylenes (PP) in which we vary the molecular character (concentration, molecular weight, regularity) of the high molecular weight mode. We apply a number of *in situ* characterization tools (rheo-optics, rheo-WAXD) to the development of transient structure and interpret our findings in light of *ex situ* examination (polarized light microscopy, TEM) of the final morphology.

Blending a well-characterized high molecular weight isotactic polypropylene into a “base iPP” at various concentrations (c), we determined that blends with less than 1% of chains with M_w five times larger than the M_w of the base resin profoundly affected the crystallization kinetics and crystalline morphology of a sheared melt. Beyond unambiguously demonstrating the important role of long chains in the formation of anisotropic crystallization under flow, this approach allowed us to be specific about the length that is meant by “long chains” and the concentration of these chains in the melt. Varying the concentration from below to above c^* revealed that the effect of the long chains involves cooperative interactions, evident in the non-linear relationship of the long chain concentration, particularly as c approaches the long chain-long chain overlap concentration. The long chains greatly enhance the formation of threadlike precursors but only mildly enhance the formation of pointlike precursors.

In studying a series of blends in which the M_w of the long chain mode was varied, we found that increasing the M_w of the long chain portion of a bimodal blend increased the tendency to form threadlike precursors to oriented crystallization. This was highlighted by a marked decrease in the threshold stress necessary to induce oriented crystalline growth and is related to the separation in time scales between the slowest relaxing chains and the average. Thus, the propagation of shish varies strongly with the separation in time scales between the slowest relaxing chains and the average. Below a threshold ratio of relaxation times ($\tau_L/\tau_S \sim 100$) addition of long chains did not change the behavior from that of Base-PP itself.

Our analysis of real-time rheo-optical and rheo-WAXD experiments combined with depth dependent information from a novel “depth sectioning” analysis technique uncovers several keys to understanding how anisotropic crystallization is induced by flow. Threads first form near the channel wall, where stress is highest, and grow in length with prolonged flow. After sufficient time, thread length per unit volume saturates, perhaps due to collisions with other threads or crystalline overgrowth from those threads. Prior to saturation, when crystalline overgrowth is negligible, the thread propagation appears to be linear with shearing time. The propagation of threads varies in a nonlinear manner with stress. Finally, we identify a promising set of conditions that can be used to measure the thread propagation velocity for this material if the appropriate length scale can be assigned by microscopy.

We examined the effects of long chain regularity on the formation of threadlike precursors, showing that addition of molecular level defects to the high end of the molecular weight distribution effectively raises the threshold stress and mitigates the formation of oriented precursors induced by flow. Our study included a model bimodal blend of isotactic and atactic polypropylene as well as large scale bimodal blends of isotactic polypropylene and a propylene-ethylene copolymer fit for pilot-scale production of nonwoven fabrics. It is noteworthy that the qualitative behavior observed in the melt-spinning process accords well with the trends evident in isothermal shear-induced crystallization. This has value in two respects. Scientifically, it is significant that idealized flow and thermal conditions may well

reveal the physics relevant to polymer processing, which involves mixed shear and extension under non-isothermal conditions. Technologically, the ability to screen different resin compositions on a small scale can be used to optimize flow-induced crystallization characteristics prior to scale up.

TABLE OF CONTENTS

LIST OF TABLES

LIST OF ILLUSTRATIONS

1 INTRODUCTION

1.1 Background

In the early 1950's, Karl Ziegler[1] and Giulio Natta[2] launched the modern polyolefin industry with the discovery and development of catalyst-driven polymerization of olefins, a feat for which they shared the Nobel Prize for Chemistry in 1963. The development of a completely synthetic, re-formable material was a boon to the nascent polymers industry, which relied heavily on natural products (e.g., rubber, gutta percha, and celluloid) and hard phenolic resins.[3] Today, representing about 60% (24 million tons) of the polymer produced annually in the U.S.,[4] polyolefins are the most widely used polymeric materials due to excellent physical properties, easy processibility, recyclability, and low cost. Polyethylene and polypropylene, the most common polyolefins, are used in products ranging from car bumpers to carpet fibers to artificial joints, and are fabricated by a variety of methods including injection molding, fiber drawing, thermoforming, and extrusion. Widespread commercial usage of polyolefins has motivated studies to understand the processing-structure-property relationships of these materials to optimize control of product material properties.

Polyolefins belong to a class of polymers known as thermoplastics, which can be melted and reformed due to their semicrystalline nature. This characteristic leads to an ease in processing that, in part, is responsible for their widespread use. The semicrystalline nature of polyolefins naturally leads to a composite structure in which crystalline portions impart strength and amorphous portions impart toughness. The material properties such as

strength, hardness, and permeability are linked to microstructural characteristics—crystallite orientation and organization—known to vary in a highly non-linear way in response to flow. Dramatic improvements in material properties can be achieved during processing by controlling crystalline microstructure. For example, Dyneema®, a highly oriented polyethylene fiber, has a modulus of 116 GPa (modulus of steel is 200 GPa), but the modulus of unoriented polyethylene is < 10 GPa. Furthermore, recent improvements in catalyst technologies enable exceptional control over molecular characteristics (molecular weight, molecular weight distribution, tacticity, comonomer incorporation) of polyolefins—the primary molecular parameters that affect crystallization. However, the complex interplay between processing conditions and molecular characteristics that determines the final crystalline microstructure in not well understood. It is our goal to elucidate the underlying physics controlling flow-induced crystallization of semicrystalline polymers.

1.1.1 Morphology and nucleation in quiescent polymer crystallization

Semicrystallinity is a consequence of the key feature that distinguishes polymers from small molecules—connectivity. Flexible chain polymers of simple monomer units that are covalently bonded to form macromolecules can be millions of units long. This connectivity has consequences for crystallization. Unlike small molecules which add sequentially to a molecular crystal arrangement in space leading to 3-dimensional crystal growth up to the macroscopic scale, polymers are unlikely to form such an arrangement due to the size of each molecule. Rather, polymer chains fold back and forth forming platelet-like crystals which extend in only two dimensions. The third dimension established by the fold length (5 – 20 nm) remains more or less constant. The chain-folding habit of polymer crystallization was determined by Keller[5] upon examining single crystals of polyethylene grown from dilute solution. These chain-folded crystals (also known as chain-folded lamellae) are a metastable structure (though at least one researcher[6] has challenged this assumption) adopted by the polymers since the thermodynamic equilibrium crystalline structure, composed of fully extended chain crystals, is kinetically frustrated. Because chain folding is a kinetically controlled process, many chains are unable to re-enter (or are rejected from) the lamellar crystal and may span multiple lamellae, participating in several crystals. This

is even more likely when crystallization proceeds in bulk from the melt state where polymer chains are highly entangled and must disentangle to participate in crystallites. The interlamellar portions of the chains remain amorphous and may represent 10 – 70% of the polymeric material.

During bulk crystallization from the melt in the absence of external perturbation, polymers tend to form spherical super structures known as "spherulites."[7,8] Spherulites result from branching and splaying of lamellae as they grow outward from a nucleus to fill space. The spherulite structures are easily analyzed with optical microscopy, yielding information on the inherent nucleation and growth rate of the polymer (Figure 1.1). Much of the early knowledge concerning crystallization kinetics and morphology was obtained in this way.

According to classical nucleation theory, quiescent crystallization of polymers begins when statistical thermal fluctuations in chain conformation and arrangement within a metastable, supercooled phase produce a critical-sized nucleus of the crystalline phase followed by growth into a new macroscopic phase. This growth is spontaneous when the size of the nucleus is large enough to balance the bulk free energy gain against the free energy cost of creating a new interface. Smaller nuclei rapidly destabilize. However, there is substantial debate concerning the earliest events of polymer crystallization, with several investigators challenging nucleation and growth as the origin of crystallites. Terrill, et al.[9] and Olmsted, et al.[10] reported SAXS experiments of crystallizing polypropylene, suggesting that the nucleation step actually resembled a spontaneous, liquid-liquid spinodal decomposition, a term that describes a completely different method of phase-separation in which the unstable phase continuously and cooperatively reorganizes on longer length scales than the nucleus. Strobl[11] cited Olmsted and Terrill when proposing that polymer crystallization closely resembles ordering in 2-D systems that grow cooperatively via intermediate states: a mesomorphic layer that thickens into a granular layer of crystalline blocks that finally merge into lamellar crystals. Muthukumar[12] contends that classical nucleation and growth can explain all experimental observations cited by the previous investigators (though the controversy continues), but points out that situation is further complicated when an external flow field is applied during crystallization.

1.1.2 Flow-induced morphology and nucleation in polymer crystallization

The morphology, or structural arrangement, of the crystallites is greatly influenced by the conditions of crystallization. In the presence of a flow field, anisotropic nucleation is known to produce highly oriented crystallites. Early studies of stirred polymer solutions by Pennings[13] uncovered a structure commonly referred to as a "shish-kebab." Conventionally, it is thought to consist of a central crystalline core of extended chain crystals ("shish") decorated with radially growing chain-folded lamellar crystals ("kebabs"). Appearance of an analogous "row-nucleated" structure[14-16] is well-established for bulk crystallization from the melt in both strong[14,17-19] (extensional) and weak[20-22] (shear) flows (Figure 1.2). However, the very nature of the shish or threadlike nuclei (crystalline,[17,22] amorphous,[23] smectic[24-28]) is not well understood and remains a topic of interest and debate.

It is well known that in polymer crystallization, flow enhances both the rate and anisotropy of nucleation. No satisfactory molecular theory currently exists to explain the mechanism by which flow induces nucleation. Flory[29] attributed enhanced nucleation to a reduction in entropy of the melt due to segmental orientation, leading to an increase in the melting point and thus an effective increase in the subcooling. However, this does not fully account for the experimentally observed increase in crystallization kinetics[30] nor does it attempt to explain morphological changes. Keller[31] contended that a coil-stretch[32] transition for the longest chains led to formation of extended chain crystalline nuclei when coiled chains fully extended. His work focused on extensional flows and cannot explain the dramatic effects induced even by "weak flows" (such as shear) where chain extension is unlikely. Janeschitz-Kriegl[33] posited the idea that dormant "athermal" nuclei in quiescent melts, nuclei whose number density is a function of temperature but not time, are activated as clusters coalesce during flow leading to threadlike precursors. More recently, Li and de Jeu[24-26] asserted that crystallization under flow proceeds via a pre-ordering of the melt into layers of pseudo-crystalline bundles of chains with smectic ordering reminiscent of Strobl's[11] description of quiescent crystallization. No clear consensus exists concerning the nature of oriented nuclei or the mechanism(s) by which they are fashioned.

1.1.3 State of knowledge concerning molecular effects on crystallization

Understanding how molecular characteristics of polymers affect crystallization will enable rational design of polymer resin molecular characteristics to exploit processing-structure-properties relationships. However, little is known concerning molecular variables, in large part because of ill-defined polymers that were studied. Until recently, heterogeneous Ziegler-Natta type catalysts used to produce commonly studied polymers (polyethylene and polypropylene) yielded materials with a broad distribution of both molecular weights and molecular defects. Furthermore, the distribution of molecular defects is linked to molecular weight such that the longest chains are the most perfect and the shortest chains contain the most defects.

In the literature, a long-standing hypothesis has held that a broad distribution of molecular weights and the high molecular weight tail, in particular, are responsible for the dramatic crystallization effects in deformed systems.[13,34-39] It is commonly believed that the long relaxation time of the longest chains relative to the bulk of shorter chains leads to preferential orientation under flow and the growth of highly anisotropic crystallites. Yet, the broad distribution of molecular weights prevented determination of which chains should be considered "long," and it remained unclear whether long chains enhanced crystallization because of length or because of regularity. Chain regularity (tacticity, comonomer content) is known to strongly affect degree of crystallinity, crystallization kinetics, and morphology.[40-43]

1.2 Motivation

Study of flow-enhanced crystallization dates back to the 1960s,[34,35,44-48] but the problem has regained considerable attention in the past decade[20,21,36,49-57] due, in part, to the advancements in single-site catalysts[58,59] which offer unprecedented control of polymer molecular properties. Metallocene catalysts produce polymers with a narrow distribution of molecular weights (M_w/M_n ~ 2) compared to heterogeneous catalysts (M_w/M_n ~ 4-6) and yield an even distribution of defects over all molecular weights. For polypropylene, the symmetry between adjacent methyl substituents, or tacticity, can be varied from random to

nearly perfect. Such control over molecular variables enables a systematic approach to the study of flow-induced crystallization.

Polypropylene has garnered attention particularly in the crystallization literature due to properties amenable to experimentation: ready availability in linear form (polyethylene tends to form branches), a wide crystallization temperature window, and moderate crystallization kinetics. Furthermore, there exists substantial interest from an industrial perspective. Polypropylene has gained the largest share of the plastics market[4] since it exhibits properties that are more desirable than polyolefin relatives: polyethylene, polyvinyl chloride, and others. Polypropylene has a higher melting point, lower density, good chemical resistance, and lower cost. Great effort is directed toward expanding the market for polypropylene and improving its processing characteristics. The crystallization kinetics of iPP are slow relative to PE, increasing technological motivation to understand the ways that molecular structure and processing flow can be used together to produce rapid solidification and hence high throughput production. To be used in the widest range of processes, polypropylene materials are tailored for processing by modification of the molecular weight, molecular weight distribution, tacticity, comonomer content, and chain architecture through trial and error methods.

The ultimate goal of studies of flow-induced crystallization is the development of a truly predictive model requiring only molecular characteristics of the polymer and flow conditions as parameters. A successful model would predict relevant crystalline characteristics such as degree of crystallization, kinetics, orientation, morphology, and material properties. Such a model does not exist. A number of empirical models[60-63] of flow-induced crystallization have been formulated which rely on adjustable parameters that are used to fit limited experimental data, do not account for morphology, and generally calculate only one pertinent value (i.e., onset of crystallization, degree of crystallization). Guided by experimental findings, recent models of flow-induced crystallization have begun to focus on molecular dynamics in the melt using rheological approaches to predict the effects of high molecular weight chains on crystallization kinetics[64,65] and morphology.[66] The dramatic influence of anisotropic nucleation upon crystallization kinetics, structure,

and ultimate material properties suggests that successful models must include the physics of oriented threadlike precursor formation. However, a solid understanding of those physics must first be discovered, motivating the design of our experiments to track the formation of oriented precursors.

Our research aims to elucidate the molecular physics that underlie flow-induced crystallization by systematic variation of molecular parameters of polypropylene. Our strategy for unraveling the molecular aspects of flow-induced crystallization begins with the hypothesis that the longest chains are responsible for the induction of highly oriented crystallites. Model blends of polypropylenes with a bimodal distribution of molecular weights in which the length and amount of long chains are known, and the molecular regularity of the long component that can be systematically varied are examined. We focus on polypropylene, in particular, but are hopeful that insights from its study will be applicable to other semicrystalline polymers and will ultimately provide a more complete perspective of flow-induced crystallization events.

1.3 Thesis organization

We begin by introducing the novel device developed for well-defined flow-induced crystallization studies and the methodology applied (Chapter 2). Next, we test and confirm the hypothesis that long chains enhance the formation of anisotropic crystals by adding small amounts of high molecular weight polypropylene to a base resin, looking particularly at how its effects vary at concentrations where the long chains begin to overlap (Chapter 3). To clarify how long chains promote the transition to oriented crystalline growth, the subsequent chapters describe the effect of the relative length of the long chains to the short chains (M_L/M_S) on the threshold stress to induce oriented crystallization, σ^* (Chapter 4); the relative thread length per unit volume as a function of the local stress, $\sigma - \sigma^*$ (Chapter 5); and the effect of long chain regularity on the formation of threadlike precursors (Chapter 6).

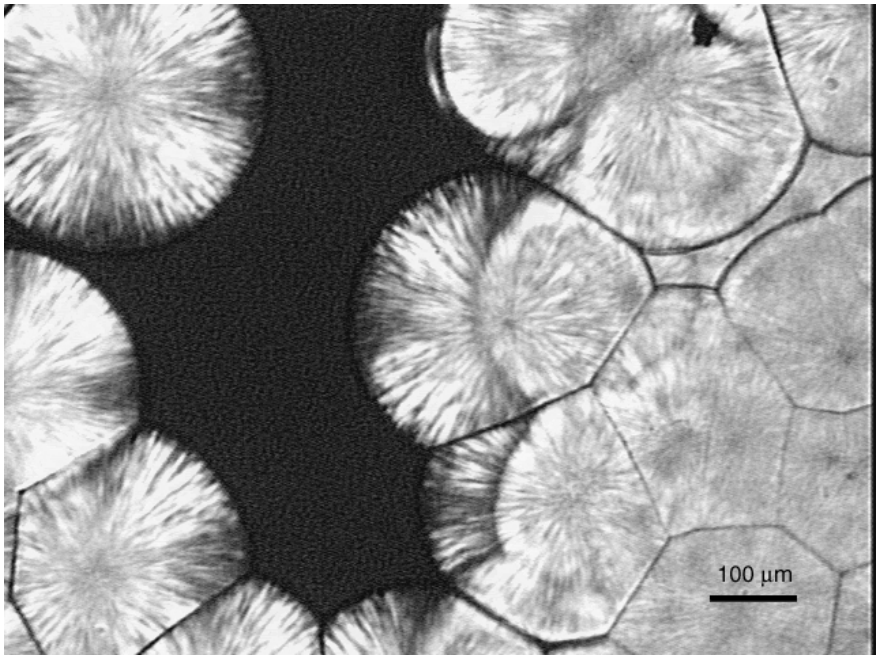

Figure 1.1: Polarized light micrograph of spherulites in an isotactic polypropylene impinging upon one another. Scale bar 100 μm.

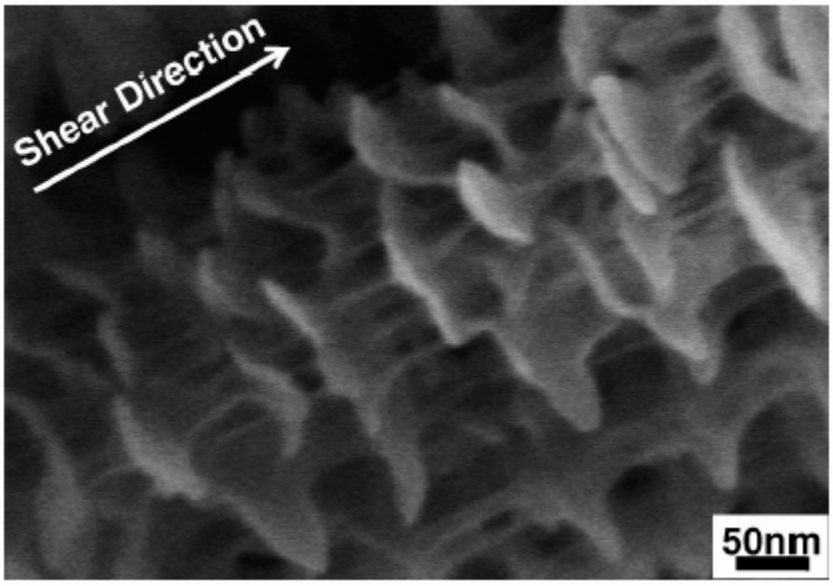

Figure 1.2: Scanning electron micrograph of toluene-extracted ultra high molecular weight polyethylene crystallites with a shish-kebab structure following shear treatment. (Reprinted with permission from Hsiao, B.S., et al. Phys. Rev. Lett. 2005; 94 (11): 117802. Copyright (2005) by the American Physical Society).

3.6 Bibliography

1. Ziegler, K.; E. Holzkamp; H. Breil, and H. Martin, "*The Mulheim Normal Pressure Polyethylene Process." Angewandte Chemie-International Edition*, **1955**. *67*: 541-47.
2. Natta, G.; P. Pino; P. Corradini; F. Danusso; E. Mantica; G. Mazzanti, and G. Moraglio, "*Crystalline High Polymers of Alpha-Olefins." Journal of the American Chemical Society*, **1955**. *77*: 1708-10.
3. Mossman, S.T. and P.J. Morris, eds. *The Development of Plastics*. 1994, The Royal Society of Chemistry: London. 120.
4. Pasquini, N., ed. *Polypropylene Handbook*. 2nd ed. 2005, Hanser Gardner Publications, Inc.: Cincinnati. 584.
5. Keller, A., "*A Note on Single Crystals in Polymers - Evidence for a Folded Chain Configuration." Philosophical Magazine*, **1957**. *2*: 1171-&.
6. Muthukumar, M., "*Molecular modelling of nucleation in polymers." Philosophical Transactions of the Royal Society of London Series a-Mathematical Physical and Engineering Sciences*, **2003**. *361*: 539-54.
7. Padden, F.J. and H.D. Keith, "*Spherulitic Crystallization in Polypropylene." Journal of Applied Physics*, **1959**. *30*: 1479-84.
8. Keith, H.D. and F.J. Padden, "*The Optical Behavior of Spherulites in Crystalline Polymers .2. The Growth and Structure of the Spherulites." Journal of Polymer Science*, **1959**. *39*: 123-38.
9. Terrill, N.J.; P.A. Fairclough; E. Towns-Andrews; B.U. Komanschek; R.J. Young, and A.J. Ryan, "*Density fluctuations: the nucleation event in isotactic polypropylene crystallization." Polymer*, **1998**. *39*: 2381-85.
10. Olmsted, P.D.; W.C.K. Poon; T.C.B. McLeish; N.J. Terrill, and A.J. Ryan, "*Spinodal-assisted crystallization in polymer melts." Physical Review Letters*, **1998**. *81*: 373-76.
11. Strobl, G., "*From the melt via mesomorphic and granular crystalline layers to lamellar crystallites: A major route followed in polymer crystallization?" European Physical Journal E*, **2000**. *3*: 165-83.
12. Muthukumar, M., "*Commentary on theories of polymer crystallization." European Physical Journal E*, **2000**. *3*: 199-202.
13. Pennings, A.J. and A.M. Kiel, "*Fractionation of Polymers by Crystallization from Solution .3. On Morphology of Fibrillar Polyethylene Crystals Grown in Solution." Kolloid-Zeitschrift and Zeitschrift Fur Polymere*, **1965**. *205*: 160-&.
14. Keller, A., "*Unusual Orientation Phenomena in Polyethylene Interpreted in Terms of the Morphology." Journal of Polymer Science*, **1955**. *15*: 31-49.
15. Monks, A.W.; H.M. White, and D.C. Bassett, "*On shish-kebab morphologies in crystalline polymers." Polymer*, **1996**. *37*: 5933-36.
16. White, H.M. and D.C. Bassett, "*On row structures, secondary nucleation and continuity in alpha-polypropylene." Polymer*, **1998**. *39*: 3211-19.
17. Keller, A. and H.W.H. Kolnaar, *Flow-Induced Orientation and Structure Formation*, in *Processing of Polymers*, H.E.H. Meijer, Editor. 1997, Wiley-VCH: New York. p. 189-268.

18. Hill, M.J. and A. Keller, "*Further Studies on Polyethylene Crystallized under Stress - Morphology, Calorimetry, and Stress Relaxation." Journal of Macromolecular Science-Physics*, **1971**. *B 5*: 591-&.
19. Hill, M.J. and A. Keller, "*Direct Evidence for Distinctive, Stress-Induced Nucleus Crystals in Crystallization of Oriented Polymer Melts." Journal of Macromolecular Science-Physics*, **1969**. *B 3*: 153-&.
20. Kumaraswamy, G.; R.K. Verma; A.M. Issaian; P. Wang; J.A. Kornfield; F. Yeh; B.S. Hsiao, and R.H. Olley, "*Shear-enhanced crystallization in isotactic polypropylene Part 2. Analysis of the formation of the oriented "skin"." Polymer*, **2000**. *41*: 8931-40.
21. Seki, M.; D.W. Thurman; J.P. Oberhauser, and J.A. Kornfield, "*Shear-mediated crystallization of isotactic polypropylene: The role of long chain-long chain overlap." Macromolecules*, **2002**. *35*: 2583-94.
22. Hsiao, B.S.; L. Yang; R.H. Somani; C.A. Avila-Orta, and L. Zhu, "*Unexpected shish-kebab structure in a sheared polyethylene melt." Physical Review Letters*, **2005**. *94*.
23. Somani, R.H.; L. Yang; I. Sics; B.S. Hsiao; N.V. Pogodina; H.H. Winter; P. Agarwal; H. Fruitwala, and A. Tsou, "*Orientation-induced crystallization in isotactic polypropylene melt by shear deformation." Macromolecular Symposia*, **2002**. *185*: 105-17.
24. Li, L.B. and W.H. de Jeu, "*Shear-induced smectic ordering as a precursor of crystallization in isotactic polypropylene." Macromolecules*, **2003**. *36*: 4862-67.
25. Li, L.B. and W.H. de Jeu, "*Shear-induced smectic ordering in the melt of isotactic polypropylene." Physical Review Letters*, **2004**. *92*.
26. Li, L.B. and W.H. de Jeu, "*Shear-induced smectic ordering and crystallisation of isotactic polypropylene." Faraday Discussions*, **2005**. *128*: 299-319.
27. Somani, R.H.; L. Yang; B.S. Hsiao; P.K. Agarwal; H.A. Fruitwala, and A.H. Tsou, "*Shear-induced precursor structures in isotactic polypropylene melt by in-situ rheo-SAXS and rheo-WAXD studies." Macromolecules*, **2002**. *35*: 9096-104.
28. Somani, R.H.; L. Yang; B.S. Hsiao, and H. Fruitwala, "*Nature of shear-induced primary nuclei in iPP melt." Journal of Macromolecular Science-Physics*, **2003**. *B42*: 515-31.
29. Flory, P.J., "*Thermodynamics of Crystallization in High Polymers .1. Crystallization Induced by Stretching." Journal of Chemical Physics*, **1947**. *15*: 397-408.
30. McHugh, A.J.; R.K. Guy, and D.A. Tree, "*Extensional Flow-Induced Crystallization of a Polyethylene Melt." Colloid and Polymer Science*, **1993**. *271*: 629-45.
31. Meijer, H.E.H., ed. *Processing of Polymers*. Materials Science and Technology: A Comprehensive Treatment, ed. R.W.H. Cahn, P.; Kramer, E.J. Vol. 18. 1997, Wiley-VCH: New York. 787.
32. Pope, D.P. and A. Keller, "*Study of Chain Extending Effect of Elongational Flow in Polymer-Solutions." Colloid and Polymer Science*, **1978**. *256*: 751-56.
33. Janeschitz-Kriegl, H.; E. Ratajski, and H. Wippel, "*The physics of athermal nuclei in polymer crystallization." Colloid and Polymer Science*, **1999**. *277*: 217-26.

34. Haas, T.W. and B. Maxwell, "*Effects of Shear Stress on Crystallization of Linear Polyethylene and Polybutene-1." Polymer Engineering and Science*, **1969**. *9*: 225-&.
35. Andersen, P.G. and S.H. Carr, "*Crystal Nucleation in Sheared Polymer Melts." Polymer Engineering and Science*, **1978**. *18*: 215-21.
36. Vleeshouwers, S. and H.E.H. Meijer, "*A rheological study of shear induced crystallization." Rheologica Acta*, **1996**. *35*: 391-99.
37. Somani, R.H.; B.S. Hsiao; A. Nogales; S. Srinivas; A.H. Tsou; I. Sics; F.J. Balta-Calleja, and T.A. Ezquerra, "*Structure development during shear flow-induced crystallization of i-PP: In-situ small-angle X-ray scattering study." Macromolecules*, **2000**. *33*: 9385-94.
38. Duplay, C.; B. Monasse; J.M. Haudin, and J.L. Costa, "*Shear-induced crystallization of polypropylene: Influence of molecular weight." Journal of Materials Science*, **2000**. *35*: 6093-103.
39. Hoffman, J.D., "*Formation of Polymer Fibrils by Flow-Induced Crystallization." Polymer*, **1979**. *20*: 1071-77.
40. Bond, E.B. and J.E. Spruiell, "*The effects of atacticity, comonomer content, and configurational defects on the equilibrium melting temperature of monoclinic isotactic polypropylene." Journal of Applied Polymer Science*, **2001**. *81*: 229-36.
41. Janimak, J.J.; S.Z.D. Cheng; A.Q. Zhang, and E.T. Hsieh, "*Isotacticity Effect on Crystallization and Melting in Polypropylene Fractions .3. Overall Crystallization and Melting Behavior." Polymer*, **1992**. *33*: 728-35.
42. Janimak, J.J.; S.Z.D. Cheng; P.A. Giusti, and E.T. Hsieh, "*Isotacticity Effect on Crystallization and Melting in Poly(Propylene) Fractions .2. Linear Crystal-Growth Rate and Morphology Study." Macromolecules*, **1991**. *24*: 2253-60.
43. Cheng, S.Z.D.; J.J. Janimak; A.Q. Zhang, and E.T. Hsieh, "*Isotacticity Effect on Crystallization and Melting in Polypropylene Fractions .1. Crystalline-Structures and Thermodynamic Property Changes." Polymer*, **1991**. *32*: 648-55.
44. Wereta, A. and C.G. Gogos, "*Crystallization Studies on Deformed Polybutene-1 Melts." Polymer Engineering and Science*, **1971**. *11*: 19-&.
45. Stein, R.S., "*Optical Studies of Stress-Induced Crystallization of Polymers." Polymer Engineering and Science*, **1976**. *16*: 152-57.
46. Wolkowicz, M.D., "*Nucleation and Crystal-Growth in Sheared Poly(1-Butene) Melts." Journal of Polymer Science Part C-Polymer Symposium*, **1977**: 365-82.
47. Fritzsche, A.K.; F.P. Price, and R.D. Ulrich, "*Disruptive Processes in Shear Crystallization of Poly(Ethylene Oxide)." Polymer Engineering and Science*, **1976**. *16*: 182-88.
48. Lagasse, R.R. and B. Maxwell, "*Experimental-Study of Kinetics of Polymer Crystallization During Shear-Flow." Polymer Engineering and Science*, **1976**. *16*: 189-99.
49. Janeschitzkriegl, H.; S. Liedauer; H. Wippel, and G. Eder, "*Influences of Flow and Heat-Transfer Conditions on the Solidification of Polymers by Crystallization." International Journal of Polymeric Materials*, **1993**. *20*: 213-21.

50. Liedauer, S.; G. Eder, and H. Janeschitzkriegl, "*On the Limitations of Shear-Induced Crystallization in Polypropylene Melts." International Polymer Processing*, **1995**. *10*: 243-50.
51. Liedauer, S.; G. Eder; H. Janeschitzkriegl; P. Jerschow; W. Geymayer, and E. Ingolic, "*On the Kinetics of Shear-Induced Crystallization in Polypropylene." International Polymer Processing*, **1993**. *8*: 236-44.
52. Jerschow, P. and H. JaneschitzKriegl, "*On the development of oblong particles as precursors for polymer crystallization from shear flow: Origin of the so-called fine grained layers." Rheologica Acta*, **1996**. *35*: 127-33.
53. Jerschow, P. and H. JaneschitzKriegl, "*The role of long molecules and nucleating agents in shear induced crystallization of isotactic polypropylenes." International Polymer Processing*, **1997**. *12*: 72-77.
54. Kumaraswamy, G.; A.M. Issaian, and J.A. Kornfield, "*Shear-enhanced crystallization in isotactic polypropylene. 1. Correspondence between in situ rheo-optics and ex situ structure determination." Macromolecules*, **1999**. *32*: 7537-47.
55. Kumaraswamy, G.; J.A. Kornfield; F.J. Yeh, and B.S. Hsiao, "*Shear-enhanced crystallization in isotactic polypropylene. 3. Evidence for a kinetic pathway to nucleation." Macromolecules*, **2002**. *35*: 1762-69.
56. Kumaraswamy, G.; R.K. Verma, and J.A. Kornfield, "*Novel flow apparatus for investigating shear-enhanced crystallization and structure development in semicrystalline polymers." Review of Scientific Instruments*, **1999**. *70*: 2097-104.
57. Kumaraswamy, G.; R.K. Verma; J.A. Kornfield; F.J. Yeh, and B.S. Hsiao, "*Shear-enhanced crystallization in isotactic polypropylene. In-situ synchrotron SAXS and WAXD." Macromolecules*, **2004**. *37*: 9005-17.
58. Coates, G.W., "*Precise control of polyolefin stereochemistry using single-site metal catalysts." Chemical Reviews*, **2000**. *100*: 1223-52.
59. Brintzinger, H.H.; D. Fischer; R. Mulhaupt; B. Rieger, and R.M. Waymouth, "*Stereospecific Olefin Polymerization with Chiral Metallocene Catalysts." Angewandte Chemie-International Edition in English*, **1995**. *34*: 1143-70.
60. Doufas, A.K.; I.S. Dairanieh, and A.J. McHugh, "*A continuum model for flow-induced crystallization of polymer melts." Journal of Rheology*, **1999**. *43*: 85-109.
61. Guo, X.; A.I. Isayev, and L. Guo, "*Crystallinity and microstructure in injection moldings of isotactic polypropylenes. Part 1: A new approach to modeling and model parameters." Polymer Engineering and Science*, **1999**. *39*: 2096-114.
62. Isayev, A.I. and C.A. Hieber, "*Toward a Viscoelastic Modeling of the Injection-Molding of Polymers." Rheologica Acta*, **1980**. *19*: 168-82.
63. Bushman, A.C. and A.J. McHugh, "*A continuum model for the dynamics of flow-induced crystallization." Journal of Polymer Science Part B-Polymer Physics*, **1996**. *34*: 2393-407.
64. Acierno, S.; S. Coppola; N. Grizzuti, and P.L. Maffettone, "*Coupling between kinetics and rheological parameters in the flow-induced crystallization of thermoplastic polymers." Macromolecular Symposia*, **2002**. *185*: 233-41.
65. Coppola, S.; N. Grizzuti, and P.L. Maffettone, "*Microrheological modeling of flow-induced crystallization." Macromolecules*, **2001**. *34*: 5030-36.

66. Zuidema, H.; G.W.M. Peters, and H.E.H. Meijer, "*Development and validation of a recoverable strain-based model for flow-induced crystallization of polymers." Macromolecular Theory and Simulations*, **2001**. *10*: 447-60.

2 EXPERIMENTAL INSTRUMENTATION AND METHODS

2.1 Background

Studies of flow-induced crystallization over nearly four decades have focused on various types of flow fields: complex processing flows[1-12] (e.g., injection molding, film blowing, fiber drawing) and controlled flows, either in modified rheometers[13-17] or custom-designed devices.[18,19] Processing flows are difficult to analyze since they involve complex flow fields (mixture of shear and elongation, uniaxial and/or biaxial deformation) that are usually unknown as well as thermal transients and gradients that are, too, usually unknown. Separately, experiments have been performed with known flow and thermal conditions in modified rheometers or custom devices that impose simple, well-defined flows under isothermal conditions. However, comparing the results from well-defined experiments to processing flows is not straightforward. Rheometers are incapable of imposing the magnitude of stress experienced in processing conditions. The highly nonlinear effects of stress make it impossible to extrapolate results seen at low stress to high stress conditions relevant to processing. Furthermore, experiments in rheometers usually involved continuous flow, leading not only to distortion of the polymer melt but a reorganization of the crystallites once formed, complicating analysis of their final orientation distribution.

In the 1990s a renewed interest in flow-induced crystallization was sparked. An elegant approach formulated by Janeschitz-Kriegl and co-workers[20-22] addressed the shortcomings

of prior studies[15-17,23,24] that were complicated by one or more of the following: non-isothermal conditions, continuous flow during the entire crystallization process, and/or inability to access stresses that induce the transition to oriented growth. Their approach involved fitting a valve on the end of an extruder allowing a controlled duration of flow at high stress relevant to processing conditions. The flow was imposed for a brief interval, shorter than the time for crystallites to appear. In this way, the effect of melt deformation on crystallite orientation could be isolated from re-organization of crystallites. Experiments were conducted isothermally so that the effect of temperature could be independently studied.

2.2 Shear-induced crystallization apparatus

We adopt the "short term shearing" approach of Janeschitz-Kriegl to examine the effects of flow as a function of shear stress and shear duration under isothermal conditions, implemented in a custom instrument developed at the California Institute of Technology by Kumaraswamy[25]. A significant advantage of our shear apparatus is a small sample requirement (~10 g) for operation enabling a suite of experiments (500 mg per experiment) to be conducted even on model materials available in limited quantities. The extruder utilized by Janeschitz-Kriegl required a minimum of 22 kg per experiment, limiting investigation to industrially available materials. The relatively compact size of our instrument facilitates synchrotron X-ray experiments to probe structure formation in real time. Like Janeschitz-Kriegl, our instrument for shear-enhanced crystallization can apply a well-defined thermal history and impose high wall shear stresses for a controlled duration, measure birefringence and turbidity during and after shear, and facilitate sample removal for *ex situ* imaging using optical and electron microscopies. Processing-like stresses (wall shear stresses up to ~0.15 MPa) can be accessed by application of large pressure drop across a rectangular channel within a flow cell. The rectangular channel has dimensions 63.5 mm x 6.35 mm x 0.5 mm (length x width x depth). Greater than 10:1 aspect ratios for length:width and width:depth confine entrance effects to a short distance into the channel and provide a nearly two-dimensional flow between parallel plates.[26]

The apparatus consists of the following parts (Figure 2.1): pneumatic actuator for driving flow, melt reservoir for holding polymer sample, heating block to hold the flow cell and maintain crystallization temperature (Figure 2.2), and a removable flow cell (Figure 2.3).

2.3 Experimental protocols

Prior to imposing short-term shearing, the polymer is in a fully relaxed, isothermal state. Polymer is loaded and held at a temperature above its melting point (T_m) in the reservoir immediately adjacent to the flow channel. Upon actuating the pneumatic cylinder, the polymer melt is driven into the flow cell (Figure 2.4). The flow cell is initially held above the equilibrium melting temperature (T_m^0) for the polymer and filled with polymer melt from the reservoir. The polymer in the flow cell is then held at T_{erase} ($> T_m^0$) for 5 – 10 min[27] to erase any (conformational) memory effects caused by the filling process and to melt any residual crystallites. By pre-filling the cell prior to characterization, we eliminate extensional and fountain flow effects associated with polymer filling the empty channel and produce a pressure-driven, shear flow when a second pressure pulse is applied. Finally, the sample is cooled to the crystallization temperature (T_c).

Upon reaching T_c, a desired pressure drop is applied to drive intense shear flow through the channel for a brief shearing time t_s. The imposition of shear demarks the beginning of the experimental time frame ($t=0$). The geometry of the flow cell (length/depth ~ 100) limits the total experimental shear strain at the wall (γ_w) to ~100 strain units to ensure that every fluid element that reaches the observation point was already in the channel at t = 0 (hence subjected to the specified thermal and flow history). Therefore, the maximum t_s that is applied is determined to be that at which ≈ 100 mg of polymer is extruded.

2.4 Sample preparation

Throughout this work we employ bimodal blends of polypropylenes designed to reveal the effects of particular molecular characteristics on flow-induced crystallization. Of particular interest are blends of a small amount of very long chains with a majority of moderate

length "base resin." The enormous viscosity mismatch between the two species precludes melt blending: we found that melt blending resulted in degradation of the long polymer and incomplete mixing of the two components. To obtain a homogeneous mixture, we employ a solution blending method. The two components are weighed and codissolved in a 2.3% xylene solution at 140 °C for 20 min under nitrogen atmosphere and in the presence of an antioxidant (2000 ppm of IRGANOX1010®). A precipitate is obtained by pouring a fine stream of the hot xylene solution into a large excess (8:1) of methanol, which is then filtered and dried under vacuum for 3 days at 80 °C. After further addition of 2000 ppm of a 1:1 mixture of two antioxidants, IRGAFOS168® and IRGANOX1010®, the dried precipitate is press molded at 180 °C under 10,000 psi into an ingot sized to fit the sample reservoir for the shear experiment.

2.5 Characterization methods

To evaluate structural changes during and after cessation of shearing, we use *in situ* rheo-optical and rheo-WAXD measurements. The effects of molecular structure and flow conditions on the final morphologies are established *ex situ* by microscopy.

2.5.1 *In situ* characterization

For real-time measurements of the transient microstructure, the flow cell is fitted with windows in the walls of the flow channel (quartz for optical, beryllium for X-ray) to allow the probing radiation to pass through.

In rheo-optical experiments, turbidity and birefringence are tracked to monitor the progress and anisotropy of crystallization. The optical train consists of He-Ne laser-light (wavelength $\lambda = 632.8$ nm) passing through crossed and parallel polarizers ($I_\perp$ and $I_\parallel$) measured with photodiode detectors.[28] When depolarization is negligible and the retardance ($\Delta n \pi d$) is less than a half-wave ($\lambda/2$), the birefringence (Δn), which is a measure of the mean anisotropy of sample, is given by

$$\Delta n = \frac{\lambda}{\pi d} \arcsin \sqrt{\frac{I_{\perp}}{I_{tot}}}, \qquad (2.1)$$

where d is the thickness of the sample. When strongly oriented crystallization proceeds after flow, the retardance become very large ($\Delta n \pi d > \lambda/2$). The time at which the retardance reaches a half-wave is marked by appearance of a maximum in $I_{\perp}/I_{\parallel}$. Successive minima correspond to increasing odd multiples of $\lambda/2$ and successive maxima correspond to even multiples of $\lambda/2$. Transmittance is defined as total transmitted intensity ($I_{tot}=I_{\perp}+I_{\parallel}$) normalized by a constant value of $I_{tot,0}$ before shearing.

The modular design of the apparatus enables relocation to a synchrotron X-ray source for *in situ* rheo-WAXD experiments. The optical train is modified to include a CCD camera (Figure 2.5) to capture 2-D diffraction patterns, and the quartz windows are replaced by beryllium. Further details regarding the synchrotron X-ray experiments are provided in Chapter 3.

2.5.2 *Ex situ* characterization

The flow cell is removable and designed for easy extraction of solidified samples. The crystalline sample can be sliced into thin sections using a cryomicrotome for further inspection by microscopy (5 – 10 μm thickness for optical microscopy, and 100 nm thickness for transmission electron microscopy [TEM]). Polarized light microscopy and TEM are used to study the final morphology at micrometer and nanometer length scales, respectively.

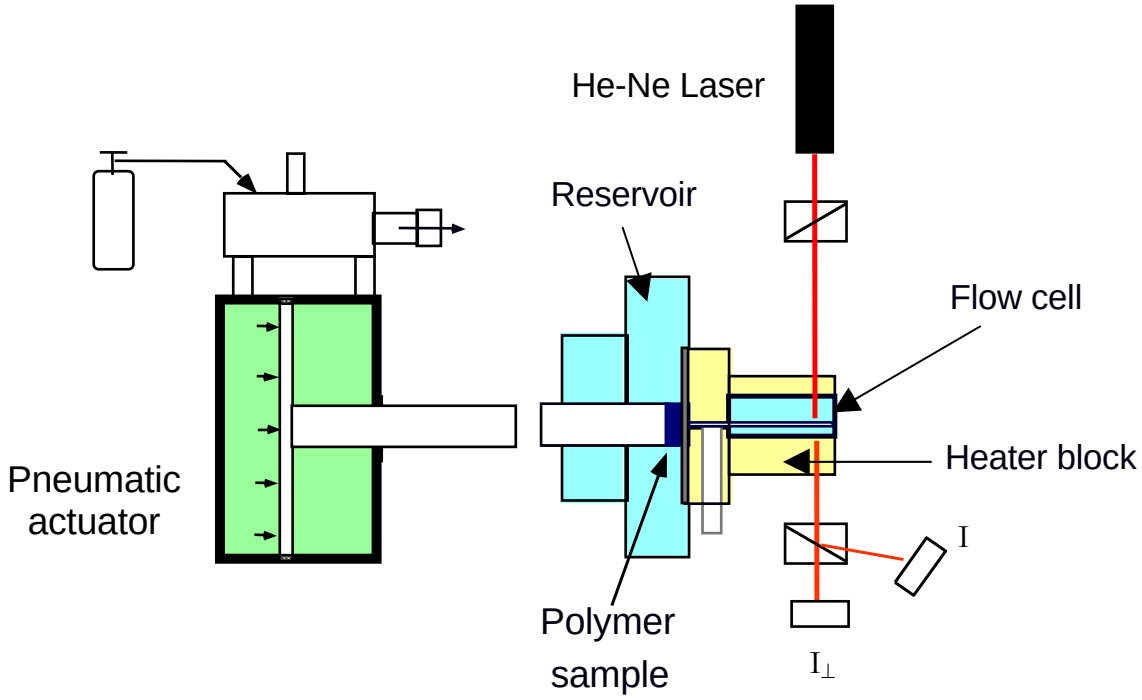

Figure 2.1: Schematic of shear-induced crystallization apparatus.

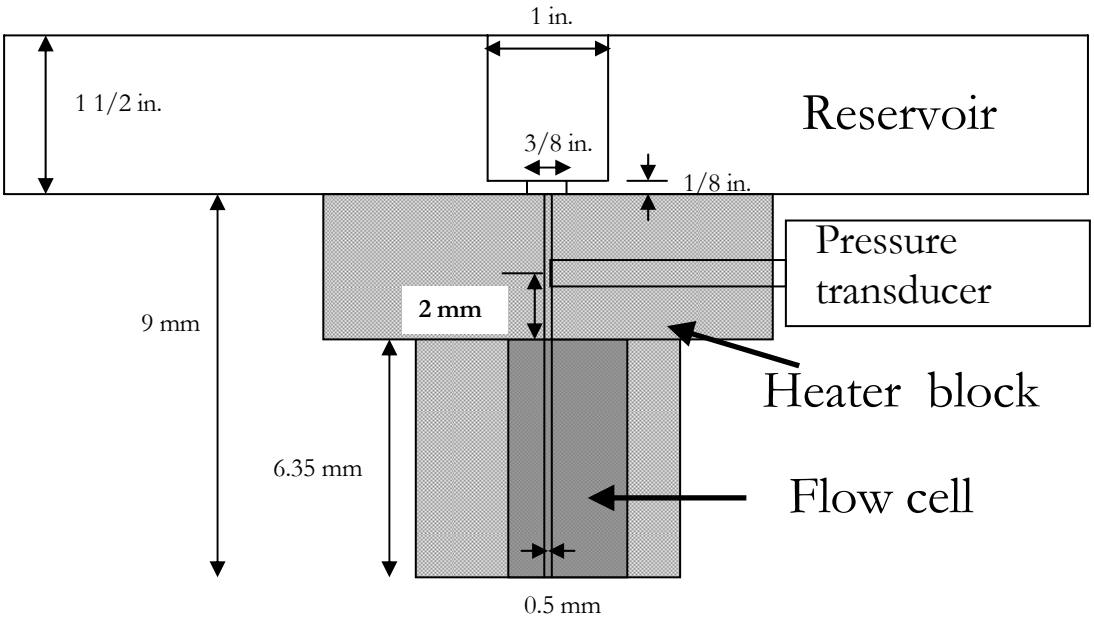

Figure 2.2: Schematic of melt reservoir, heater block, and flow cell (gray) assembly.

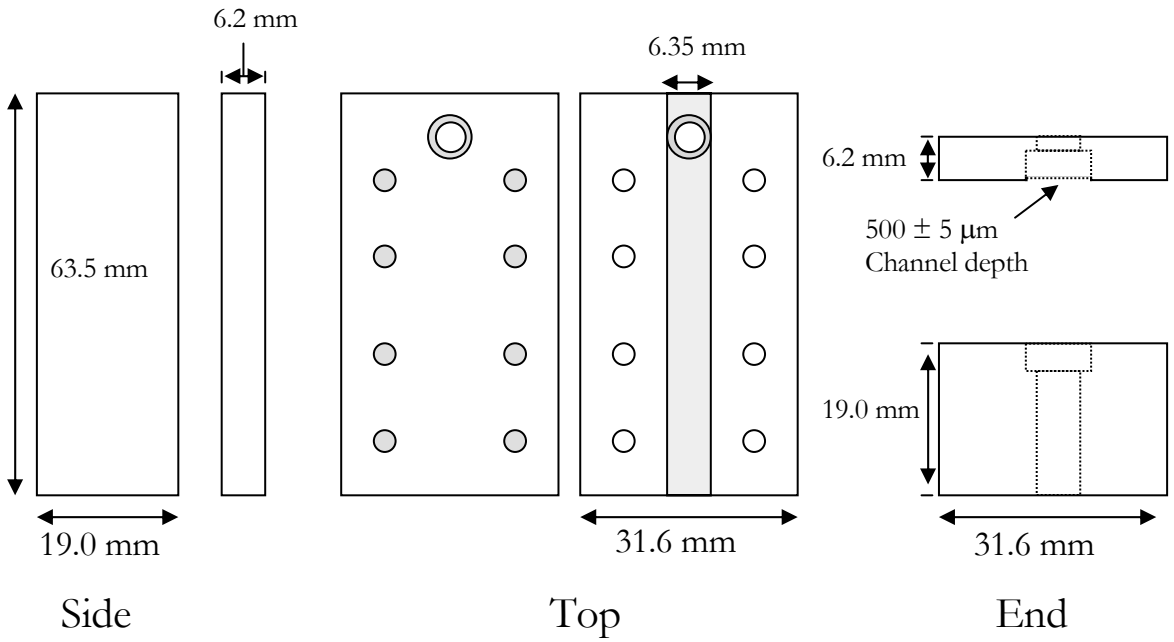

Figure 2.3: Schematic of flow cell.

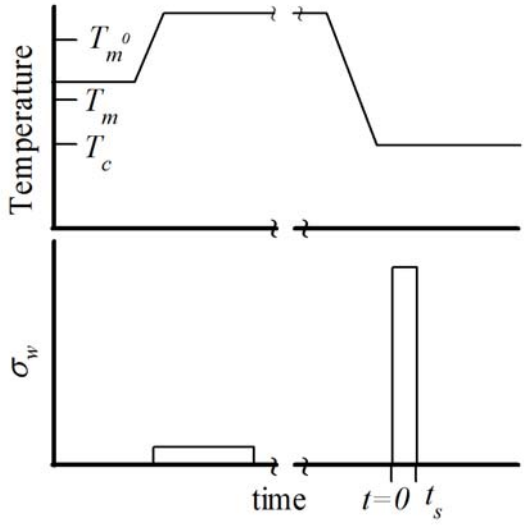

Figure 2.4: Schematic of the thermal and flow history imposed on samples subject to flow-induced crystallization.

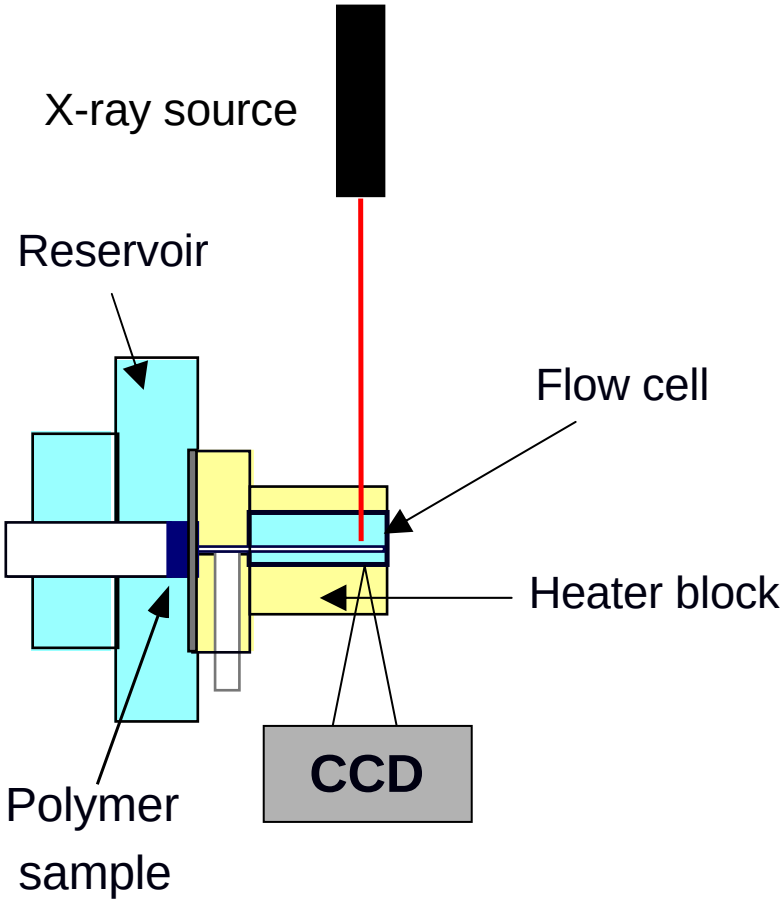

Figure 2.5: Schematic of optical arrangement for WAXD.

2.6 Bibliography

1. Fitchmun, D.R. and Z. Mencik, "*Morphology of Injection-Molded Polypropylene." Journal of Polymer Science Part B-Polymer Physics*, **1973**. *11*: 951-71.
2. Guo, X.; A.I. Isayev, and L. Guo, "*Crystallinity and microstructure in injection moldings of isotactic polypropylenes. Part 1: A new approach to modeling and model parameters." Polymer Engineering and Science*, **1999**. *39*: 2096-114.
3. Guo, X.; A.I. Isayev, and M. Demiray, "*Crystallinity and microstructure in injection moldings of isotactic polypropylenes. Part II: Simulation and experiment." Polymer Engineering and Science*, **1999**. *39*: 2132-49.
4. Trotignon, J.P. and J. Verdu, "*Skin-Core Structure Fatigue Behavior Relationships for Injection-Molded Parts of Polypropylene .1. Influence of Molecular-Weight and Injection Conditions on the Morphology." Journal of Applied Polymer Science*, **1987**. *34*: 1-18.
5. D'Orazio, L. and G. Cecchin, "*Isotactic polypropylene/ethylene-co-propylene blends: effects of composition on rheology, morphology and properties of injection moulded samples." Polymer*, **2001**. *42*: 2675-84.
6. Samon, J.M.; J.M. Schultz, and B.S. Hsiao, "*Structure development in the early stages of crystallization during melt spinning." Polymer*, **2002**. *43*: 1873-75.
7. Schultz, J.M.; B.S. Hsiao, and J.M. Samon, "*Structural development during the early stages of polymer melt spinning by in-situ synchrotron X-ray techniques." Polymer*, **2000**. *41*: 8887-95.
8. Wu, J.P. and J.L. White, "*Crystalline Orientation in Injection Molded Polyethylene Parts." International Polymer Processing*, **1992**. *7*: 350-57.
9. Bond, E.B. and J.E. Spruiell, "*Melt spinning of metallocene catalyzed polypropylenes. I. On-line measurements and their interpretation." Journal of Applied Polymer Science*, **2001**. *82*: 3223-36.
10. Bond, E.B. and J.E. Spruiell, "*Melt spinning of metallocene catalyzed polypropylenes. II. As-spun filament structure and properties." Journal of Applied Polymer Science*, **2001**. *82*: 3237-47.
11. Zhang, X.M.; S. Elkoun; A. Ajji, and M.A. Huneault, "*Oriented structure and anisotropy properties of polymer blown films: HDPE, LLDPE and LDPE." Polymer*, **2004**. *45*: 217-29.
12. Lu, J.J.; H.J. Sue, and T.P. Rieker, "*Morphology and mechanical property relationship in linear low-density polyethylene blown films." Journal of Materials Science*, **2000**. *35*: 5169-78.
13. Fritzsche, A.K. and F.P. Price, "*Crystallization of Polyethylene Oxide under Shear." Polymer Engineering and Science*, **1974**. *14*: 401-12.
14. Fritzsche, A.K.; F.P. Price, and R.D. Ulrich, "*Disruptive Processes in Shear Crystallization of Poly(Ethylene Oxide)." Polymer Engineering and Science*, **1976**. *16*: 182-88.
15. Wolkowicz, M.D., "*Nucleation and Crystal-Growth in Sheared Poly(1-Butene) Melts." Journal of Polymer Science Part C-Polymer Symposium*, **1977**: 365-82.
16. Andersen, P.G. and S.H. Carr, "*Crystal Nucleation in Sheared Polymer Melts." Polymer Engineering and Science*, **1978**. *18*: 215-21.

17. Lagasse, R.R. and B. Maxwell, "*Experimental-Study of Kinetics of Polymer Crystallization During Shear-Flow." Polymer Engineering and Science*, **1976**. *16*: 189-99.
18. Haas, T.W. and B. Maxwell, "*Effects of Shear Stress on Crystallization of Linear Polyethylene and Polybutene-1." Polymer Engineering and Science*, **1969**. *9*: 225-&.
19. Wereta, A. and C.G. Gogos, "*Crystallization Studies on Deformed Polybutene-1 Melts." Polymer Engineering and Science*, **1971**. *11*: 19-&.
20. Eder, G. and H. Janeschitz-Kriegl, *Crystallization*, in *Processing of Polymers*, H.E.H. Meijer, Editor. 1997, Wiley-VCH: New York. p. 269-342.
21. Eder, G.; H. Janeschitzkriegl, and S. Liedauer, "*Crystallization Processes in Quiescent and Moving Polymer Melts under Heat-Transfer Conditions." Progress in Polymer Science*, **1990**. *15*: 629-714.
22. Janeschitz-Kriegl, H. and G. Eder, "*Basic Concepts of Structure Formation During Processing of Thermoplastic Materials." Journal of Macromolecular Science-Chemistry*, **1990**. *A27*: 1733-56.
23. Vleeshouwers, S. and H.E.H. Meijer, "*A rheological study of shear induced crystallization." Rheologica Acta*, **1996**. *35*: 391-99.
24. Sherwood, C.H.; F.P. Price, and R.S. Stein, "*Effect of Shear on Crystallization Kinetics of Poly(Ethylene Oxide) and Poly(Epsilon-Caprolactone) Melts." Journal of Polymer Science Part C-Polymer Symposium*, **1977**: 77-94.
25. Kumaraswamy, G.; R.K. Verma, and J.A. Kornfield, "*Novel flow apparatus for investigating shear-enhanced crystallization and structure development in semicrystalline polymers." Review of Scientific Instruments*, **1999**. *70*: 2097-104.
26. Janeschitz-Kriegl, H., *Polymer Melt Rheology and Flow Birefringence*. Polymers: Properties and Applications. Vol. 6. 1983, New York: Springer-Verlag. 524.
27. The effect of annealing time of the freshly filled flow cell was determined by altering the annealing time while holding crystallization conditions constant. The crystallization kinetics and orientation measured by turbidity and birefringence for samples held more than 5 min at 215 C were identical within experimental error.
28. Kumaraswamy, G.; A.M. Issaian, and J.A. Kornfield, "*Shear-enhanced crystallization in isotactic polypropylene. 1. Correspondence between in situ rheo-optics and ex situ structure determination." Macromolecules*, **1999**. *32*: 7537-47.

3 EFFECTS OF LONG CHAIN CONCENTRATION IN BIDISPERSE BLENDS

3.1 Introduction

The strong effects of flow on crystallization are attributed to the perturbation of chain configuration by flow. It has been generally believed that extension of macromolecules promotes the formation of long threadlike structures oriented in the direction of elongation, and these filaments provide nucleating surfaces for radial growth of chain-folded lamellae. Keller and coworkers[1, 2] have studied flow-induced crystallization in polymer solutions, where interactions between molecules can be minimized, in order to describe the underlying mechanisms of polymer crystallization from the oriented state, partly based on the detailed study of “shish-kebab” structures grown from stirred solutions.[3] This “row-nucleated structure” model, deduced from solution studies, also describes the morphology resulting from elongational flow-induced crystallization of bulk polymers where the

connectivity within a chain and the entanglements between chains restrict the segmental diffusion of the molecules.[4] Similar shish-kebab morphology is induced by shear flow in which full extension of individual chains is unlikely. Perhaps extension of portions of the chain between topological constraints in the melt is sufficient to produce threadlike structures,[5] or perhaps chain extension is not required.

It has also been inferred that flow-induced changes in crystallization kinetics and the induction of the shish-kebab structure are strongly affected by "long chains."[6-12] The evidence is based predominantly on samples that have broad distributions of molecular weight and molecular regularity. This has presented a major obstacle to 1) defining what is meant by the long chains, 2) proving that their role is due specifically to length and not to more perfect molecular structure (traditional polyolefins produced by Ziegler-Natta type catalysts have correlated length and regularity[13, 14]), and 3) discerning how their impact varies with concentration to gain deeper insight into the physical basis of their effect. Further, when comparing materials of different average length, a number of investigators have used experiments performed holding deformation rate fixed.[6-10, 15-17] This choice makes it difficult to attribute observed differences in behavior to molecular length per se, since the comparisons are made at very different stress. The effects of stress are known to be very strong, including qualitative changes in kinetics and morphology upon crossing threshold stress levels; therefore, comparisons made at fixed stress are needed to probe effects of chain length and its distribution.

To overcome the limitations of poorly defined materials, we follow the approach of Kumaraswamy et al.,[18] who demonstrated that preparation of binary blends of narrow distribution isotactic polypropylenes (iPPs) provides a route to model materials in which the length and concentration of long chains are known and can be systematically varied. To expose the effect of long chains on the response during and after shear, we adopt the "short term shearing" approach of Janeschitz-Kriegl[19-21] and make comparisons of the effects of flow at a given shear stress. To evaluate structural changes during and after cessation of shearing, we use *in situ* rheo-optical and rheo-WAXD measurements. To reveal the effects

of molecular structure and flow conditions on the final morphologies, *ex situ* microscopic observations were performed.

Portions of the work in this chapter were performed by collaborators[22] who provided fractionated long chain polymers, polymer characterization (GPC and NMR), and optical and electron micrographs. Our primary collaborator, Dr. Seki, prepared polymer blends and conducted DSC characterization and rheo-optical experiments in our laboratory at the California Institute of Technology. (Parts of this chapter have been published and are reproduced with permission from *Macromolecules*, **2002**. 35: 2583-94. Copyright 2002 American Chemical Society).

3.2 Experimental

3.2.1 Materials

An iPP with moderate molecular weight (186 kg/mol) and narrow polydispersity in terms of both molecular weight (M_w/M_n = 2.3) and stereoregularity ([mmmm] = 96%, T_m = 148 °C) was provided by Dr. Robert Sammler[23] for use as a base polymer resin (Base-PP). An iPP with much higher molecular weight (923 kg/mol), narrow PDI (M_w/M_n = 1.3), and high stereoregularity ([mmmm] = 98%, T_m = 165 °C) (L-PP) was prepared by fractionation from a parent iPP polymerized with a Ziegler-Natta catalyst. The tight distribution of chain length for L-PP (Figure 3.1) was achieved by using fractionation by the solvent gradient method, in which the solvent composition of *o*-dichlorobenzene and diethylene-glycol-monomethyl-ether in polymer solution was changed gradually.[24] The methods used for molecular characterization are presented below in Section 3.2.7.[25] The difference in stereoregularity and M_w led to a 16.3 °C difference in the apparent melting point of the two samples.

Bidisperse blends were prepared with different concentrations of L-PP (c), varying c from 0 to twice the critical concentration of L-PP (c^*) at which molecular coils of L-PP begin to overlap one another (Table 3.1). The overlap concentration, c^*, is[26, 27]

$$c^* = \frac{3M_w}{4\pi(R_g^{\,2})^{3/2}N_a}, \qquad (3.1)$$

where N_a is Avogadro's number and R_g is the radius of gyration. The characteristic ratio of the weight-averaged radius of gyration to M_w of iPP ($<R_g^2>/M_w^{0.5}$) is 0.39 according to SANS measurements,[28] leading to an estimated c^* of 7.0 x 10^{-3} g/cm^3 for L-PP. Blends are coded using the value of c/c^*. For example, B025 denotes the blend with $c/c^* = 0.25$. Blends were prepared by solution blending as described in Chapter 2.

3.2.2 *In situ* rheo-optical measurements

The flow cell was initially held at 215 °C and filled with polymer melt from the reservoir. The polymer in the flow cell was then held at 215 °C for 10 min[29] to erase any memory effects caused by the filling process. Finally, the sample was cooled to the crystallization temperature (T_c). Upon reaching T_c, a desired pressure drop was applied to drive shear flow through the channel for a brief shearing time t_s. All experiments described here were conducted at the same T_c of 137 °C. Temperature stability was maintained within ± 0.3 °C. Short-term shear pulses, corresponding to wall shear stresses (σ_w) of 0.055, 0.09, 0.11, and 0.12 MPa were applied for brief periods such that t_s was much less than the crystallization time at this temperature. In order to change total strain applied, the amount of polymer extruded (w_{ex}) was varied from about 30 mg to 100 mg by changing t_s from about 250 ms to 8 s. The turbidity and birefringence were tracked to monitor the progress and anisotropy of crystallization.

3.2.3 *In situ* rheo-WAXD

A selected set of shearing conditions were further examined by rheo-WAXD (wide angle X-ray diffraction) to provide more detailed information concerning crystallization kinetics and the orientation distribution of the crystallites. The modular nature of our shearing apparatus allows facile relocation to a synchrotron radiation source. The flow cell used for rheo-optical experiments containing quartz windows is replaced by a cell with beryllium windows, which are largely X-ray transparent. No additional modifications of the apparatus are required. The high beam flux available from a synchrotron enables time-resolved X-ray

diffraction measurements from weakly scattering materials such as polymers. WAXD experiments were performed at beamline X27C at the National Synchrotron Light Source.[30] The beam at X27C is tuned to a wavelength of 1.366 Å. Two-dimensional scattering patterns (1024 x 1024 pixels) were collected using a MarCCD camera.[31]

The 2-D WAXD patterns are background corrected by subtracting an empty cell background pattern to remove excess scattering from the beryllium windows and air. Each frame captured is normalized according to acquisition time and the time dependent beam intensity of the synchrotron source. The resulting patterns are analyzed in terms of a circular average of the scattered intensity vs. scattering vector **q** and azimuthal scans of the orientational dependence of scattering intensity of the 110 and 040 diffraction planes.

It is not possible to compute the quantitative degree of crystallization from our WAXD data, so we use a crystallinity index to characterize the increase in overall crystallinity with time. Quantitative calculation of the degree of crystallinity requires a wide enough range of diffraction angles to perform an analysis such as the Ruland[32] method. Further, it requires that the crystallite orientation distribution be well-defined and invariant with time. Alternatively, we report a crystallinity index (x_c)

$$x_c = \frac{I_c}{I_c + I_a}, \tag{3.2}$$

where I_c and I_a are the intensities of the crystalline and amorphous portions of the scattering profile respectively, as determined from a circular average of scattering intensity vs. **q**. The crystallinity index includes the major peaks captured in our data in the scattering range **q** = 0.9 – 1.6 (Figure 3.2). The amorphous and crystalline portions of the profile are deconvoluted by subtracting the scattering profile of the amorphous polymer prior to shear treatment scaled appropriately to approximate the amorphous portion of each scattering profile (Figure 3.2). The resultant represents scattering from the crystalline portion only. The crystallinity index does not give a quantitative degree of crystallinity and neglects the orientation dependent nature of crystalline scattering. Here we use x_c to highlight overall changes in the rate of crystallization due to flow as a function of polymer composition and

to qualitatively compare the overall rate of crystallization with that of the oriented crystallites.

To characterize the orientation distribution of crystallites, azimuthal scans are performed at each Bragg angle of interest (110 and 040). The amorphous contribution to the diffracted intensity at that scattering angle is estimated from the circularly averaged data using a linear interpolation between scattering angles on either side of the diffraction peak (dotted lines, Figure 3.2). After subtracting the amorphous contribution, the azimuthal distribution of intensity is analyzed to determine the angular position, peak amplitude, and full-width at half-maximum (FWHM) that provide the best fit of a Lorentzian line shape to the experimental data. Emphasis is placed on the 110 reflection because it reveals the relative amounts and the angular distributions of parent crystallites and their epitaxial daughter crystallites.

To properly evaluate the ratio of parent to daughter crystallites (P:D), it is necessary to apply a geometrical scaling to the azimuthal intensity to account for orientation-dependent scattering. The geometry of the Ewald's sphere construct dictates that crystallites with uniaxial orientation along the axis of the orientation sphere (the flow direction in our case) will have a diminished diffracted intensity compared with an isotropic distribution of the same amount of crystallites such that

$$\frac{Oriented}{Isotropic} = \frac{2}{f\pi \sin(\phi)}, \tag{3.3}$$

where ϕ is the azimuthal angle and $f = \sin(90 - \theta)$ with θ denoting the scattering angle; f has the value 0.992 and 0.989 for 110 and 040 planes, respectively.[33] For a given number of crystalline poles (plane normals), the intensity of diffraction depends on the density of poles that satisfy the Bragg condition (at each 2θ). Crystalline poles with perfect uniaxial orientation at an angle ϕ from the axis of the orientation sphere trace out a cone on the orientation sphere (Figure 3.4). For example, crystalline poles oriented perpendicular to the axis of orientation will cover a disc (a cone of $\phi = 90°$) and have a relatively low density of poles that intersect the Ewald's sphere. In contrast, crystalline poles oriented along the

orientation axis ($\phi = 0$) will have a high density. On our flat plate image, the flow direction and axis of the orientation sphere are along the equator (horizontal direction) of the 2-D image. Therefore, the scattered intensity detected on the meridian (vertical direction) of the 2-D image from crystalline poles oriented at $\phi = 90°$ appears less intense than an equivalently oriented group of crystalline poles oriented along the equator $\phi = 0°$.

3.2.4 *Ex situ* microscopy (OM and TEM)

Sheared samples examined in the rheo-optical experiments were allowed to solidify at T_c = 137 °C *in situ* until the transmittance dropped to zero, after which the flow cartridge was removed and plunged into ice water. After the cartridge had cooled, the sample was removed and prepared for *ex situ* morphology studies. Thick sections (thickness = 10 μm) were taken in the flow-vorticity and flow-gradient planes and were examined using a polarization optical microscope (OM). Ultra thin sections approximately 100 nm in thickness were cut at a position corresponding to the center of the optical window. A block face was cut, the sample was stained with ruthenium tetroxide for two hours at 50 °C,[34] and sections were cut from the block face using a microtome. Thin sections for both "through" and "edge" views were prepared (images in the flow-vorticity and flow-gradient planes, respectively). Transmission electron microscope (TEM) observation was carried out at Mitsubishi using a JEOL TEM model JEM 1230 at 100 kV.

3.2.5 DSC measurements

In a differential scanning calorimeter (Perkin-Elmer DSC-7), the crystallization and melting of iPPs were characterized at a scanning rate of 5 °C/min in N_2 atmosphere.

3.2.6 Measurement of molecular weight

Weight averaged molecular weight (M_w) and polydispersity of molar mass for iPPs were measured at Mitsubishi by GPC with an on-line multi-angle laser light scattering photometer (GPC-MALLS). The measurements were performed on a Waters model 150C with three polystyrene columns (SHODEX KF-806M from Showa Denko Co. Ltd.) at 413.2K using a flow rate of 1.0 mL/min. The sample was injected as a 0.3 mL aliquot of a 1,2,4-trichlorobenzene solution with 2 mg/mL concentration. The differential refractometer

was used to detect solute concentrations and specific refractive index increments. The MALLS model DAWN DSP from Wyatt Technology Corporation, equipped with a He-Ne laser (λ = 632.8 nm), was connected with the GPC instrument. The ASTRA software package from Wyatt was used for analyzing GPC data and scattering data, which were collected simultaneously at 17 scattering angles ranging from 18° to 155° (details[25] are given elsewhere).

3.3 Results

3.3.1 Quiescent crystallization kinetics

The peak crystallization temperature, melting temperature, and enthalpy change (ΔH_f) were measured by differential scanning calorimetry (DSC) at a constant cooling rate. These values were almost identical for all blends and were ≈ 112 °C, ≈ 143 °C, and 85 J/g, respectively (Table 3.1). Addition of L-PP to Base-PP did not affect the crystallization kinetics under quiescent conditions, even though pure L-PP has greater crystallinity and faster kinetics compared with Base-PP due to its higher stereoregularity. Similarly, the turbidity half time, defined by the time at which the transmittance reaches one-half, was approximately 6500 s at 137 °C for all blends (Figure 3.5). Slight differences in the turbidity half time can be ascribed to variability in the temperature control.

3.3.2 *In situ* rheo-optical

3.3.2.1 Turbidity

The development of turbidity at earlier times indicates that crystallization kinetics accelerate with increasing σ_w even when t_s is reduced to hold the total applied strain nearly constant (Figure 3.6). The turbidity half time of the blends sheared at 0.12 MPa for the maximum t_s was approximately ten times shorter than that for quiescent conditions. The addition of low concentrations of long chains (< 2% wt.) only slightly alters the melt rheology. Therefore, these measurements are made not only at fixed stress (hence nearly the same average level of segmental orientation due to flow), but also for similar shearing time and total applied strain.

The turbidity half time also decreases with increasing t_s, but the dependence on t_s is much weaker than the dependence on σ_w (Figure 3.7).

3.3.2.2 Birefringence

Distinctive changes in the transient birefringence with applied stress indicate a critical stress level necessary to induce highly oriented crystalline growth in the sample. Therefore, we define a "critical shear stress" (σ^*) necessary for this event. For the present samples, as described below, the critical shear stress showed a significant and monotonic decrease with increasing c/c^* (Figure 3.8).

Below this threshold stress ($\sigma_w < \sigma^*$), the birefringence profiles show no evidence of highly oriented growth (Figure 3.9). The plots of $I_\perp/I_{tot}$ for B1 are representative of all blends during and after shearing at σ_w, ranging from 0.055 to 0.11 MPa for different t_s (0.5 s < t_s < maximum t_s). $I_\perp/I_{tot}$ during shearing exhibits a boxlike locus, which increases in a matter of ~50 ms to the plateau value, and is nearly constant and then at t_s drops to the baseline value, a response that is consistent with the applied pressure profile. $I_\perp/I_{tot}$ then increases gradually after cessation of flow, reaching a value around 0.1 at the end of the optical experiment (stopped when the transmittance falls to zero) regardless of c and σ_w (< 0.11 MPa). The delay time (t_d) between the cessation of shearing and the subsequent growth of $I_\perp/I_{tot}$ decreases with increasing σ_w and increasing c. For example, t_d decreases 900 ± 100, 650 ± 50, 600 ± 50, 450 ± 30, and 500 ± 30 s as c increases for B0, B025, B05, B1, and B2, respectively, for σ_w = 0.09 MPa and maximum t_s. The low turbidity at t_d ($I_{tot}/I_{tot,0} \approx 1.0$) suggests that this rise in $I_\perp/I_{tot}$ is not due to depolarization. The effect of t_s on t_d is very weak for σ_w < 0.11 MPa but indicates a faster onset of crystallization with increasing t_s.

For $\sigma_w \geq \sigma^*$, the birefringence profiles show evidence of highly anisotropic crystallization (Figure 3.10). The values of $I_\perp/I_{tot}$ during crystallization after shearing attain remarkably large values compared with results at lower σ_w (σ_w < 0.11 MPa). For B025 with σ_w = 0.12 MPa and t_s = 0.5 s (less than the maximum t_s), $I_\perp/I_{tot}$ reaches 0.4, more than four times

larger than the ultimate value following shear at a slightly lower σ_w and maximum t_s.

The development of $I_{\perp}/I_{tot}$ for shear at 0.12 MPa is strongly affected by c and t_s. With increasing t_s and c, birefringence after transient shearing grows faster and achieves higher values. When the long chain concentration increases to $c/c^* = 0.5$, we observe a qualitative change in the evolution of birefringence during transient shearing. The loci of $I_{\perp}/I_{tot}$ for B0 and B025 during transient shearing at 0.12 MPa generate the same boxlike shape as that sheared at lower σ_w; however, for B05, B1, and B2 we see that $I_{\perp}/I_{tot}$ exhibits an "upturn" during shear after the plateau value is reached and then relaxes upon cessation of shear (Figure 3.10). The "upturn" feature has been shown to correspond to the formation of a "shear-induced structure" that gave fiber-like crystalline reflections of the α-modification of iPP during real time synchrotron WAXD in a conventional Z-N iPP.[35, 36] Subsequently, these samples were shown to have developed a skin-core crystalline morphology. In our samples, the "upturn" in birefringence similarly indicates that shearing at $\sigma_w > \sigma^*$ results in the formation of a highly oriented structure in B05, B1, and B2. The "upturn" appears at $t_s = 0.35$ s in these three blends, corresponding to w_{ex} of approximately 65 mg. Moreover, it should be noted that the birefringence of B1 and B2 after transient shearing at $\sigma_w > \sigma^*$ does not completely relax to the baseline value when $t_s > 1$ s (Figure 3.10D and 3.10E).

The ultimate value of birefringence (at the time the transmittance fell to zero) does not increase linearly with c but distinctively increases around c/c^* of 0.5 (Figure 3.11). This non-linear dependence on long chain concentration suggests that the kinetic and morphological results due to increased long chain content are due to a multi-body effect. Specifically, long chain-long chain overlap enhances the development of anisotropy during shearing, i.e., the appearance of the birefringence "upturn," and leads to well-developed oriented structures during subsequent crystallization.

3.3.3 *In situ* rheo-WAXD

The material used to prepare bidisperse blends was limited, which restricted X-ray scattering experiments to just three materials, B0, B05, and B1, and to stresses that induce oriented crystallization ($\sigma_w > \sigma^*$). All samples crystallized primarily in the monoclinic α crystalline phase confirmed by the positions of 5 strong diffraction peaks (110, 040, 130,

111, and 041/131). At long times, a small amount of γ crystalline content is detected, evident by the unique peak at **q** = 1.43 $Å^{-1}$. The presence of γ-phase crystallites is known to occur in metallocene based iPP[37] due to its particular distribution of stereo- and regio-defects; γ-crystallites commonly nucleate epitaxially from the *ac* face of α-iPP crystallites.[38]

Scattering reflections for α-iPP (110, 040, and 130) centered on the meridian of the 2-D WAXD pattern (Figure 3.12) indicate crystallites with c-axis oriented along the flow direction. As is the case for most polymers, the c-axis of the unit cell is along the direction of the chain axis of the molecule for α-iPP. A second population of crystallites is indicated by maxima flanking the equator of the pattern along the 110 plane. Isotactic polypropylene exhibits a unique lamellar branching behavior[38] known as "cross-hatching" in which a second population of crystallites (daughters) grows epitaxially from existing crystalline lamellae (parents). These daughter crystallites are oriented nearly perpendicular to the parents (~80° or ~100°, the β angle of the monoclinic unit cell of α-iPP). The azimuthal distribution of intensity of the 110 diffraction peak is analyzed to determine the distribution of parent and daughter crystallites. (Daughter peaks can in principle be distinguished along the 130 plane as well, but are not as prominent as those along 110 and are located much closer to the parents, making the 130 unsuitable for determination of parent:daughter ratio.)

The qualitative effects of long chain concentration are evident in the 2-D WAXD patterns (Figure 3.12) recorded at a particular time (1200 s) after shearing at a given stress (σ_w = 0.11 MPa) for a fixed number of strain units (fixed extruded mass, w_{ex}): the blends with long chains added show much greater overall crystallinity and the enhancement is largely due to the growth of strongly oriented crystals.

During crystallization, x_c increases more rapidly for the blends than for the base resin (Figure 3.13A): at a concentration of 0.5c*, long chains result in roughly double the crystallization rate compared to the base polymer (B0), and at c* the overall rate is roughly 2.5x greater than for B0. The difference can be attributed to the quantity of oriented crystallites measured by the amplitude of the 110 parent peaks (Figure 3.13B). The strength

of the effect of long chains depends on the stress imposed. We find that low concentrations of long chains reduce σ^*, the threshold stress required to trigger the transition to oriented growth. The differences in behavior between the base resin and the binary blends are most pronounced in the range of stress that lies above σ^* of the blend and below σ^* of the base resin, as in the case for the flow conditions of Figures 3.12, 3.13, and 3.14.

Increasing the concentration of long chains leads to the following trends in the kinetics and morphology of crystallization of the oriented skin: the population of oriented crystals, tracked using the amplitude of the parent peak in the 110 diffraction (Figure 3.13B), grows more rapidly and reaches higher values before the time at which parent growth slows; the degree of orientation increases, as indicated by the decrease in azimuthal width of the parent 110 peak (Figure 3.13C); and the predominance of parent crystallization over daughter crystallites increases (Figure 3.14A and 3.14C).

In addition to the dramatic effects of long chains on the formation of the oriented skin, the WAXD patterns also indicate enhancement of unoriented crystallization in the bimodal blends relative to B0 (Figure 3.14C).

For the 110 reflection, overlap of the parent and daughter peaks contributes to the baseline of azimuthal scans, especially for broad distributions. However, the parent and daughter are coincident along the meridian at the 040 reflection since the unit cells share a common b-axis. Therefore, we analyze the azimuthal dependence of the 040 reflection to quantify the oriented (parent + daughter) population relative to the unoriented population. For this reason, we used the 040 plane to determine the baseline due to isotropic crystalline scattering.

3.3.4 *Ex situ* microscopy (OM and TEM)

Optical micrographs (OM) under crossed polarizers and TEM for a B2 sample sheared at 0.055 MPa for 7.5 s (w_{ex} = 98 mg) and then crystallized at T_c = 137 °C for 2800 s are presented to show the typical morphology of blends sheared at $\sigma_w < \sigma^*$ (Figure 3.15). The

value of $I_{\perp}/I_{tot}$ just before removing the sample was 0.075 ± 0.03. A thin (5 μm thick), somewhat oriented skin layer can be seen at the surfaces of the sample, and a fine-grained layer of spherulitic structures is observed below the skin layer. The thin birefringent skin layer is composed of stacked lamellae grown perpendicular to the flow direction (Figure 3.15B).

A similar thin layer of lamellae perpendicular to flow also appears in some of the OM and TEM images for samples sheared at $\sigma_w > \sigma^*$ (Figure 3.16). Previously, Kumaraswamy encountered such a layer but was unable to determine its nature.[36] The replica technique used to image the features of the sample by TEM was not suitable to capture features in this dense layer. However, ruthenium tetroxide staining provides adequate contrast to distinguish the crystalline features. In the example shown (Figure 3.16), the perpendicular lamellae occur in a layer extending 6 μm from the cell wall adjacent to the highly birefringent layer and appear slightly darker in optical micrographs. At higher magnification (TEM), the morphology of the 6 μm layer appears distinctly different than the shish-kebab structures (highly birefringent layer) farther from the wall. At the highest magnification, we discern individual lamellae and can visualize the cross-hatching behavior. The high number of cross-hatches in this layer accounts for the dark appearance when viewed between crossed polarizers since the nearly perpendicular parent and daughter lamellae cancel each other's birefringence. We believe the presence of this thin stacked lamellar layer is due to a flow effect at the wall surface (quartz windows). Crystallization of the polymer on a quartz window substrate at the quiescent condition did *not* produce ordered stacks of lamellae (Figure 3.17).

All blends crystallized after shearing at σ_w of 0.12 MPa ($> \sigma^*$) showed a highly oriented skin layer (Figure 3.18A-E). The skin layers appear as bright bands at the walls when viewed through crossed polarizers. The thickness of the skin layers for B0, B025, B05, B1, and B2 (Figure 3.18A-E) are estimated to be 10 ± 3, 25 ± 10, 53 ± 5, 47 ± 8, and 47 ± 5 μm, respectively. The thickness and uniformity of the skin layer increases remarkably at c/c^* of 0.5 and saturates for $c/c^* = 1$ or higher. The position of the abrupt transition between the skin layer and the spherulitic core provides a measure of the threshold stress required to

induce the transition to oriented growth, σ^*, since the stress decreases linearly from the wall to the center of the flow channel. At depths greater than 50 μm from the wall, highly oriented crystallites are not observed; the boundary is fairly sharp and corresponds to $\sigma^* \approx 0.11$ MPa. The saturation in skin thickness as a function of long chain content indicates that the threshold stress varies weakly with c for $0 < c < 0.25c^*$, strongly for $0.25c^* < c < 0.5c^*$, and weakly for $0.5c^* < c$ (Figure 3.8). As previously reported,[35] the formation of the oriented skin observed *ex situ* correlates with the development of strong birefringence *in situ* after cessation of shear as lamellae grow transverse to the precursors created during shear (Figures 3.10 and 3.18).

A difference in the exact depth of the channel of flow cells containing beryllium windows used in rheo-WAXD experiments compared with the cells used for rheo-optical experiments resulted in a lower σ_w when the same pressure drop was applied across the cell. Therefore, the rheo-WAXD experiments required longer shearing times to apply the same total strain. Because the stress applied was closer to σ^*, a thinner oriented skin layer was observed for rheo-WAXD than for rheo-optical experiments (Figure 3.19). The resulting micrographs of the quenched samples show a transcrystalline layer where the spherulites at the edge of the fine-grained layer grew toward the center of the channel. The boundary between the fine-grained and transcrystalline layer (at ~100 μm) allows us to visualize the depth dependence of shear-induced nuclei and infer the critical stress (~0.09 MPa) for pointlike nucleation induced by shear.[39] (This boundary cannot be seen if samples are quenched prior to the growth of the transcrystalline layer as in Figures 3.15, 3.16, and 3.18).

TEM images of the skin layer of the same samples examined by OM reveal shish-kebab structures (Figure 3.20). The thickness of the bright skin layer observed by OM is consistent with the distance from the surface to the boundary between the row-nucleated region and the spherulitic region seen in TEM images. From a series of TEM images (Figure 3.20A-E) it can be clearly seen that the number of shish-kebabs increases with increasing c and increasing t_s (Figure 3.20D and 3.20F). Thus, evidence strongly supports the notion that the strong, non-linear effect of c on the transient birefringence during shear-

induced crystallization at $\sigma_w > \sigma^*$ is caused by the formation of the shish-kebab structure and the non-linear increase in the number of shish-kebabs, particularly as c/c^* increases from 0.25 to 0.5.

We quantify the length of threadlike precursors per unit volume by measuring the average distance between shish-kebab centers. We determined this thread density from TEM images by counting the number of shish-kebabs in a 2 μm depth range at several distances from the wall (Figure 3.21). The inverse of the square of the distance between centers scales as shish *length/vol*. The thread density saturates at long chain concentration above c^*.

3.4 Discussion

3.4.1 Isolating the effect of long chain content

To clarify the effect of the long chains, it is necessary to compare experiments performed at the same wall shear stress so that the average polymer orientation in the melt during shear is approximately fixed. Using this approach we avoid the difficulty of discriminating the effects of long chain content from the highly non-linear effects of changing the applied stress, which obscure the interpretation of prior studies that made comparisons at fixed deformation rate.[7-11, 15-17] The addition of a small concentration of narrow distribution long chains to a fixed "base resin" exposes their role in oriented crystallization. The utility of this method was demonstrated by Kumaraswamy et al. who showed that long chain content in bidisperse blends was strongly related to the induction of oriented growth by shearing.[18] At fixed stress, and hence roughly fixed average orientation, the long chains become more oriented than average. The relative length of the long and short chains largely determines the disparity in their relaxation times and their orientation states during shear. In contrast to earlier experimental studies in which polymer samples with very broad molecular weight distributions were blended to vary long chain content,[40] Kumaraswamy used relatively well-defined materials. Thus, it was possible to be specific about the relative length of the long chains compared to the bulk ($M_L/M_S \sim 4.5$).

The prior study by Kumaraswamy et al. only examined concentrations above long-chain overlap (2-10%, corresponding to c/c^* of 2.5 – 12.3), and pronounced skin formation was observed for all binary blends investigated (but not for either the short or long polymers alone). The purpose of the present study is to learn more about the mechanism by which long chains affect flow-enhanced crystallization. Here we examine the change in behavior as a function of c both above and below c^* to determine whether the long chain effect is a single-chain effect or cooperative. We further examine the experimental results for evidence of the specific steps in flow-enhanced crystallization in which the longest chains play an important role.

3.4.2 Sequence of events in shear-enhanced crystallization

According to the model of Janeschitz-Kriegl and coworkers,[15] the first stage in shear-enhanced crystallization is the formation of "pointlike" precursors; once formed, sustained shearing can elaborate these "pointlike" precursors into "threadlike" precursors (Figure 3.22). The high aspect ratio of the threads causes lamellar growth from them to be laterally constrained, resulting in formation of a highly oriented, row-nucleated morphology. Our data is qualitatively consistent with this model, and we will discuss our results in the context of this basic physical picture. From the earlier work of Kumaraswamy et al.[18] and the results described above, it is clear that long chains play a central role in the formation of the row-nucleated morphology. Within the framework put forward by Janeschitz-Kriegl, it is essential to know where the long chains are involved in the sequence of events that underlie the creation of this oriented structure.

At what stage(s) are the long chains involved? The observed behavior of the blends indicates that the long chains greatly enhance the growth of threadlike precursors but only mildly enhance the formation of the initial pointlike precursors. Above the threshold stress the elaboration of pointlike nuclei into threads depends strongly on c. TEM images reveal that the number of threads increases with increasing long chain concentration (Figure 3.20), holding T, σ_w, t_s, and γ_w all nearly fixed. As concentration increases from 0 to $0.5c^*$, we observe an increase in thread length per unit volume up to a saturation value that does not change substantially with further increase in long chain concentration up to $2c^*$

(corresponding to approximately 100 nm between thread centers). For B0 and B025, most threads are less than 20 μm long (both ends visible in TEM images), but for B05, B1, and B2 the length of the threads exceeds the field of view (20 μm).

The enhancement of oriented growth due to the addition of long chains indicates that a greater *length/vol* of threadlike precursors form in the binary blends, as is confirmed by electron micrographs (Figure 3.20 and 3.21). Increase in the total length of threadlike precursors per unit volume is accompanied by a decrease in the lateral distance between them. Kinetic consequences of this trend include an increase in the initial rate of formation of oriented crystals (Figure 3.13B). Because all of the observed growth occurred after cessation of flow and the long chain concentration is so low that it does not affect the growth velocity, the quiescent growth velocity is constant across the three experiments. Therefore, the greater the rate of oriented crystallization, the greater the area of the growth front, in accord with the increase in *length/vol* of threadlike precursors. Another consequence of the decreased distance between threads is a reduction of the distance the growth fronts propagate prior to impingement. Since the splay in orientation increases with distance from the shish, reduced distance to impingement leads to a tight orientation distribution.

Further evidence for increased thread length comes from the real-time development of birefringence and oriented crystalline diffraction intensity during crystallization after cessation of shear. The birefringence grows faster for blends with higher long chain concentration and exhibits a saturation effect at higher concentrations, consistent with the *ex situ* TEM findings (Figure 3.10). The increasing birefringence during crystallization is due to the growth of oriented lamellae (kebabs) that occurs after the cessation of flow. The quiescent growth velocity is the same for all blends as indicated by our DSC data, so the accelerated growth of birefringence and parent (kebab) peak amplitude with increasing *c* is a result of higher thread length per unit volume. Therefore, we conclude that long chains enhance the process of thread elaboration, leading to longer threads and higher thread-nuclei density.

The transient birefringence observed during shear also shows that adding long chains enhances the formation of oriented precursors up to concentrations of c^*, with a weak effect upon further addition of long chains. For low concentrations of long chains (B0 and B025, Figure 3.10A, B), the birefringence profile is boxlike, tracking the orientation of chain segments in the melt due to the applied stress. When more long chains are added, there is an "upturn" in the birefringence (beginning at roughly 0.35 s for B05, B1, and B2, Figure 3.10C-D), which prior work has shown correlates with the formation of threadlike precursors and highly oriented α-iPP with c-axis along the flow direction.[35, 36] The "upturn" occurs when a sufficient number of oriented crystallites (combination of "shish" and "kebabs") have formed, causing the birefringence due to crystalline anisotropy to become greater than the birefringence from segmental anisotropy in the melt. Thus, the appearance of the "upturn" for $c/c^* \geq 0.5$ indicates a substantial increase in the number and length of threadlike nuclei with increasing long chain concentration. Unfortunately, the limited sensitivity of rheo-WAXD experiments precludes the detection of crystallites at such early times. However, we observe a correlation between the upturn in birefringence with the appearance of highly oriented α-phase crystallites.

In contrast to the strong effect of c on the formation of threadlike precursors, the effect of long chains on the formation of the pointlike precursors was relatively weak. Below the critical stress required to induce highly oriented growth, the absence of oriented structures observed by *ex situ* microscopy implies that threadlike precursors were not formed or that they were exceedingly short-lived and did not nucleate oriented crystallization. Nevertheless, samples sheared below the threshold stress show accelerated crystallization kinetics compared to quiescent conditions. Indeed, the fine-grained layer seen in samples sheared below σ^* shows an increased number of spherulites when compared with quiescent conditions, consistent with the shear-induced formation of pointlike precursors. The density of nuclei in a sheared melt is a function of stress and temperature. In our isothermal experiment, the stress gradient determines nuclei density and spherulite size, with large spherulites forming at the core where few nuclei develop and a fine-grained layer near the wall (optical micrographs of samples subjected to $\sigma_w < \sigma^*$ not shown). TEM images for

quenched samples sheared at $\sigma_w > \sigma^*$ reveal that, below the oriented skin layer, spherulites at a given depth from the wall (i.e., at comparable $\sigma < \sigma^*$) were approximately the same size regardless of c. Thus, the addition of long chains did not produce a pronounced change in morphology for $\sigma < \sigma^*$, suggesting that long chains do not strongly affect the formation of point-nuclei. *In situ* rheo-optical observations also support this conclusion. The accelerated formation of pointlike precursors at $\sigma < \sigma^*$ is manifested in the development of light scattering at an earlier time than in the quiescent case. The addition of long chains has only a weak effect on turbidity half times for experiments at similar stresses ($\sigma_w < \sigma^*$) and shearing times (Figure 3.23).

On the other hand, rheo-WAXD results highlight a noticeable change in the kinetics of unoriented crystallization, suggesting an increase in the number of pointlike precursors with increasing long chain concentration. The onset of isotropic crystallite growth occurred earlier for B1 than B05 (and B0), although the ratio of isotropic crystallites was only marginally lower for B05 at 1200 s, the time at which the total transmitted intensity of light in rheo-optical experiments was nearly 0. Since we were unable to obtain rheo-WAXD results for B025 or B2, we can not clearly distinguish the nature of the dependence of pointlike precursors on long chain concentration. However, it is clear that the presence of long chains affects the kinetics of isotropic crystallization, but perhaps only slightly. Therefore, it seems that the turbidity half-time is too insensitive to be a good indicator of the number of pointlike nuclei. For the (very low) concentration range we examined and the given length of long chains, we maintain that the effect of long chain concentration on the formation of pointlike precursor formation is weak compared with its effect on threadlike precursor formation. The long chains likely exert a stronger influence at higher concentrations than those used here or when the long chains have higher M_w.

3.4.3 Molecular perspective on shear-enhanced crystallization

3.4.3.1 Formation of pointlike precursors

Even at low stress levels, flow greatly enhances the crystallization kinetics of a polymer melt by increasing the number of pointlike nuclei. The mechanism by which these crystallization precursors are formed is unknown, but the results indicate that the

mechanism does not preferentially involve the most oriented chains in the melt (the long chains). Put another way, it appears that the average level of segmental orientation is the dominant factor in determining their rate of formation, since the rate appears to be governed by the local stress (~average orientation), nearly independent of the concentration of long chains. The low concentration of long chains in our blends will only slightly alter the average orientation and so lead to a slight increase in pointlike nucleation. Thus, the experimental results negate our initial hypothesis that the addition of long chains would greatly enhance the formation of pointlike nuclei following shear as a result of the stronger orientation of the longest molecules due to their long relaxation times. Similarly, Somani et al.[6] have hypothesized that for "orientation-induced crystallization, a certain degree of molecular extension must be achieved to induce formation of stable primary nuclei," and for a "particular $\dot{\gamma}$, only the longer chains will be oriented." If this were the case, the addition of long molecules would increase the amount of oriented material as well as the number of primary nuclei. Alternatively, Janeschitz-Kriegl and coworkers suggested that the pointlike precursors form by the coalescence of "athermal nuclei" during shear, tracking the applied strain rather than the degree of molecular orientation.[41] This mechanism is expected to be insensitive to the addition of long chains, in accord with these results. However, the "athermal nuclei" hypothesis does not accord with the observed temperature dependence of precursor formation reported by Kumaraswamy.[18, 35]

The α-modification of crystalline iPP is a complex arrangement of molecules composed of 3_1 helices with alternating handedness packed into a monoclinic unit cell.[42] Although shear cannot generate this precise structure, the local ordering of segments due to flow increases the likelihood that chains may adopt a long-lived structural arrangement due to thermal motion. The accelerated formation of pointlike precursors occurs sporadically at a rate that is controlled by the average segmental orientation. The fact that the presence of highly oriented long chains does not greatly affect this rate implies that many chains are involved, sampling a significant portion of the overall orientation distribution.

3.4.3.2 Formation of threadlike precursors

The primary mechanism by which long chains enhance the formation of row-nucleated structures appears to be the elaboration of pointlike precursors into threads. When the applied shear stress exceeds the critical shear stress, threadlike precursors form. The fact that the threshold stress σ^* initially decreases with addition of long chains shows that the presence of these slower relaxing molecules enhances the elaboration of pointlike precursors into threads. The decrease in the sensitivity of the process to addition of long chains beyond the overlap concentration indicates that the effect of long chains is a cooperative one that increases significantly as the probability of long chain-long chain overlap increases.

Why are long chains preferentially involved in elaboration into threads? If we consider the propagation of a threadlike precursor from a pointlike precursor, we envision that adjacent chains in the melt interact with the surfaces of a given pointlike precursor. Suppose that an adjacent chain adsorbs to a surface normal to the gradient direction: the free segments of such a chain will subsequently become elongated due to sustained shear (Figure 3.24a). Chain segments convected along a streamline with lower velocity relative to the attachment point will lag behind, while those segments on the higher velocity side will be extended downstream. If a number of chains become tethered to the pointlike precursor, this process will create a substantial number of oriented segments upstream and downstream of the particle (Figure 3.24b). Although full extension is unlikely, the strong orientation enhances the likelihood of subsequent nucleating structures forming along the line of flow (Figure 3.24c). Thus, the same process can repeat itself over and over again, leading to a train of precursor clusters connected into a thread (Figure 3.24d).

Long chains might greatly enhance this process for three reasons. First, their segments are more oriented than average, which might put them in a preferred state for adsorption onto a precursor surface. Second, simply by virtue of having more segments per molecule, they are more likely to adsorb. Third, once adsorbed, they provide more segments to participate in "streamers" dangling upstream or downstream (Figure 3.24b), and these segments will be more oriented on average than those of shorter "streamers."

After cessation of shearing, lateral growth continues from the threadlike precursors (Figure 3.24e). Since relaxation of chains in the melt occurs quickly after cessation of shearing, the growth velocity is expected to be that of the quiescent case.

Why is the threshold stress insensitive to long chain concentration? We expected σ^* to decrease substantially with increasing long chain concentration over the range tested due to stronger relative orientation and proximity of long chain segments. Instead we see a threshold stress that only decreases ~10% as c increases to $0.5c^*$ and is almost unchanged with further increase to $2c^*$ (Figure 3.8). The schematic picture in Figure 3.24 may provide insight into the reason(s) that addition of long chains enhances the formation of threads, yet the threshold stress does not change with long chain concentration. First, the threshold stress may correspond to one that induces sufficient segmental orientation of the long chains to significantly enhance the rate of adsorption onto precursor surfaces (Figure 3.24a). This threshold is insensitive to c over the range probed because the relaxation time of the long chains does not increase greatly from that of isolated long chains in a short chain matrix (even at $2c^*$ there is little long-long entanglement). Second, the threshold stress may be the value that induces sufficient orientation of the "streamers" to trigger rapid propagation of threads up and downstream of a given precursor (Figure 3.24b-c). In this case the threshold stress would be insensitive to the long chain concentration for the same reason as for the shear induced orientation of long chains in the melt: the relaxation dynamics of a long chain tethered to a precursor are insensitive to long chain concentration until long-long entanglement becomes significant.

Why is the effect of long chains cooperative? There are two ways in which reaching long chain-long chain overlap might be significant. First, the probability of a particularly strong local enhancement of orientation due to overlap of the "orientation clouds" represented by individual long chains becomes increasingly likely to occur. In view of our speculation about the way the threads propagate, the multi-body interaction may be among long chain "streamers" trailing from pointlike precursors. Second, the relaxation time of the long chains increases with increasing long chain-long chain interaction, particularly with the inception of long chain-long chain entanglement. As the long chain relaxation time

increases with c, the orientation of the long chains also increases, particularly for c low enough that the mean relaxation time is hardly perturbed (so the deformation rate under a given stress remains nearly that of the pure short chains). Similarly, if a long chain adsorbs to the surface of a precursor, the degree of orientation of the resulting "streamers" will be higher if the strands are entangled with surrounding long chains that are being swept by in the flow.

Why don't shish tumble? A striking feature of the row-nucleated morphology is that the threadlike precursors are well-oriented along the flow direction. If they tumbled with the vorticity of the shear flow, it is unlikely that they could attain the lengths seen in micrographs or exhibit the strong, uniform orientation that is observed. It may be that the threads do not tumble because they are elongating continuously. For long, slender particles, the tumbling period, which is deduced from Jeffery orbit for rod-like particles,[43] increases strongly with increasing length of rods. We suspect that the threadlike precursors may grow sufficiently quickly that their tumbling period effectively becomes infinite (long compared to t_s) before they tumble. The shish formed in B025 after shearing at 0.12 MPa for 1.0 s were not completely straight (Figure 3.25A), whereas the shish formed in B2 after shearing at 0.12 MPa for 0.75 s were quite straight and thin (Figure 3.25B), perhaps reflecting the difference in thread growth velocity in these samples.

Why does the concentration of threads saturate? It is interesting that the addition of long chains beyond c^* to $2c^*$ produces little further enhancement of the formation of threads. This may be related to a morphological feature observed *ex situ*. The distance between centers of neighboring shish in the region where shish are most densely packed was determined from TEM images. For the same conditions (σ_w = 0.12 MPa; comparable strain units corresponding to $w_{ex} \approx$ 100 mg) the shortest distance between shish for B0 was 200 nm and for all other blends 100 nm. Since TEM images average over the thickness of the ultra-thin sections, the actual spacing between the threads may be greater than this apparent value. Nevertheless, the distance between threads seems to saturate as c increases. We see two general mechanisms that might be involved in this saturation effect. First, once the threads reach a sufficiently high density, they may hinder each other's further growth

(perhaps growing threads strike lateral lamellae propagating from neighbors). Second, at the tip of a growing thread, locally like a pointlike precursor, there may only be sufficient surface area for adsorption of a small number of chains. As the concentration of long chains increases, they may fully occupy the available surface, causing the propagation velocity of the threads to saturate.

3.4.3.3 Comparison to existing concepts regarding long chains

Somani et al.[6] have offered a molecular picture for nucleation and growth induced by transient shearing mediated by chains above a critical orientation molecular weight M^*. In their results, stacked lamellae oriented perpendicular to the flow direction were observed by TEM. Assuming the power law relationship between the shear rate and M^* ($M^* \sim \gamma^{-a}$) given by Keller,[5,44] they estimated M^* from the fraction of the oriented crystalline lamellae. Implicit in this analysis is the assumption that "only polymer molecules having a molecular weight above a critical orientation molecular weight M^* can form oriented structures" at a given shear and that all chains above M^* are in these oriented crystals. In a subsequent paper[40] they argue that incorporation of short molecules into the oriented crystals may not take place. The present results show that the amount of oriented crystalline material (approximately half of the polymer in the oriented skin) can greatly exceed the amount of long chains (less than 1.5% in the present blends) that are involved in templating the oriented growth. Physically, this result suggests that it is sufficient to create a very dilute quantity of threads to template oriented growth which incorporates chains of all lengths as the growth front advances.[33]

Keller et al.[5,44] ascribed the mechanisms for formation of threadlike structures to a coil-stretch transition of long molecules from random coils to extended conformations which can then solidify into fibrillar crystals. His explanation of a coil-stretch mechanism at work during simple shear flow was based upon studies in extensional flow, where shish were shown to be the result of extended chain crystals. In shear flow, Keller hypothesized that extension of long chains would result between entanglement constraints imposed by the surrounding molecules. Our data suggest multi-body interactions of long chains play a significant role during the formation of threads, exhibiting a non-linear increase in the

number of threads with increasing *c*. While we do not believe a coil-stretch transition occurs during shear, the nonlinear dependence on long chain concentration may indicate that long chain-long chain entanglement plays a role consistent with the partial extension of segments of the long chains due to topological constraints described by Keller.

The concept of coil-stretch can not be completely ruled out, however. Intriguing experiments by Chu and coworkers[45] examined of the conformational dynamics of λ- DNA molecules fluorescently labeled to allow direct microscopic observation in a shear flow. Molecules in shear flow did not show a distinct coil-stretch transition such as occurs in extensional flow, but at high shear rates individual molecules were observed to explore largely extended fluctuations. However, the mean fractional extension never rose higher than 0.4, as the stretched state is destabilized by the rotational component of the shear flow which causes the molecules to tumble. This leaves open the possibility that some long chains in our blends may achieve a partially extended state and that this contributes to the formation of oriented precursor structures.

3.5 Conclusions

Blending well-characterized iPP into a "base iPP" is a useful way to determine a relationship between characteristics of specific molecules and their role in the crystallization process.[18] Using this approach we have shown that blends with less than 1% of chains with M_w five times larger than the M_w of the base resin have profoundly affected the crystallization kinetics and crystalline morphology of a sheared melt. Beyond unambiguously demonstrating the important role of long chains in the formation of anisotropic crystallization under flow, this approach allows us to be specific about the length that is meant by "long chains" and the concentration of these chains in the melt.

Varying the concentration from below to above c^* revealed that the effect of the long chains involves cooperative interactions, evident in the non-linear relationship of the long chain concentration particularly as c approaches the long chain-long chain overlap concentration. The long chains greatly enhance the formation of threadlike precursors, but only mildly enhance the formation of pointlike precursors.

Table 3.1 Blend Composition and Thermal Properties

blend	c [a] (g/cm^3)	c / c^* [a]	T_c [b] (°C)	ΔH_f [b] (J/g)	T_m [c] (°C)
B0	0	0	113.1	84.3	143.8
B025	1.76×10^{-3}	0.25	112.2	86.7	143.8
B05	3.51×10^{-3}	0.5	112.7	83.5	143.7
B1	7.00×10^{-3}	1.0	111.9	84.5	143.6
B2	1.39×10^{-2}	2.0	112.9	86.2	143.8

[a]Concentration of L-PP (c) and the critical concentration of L-PP obtained from eq. 1 in the main text. [b]Crystallization temperature (T_c) and heat of fusion (ΔH_f) determined by the exothermal peak position and calorific value of DSC with the constant cooling condition of 5°C/min from the melt (220°C). [c]Apparent melting temperature (T_m) was determined by the peak temperature of DSC on second heating with heating rate of 5°C/min.

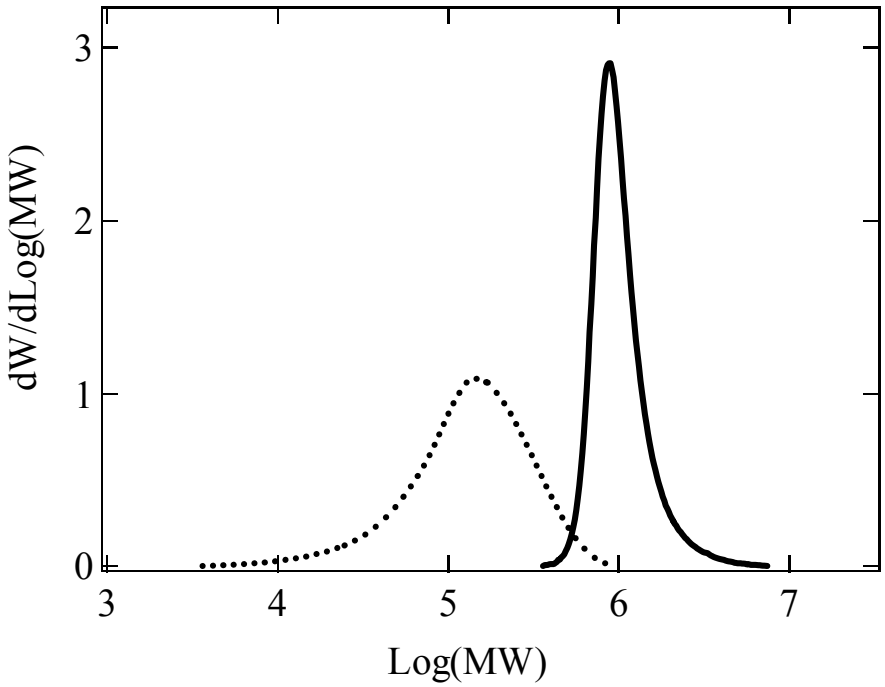

Figure 3.1: Molecular weight distribution for Base-PP (dotted line) and L-PP (solid line) measured by GPC-MALLS.

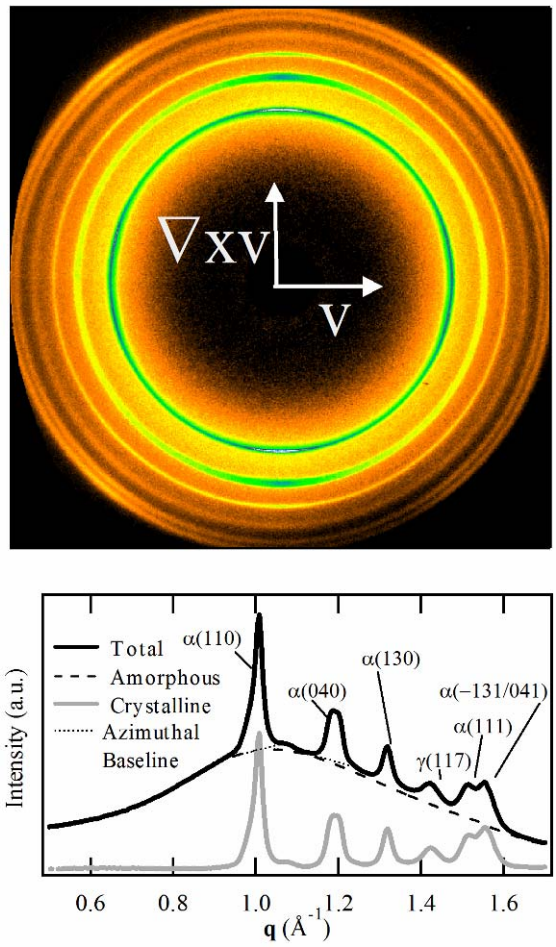

Figure 3.2: Circular average of 2-D WAXD patterns. Two-dimensional WAXD patterns are collected using a MarCCD camera (top). A circular average of intensity vs. **q** is extracted (bottom) and crystalline peaks are identified. The crystallinity index (x_c) is calculated by separating the crystalline and amorphous fractions of the circular average. The amorphous portion (dashed line) is approximated by the scattering profile of the amorphous polymer melt (prior to shearing), scaled appropriately. The profile of diffraction from crystalline material (grey curve) is taken to be the difference between the total intensity and the amorphous contribution. Subsequent analysis of the azimuthal dependence of crystalline diffraction uses a linear approximation (dotted lines) of the amorphous halo.

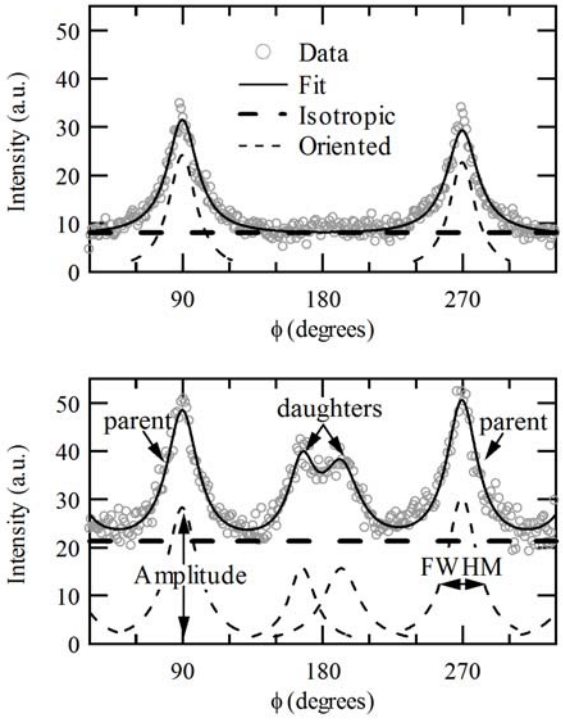

Figure 3.3: Azimuthal scans of the 040 (top) and 110 (bottom) planes and fits. Crystallite orientation is analyzed by fitting the azimuthal peaks with Lorentzian peak shapes and extracting the relevant peak parameters (i.e., peak amplitude, FWHM). The 040 peaks are fit first and used to set the isotropic baseline since the peaks are sufficiently separated that no peak overlap occurs. The fraction of isotropic to oriented intensity in the 040 scan is used to determine the isotropic baseline for the 110 scan. After removing the 110 isotropic baseline, the parent and daughter 110 peaks are fit with Lorentzian shapes. The parent:daughter ratio is calculated from the peak amplitudes. The FWHM measures the distribution of orientations.

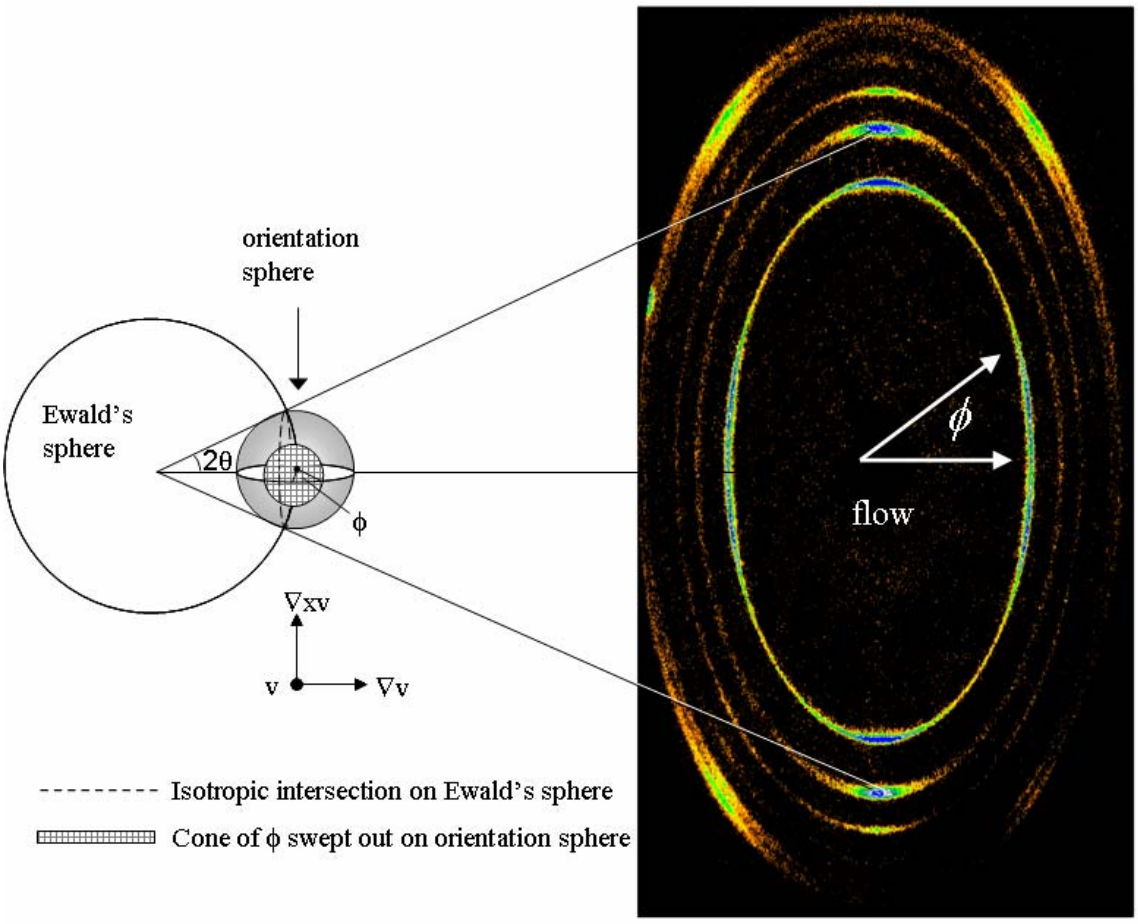

Figure 3.4: Geometry demonstrating the intersection of the Ewald's sphere with the orientation sphere. This axis of the orientation sphere is directed out of the page and is coincident with the velocity direction in our experiment. The dashed line denotes an isotropic intersection of the orientation sphere with the Ewald's sphere and will project a ring on the 2-D flat image at the right. The hashed circle is a projection of the cone of ϕ that the uniaxially oriented crystals trace out on the orientation sphere. The intersections of this cone with the dashed line (on the Ewald's sphere) will project arcs on the 2-D WAXD image.

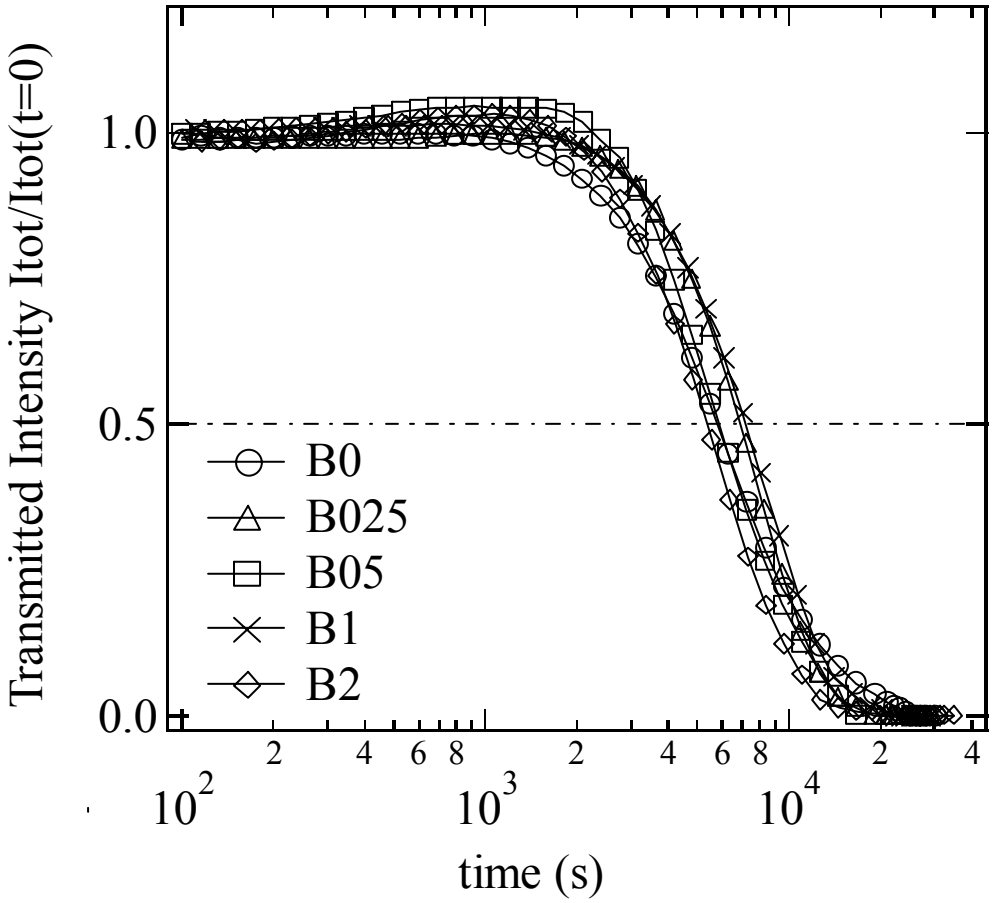

Figure 3.5: Turbidity of blends crystallized quiescently at 137 °C.

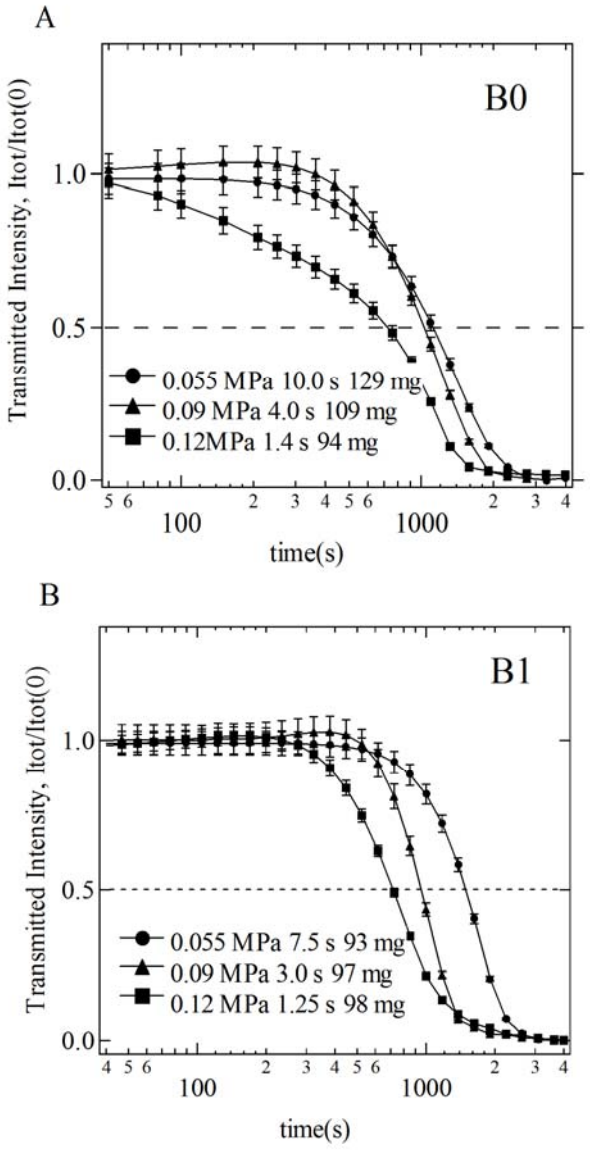

Figure 3.6: Turbidity of (A) B0 and (B) B1 during crystallization after short term shearing (t = 0 defines beginning of shear) at T_c = 137 °C and various wall shear stresses for maximum shearing time (extruded mass was about 100 mg).

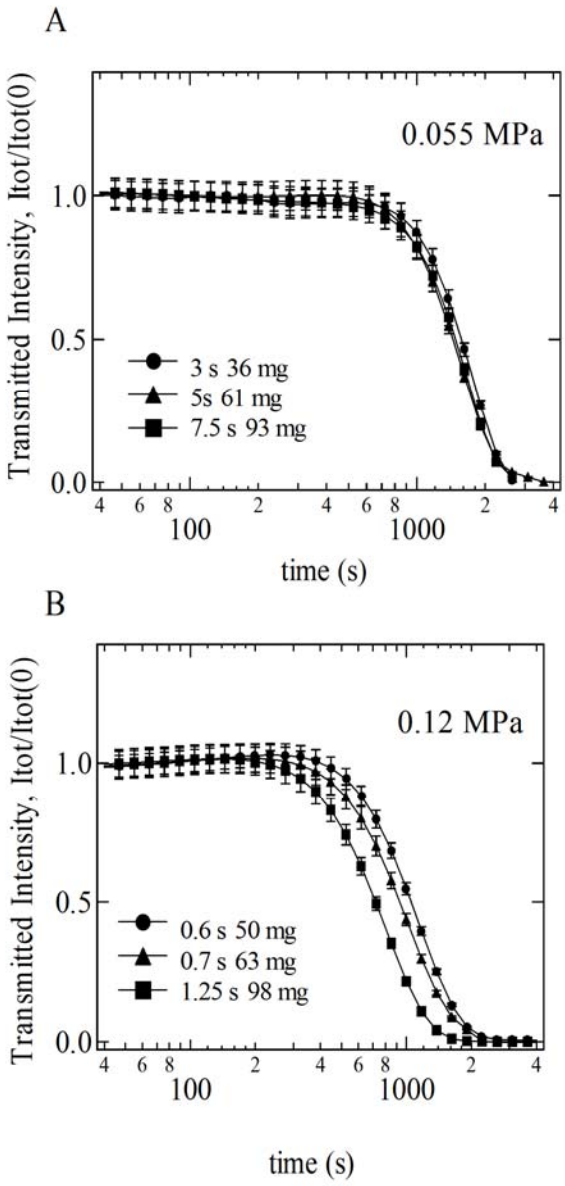

Figure 3.7: Turbidity of B1 during crystallization after short term shearing at T_c = 137 °C for σ_w of (A) 0.055 MPa and (B) 0.12 MPa for various shearing time.

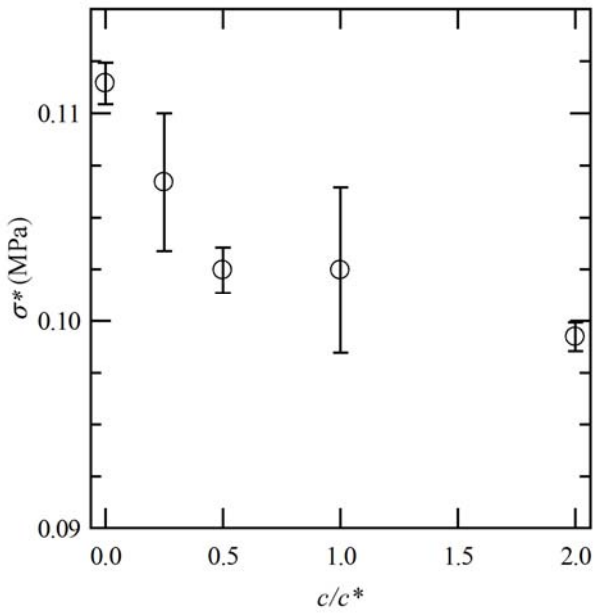

Figure 3.8: The critical shear stress (σ^*) needed to induce the transition to oriented growth is plotted against long chain concentration (c/c^*). The value for σ^* was determined by measuring the depth of the highly birefringent skin in polarized light micrographs. The error bars indicate variation in the skin thickness rather than measuring error.

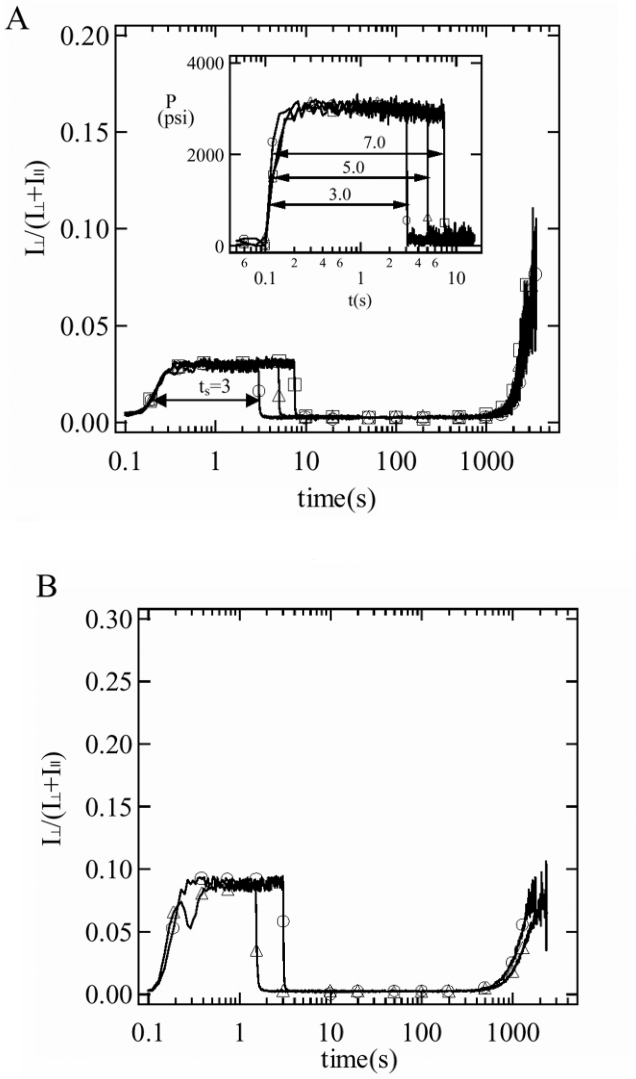

Figure 3.9: Relative intensity through crossed polarizers ($I_{\perp}/I_{tot}$) of B1 during short term shearing at 137 °C and during the crystallization after cessation of shear. The inception of shear is taken to be t = 0.1 s since the first relevant decade is 0.1-1 s. (A) A shear pulse with σ_w = 0.055 MPa was applied for (○) 3.0 s, (Δ) 5.0 s, and (□) 7.5 s, corresponding to w_{ex} (mass extruded ~ total strain) of 36, 61, and 93 mg, respectively. (B) A shear pulse at σ_w = 0.09 MPa was applied for (○) 3.0 s and (Δ) 1.5 s, corresponding w_{ex} was 47 and 97 mg, respectively. A "boxlike" pressure profile was imposed during t_s (inset in A).

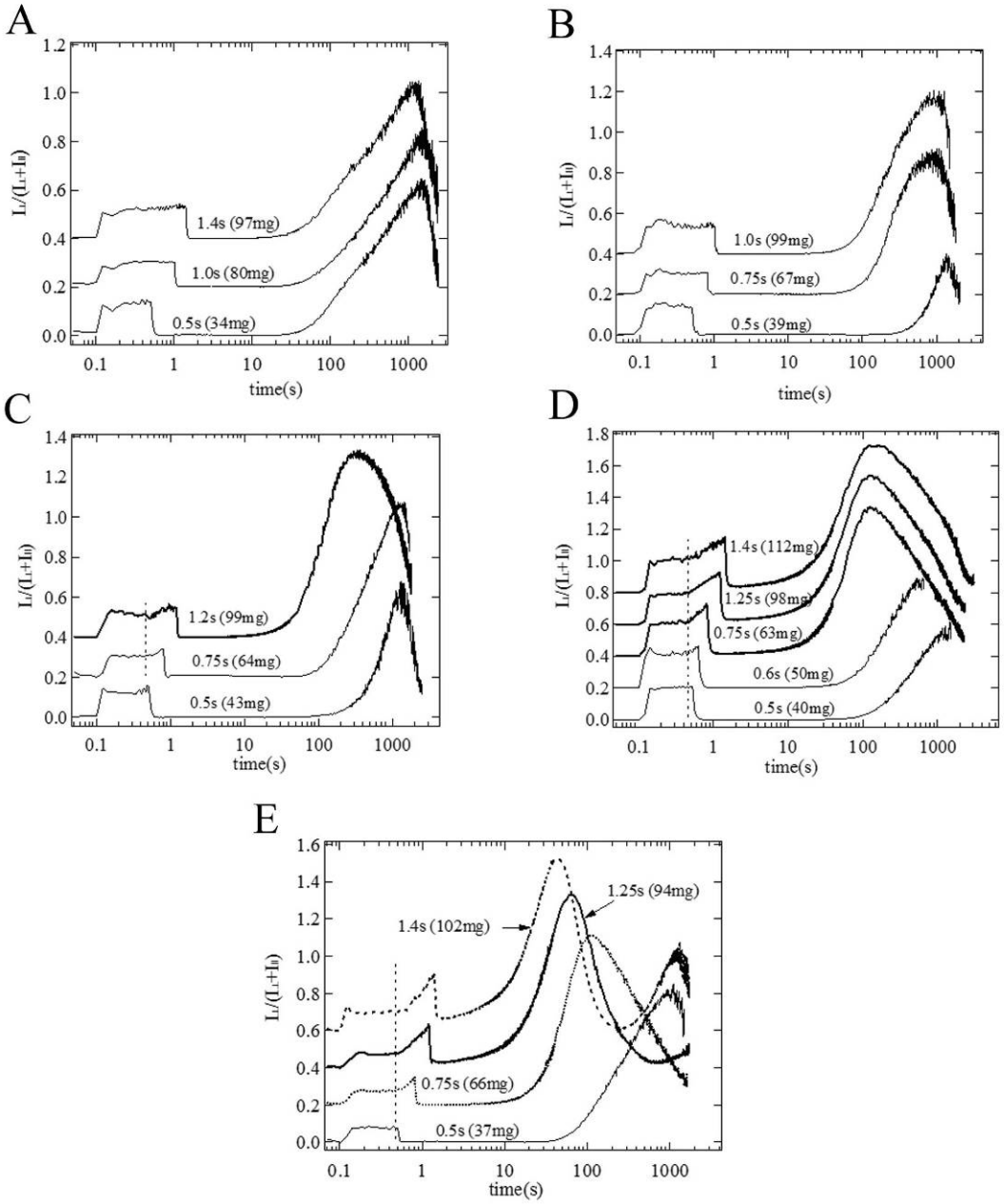

Figure 3.10: Relative intensity through crossed polarizers ($I_{\perp}/I_{tot}$) of (A) B0, (B) B025, (C) B05, (D) B1, and (E) B2 during and after short term shearing at 0.12 MPa and 137 °C is plotted against time. Time is offset by 0.1 s and relative intensities have been shifted progressively by a factor of 0.2 for clarity. Shearing time and w_{ex} are given above each trace. Dotted lines in figures indicate the time when the birefringence upturn during shear can be observed.

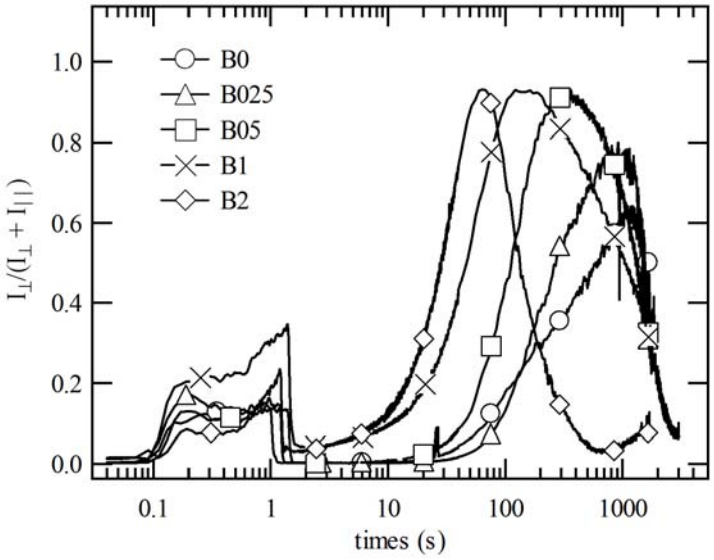

Figure 3.11: Relative intensity through crossed polarizers ($I_{\perp}/I_{tot}$) vs. long chain concentration (c/c^*) of blends crystallized at 137 °C with σ_w = 0.11 MPa. Shearing times are 1.4 s, 1.0 s, 1.2 s, 1.4 s and 1.25 s for B0, B025, B05, B1, and B2, respectively. Time is offset by 0.1 s for clarity.

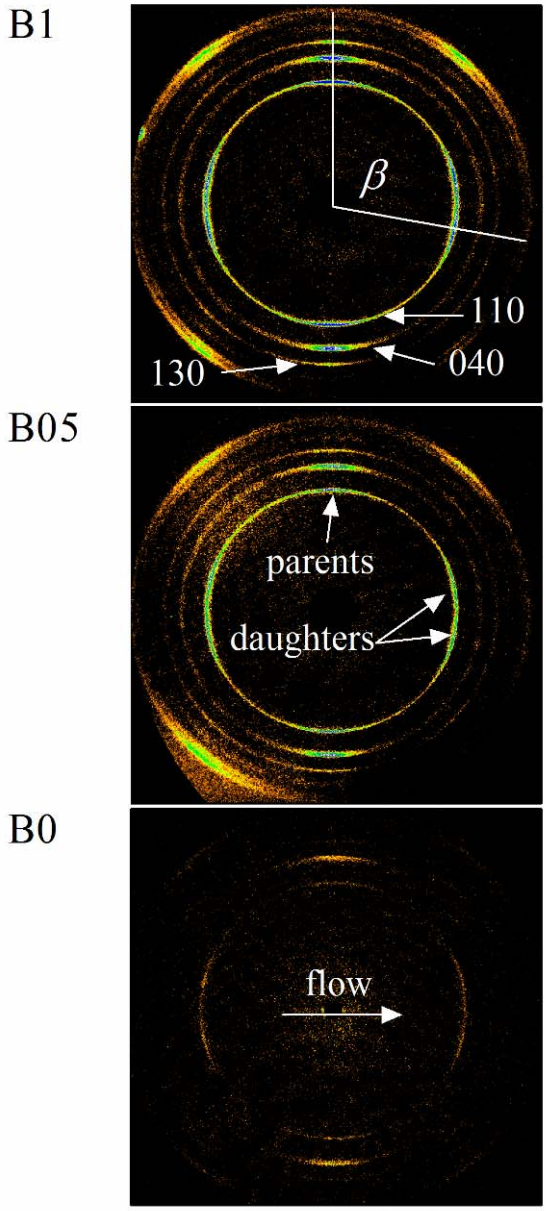

Figure 3.12: Two-dimensional WAXD patterns acquired at 1200 s after shearing at σ_w = 0.11 MPa for B0 (t_s = 1.7 s), B05 (t_s = 2.0 s), and B1 (t_s = 2.2 s). The acquisition time was 30 s and the patterns have been deconvoluted from the amorphous scattering halo and retain crystalline diffraction only. Parent and daughter crystalline peaks are evident on the 110 plane. The β-angle of the monoclinic unit cell of α-iPP (99.62°) is shown for reference. Daughter peaks along 130 are not distinct. (The flow direction coincides with the equatorial direction; the meridional direction is vertical.)

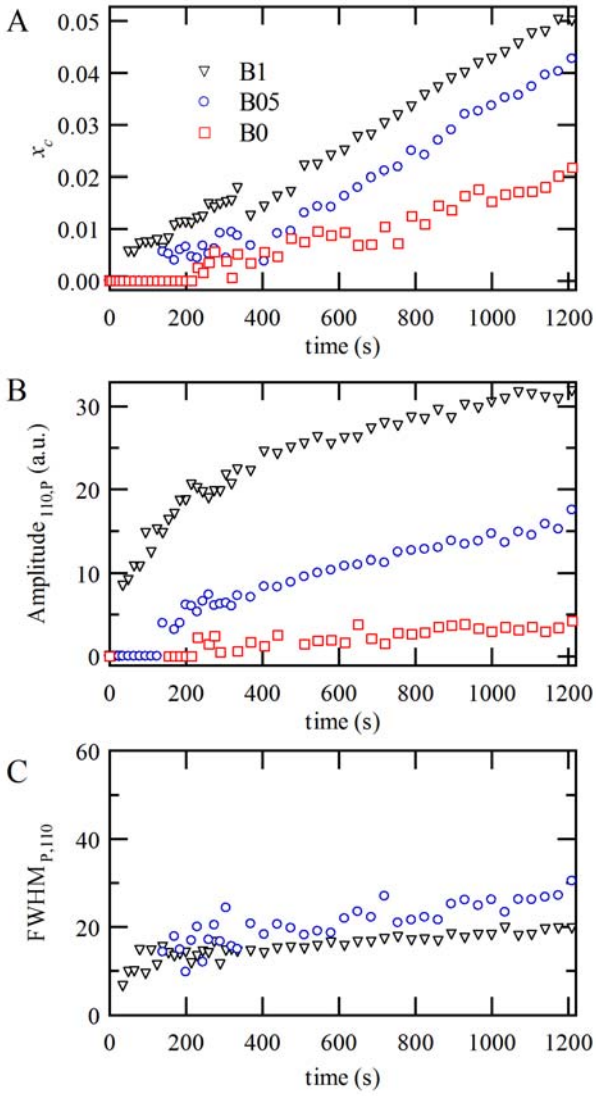

Figure 3.13: Real-time rheo-WAXD analysis of crystallization kinetics. For σ_w = 0.11 MPa > σ^*, increasing long chain concentration causes an increase in A) crystallization kinetics evident by crystallinity index, x_c, B) amplitude of parent peaks, and C) the FWHM of parent 110 peaks. Peaks for B0 were too ill-defined to confidently assign a FWHM from fits. The shearing time and wall shear stress (and mass extruded) for each experiment are: t_s = 1.7 s, σ_w = 0.11 MPa,(w_{ex} = 89.8 mg) for **B0**; t_s = 2.0 s, σ_w = 0.107 MPa, (w_{ex} = 98.3 mg) for **B05**; and t_s = 2.2 s, σ_w = 0.108 MPa, (w_{ex} = 108 mg) for **B1**. The break in x_c at 375 s is an artifact of data collection where the acquisition time change from 10 s to 30 s.

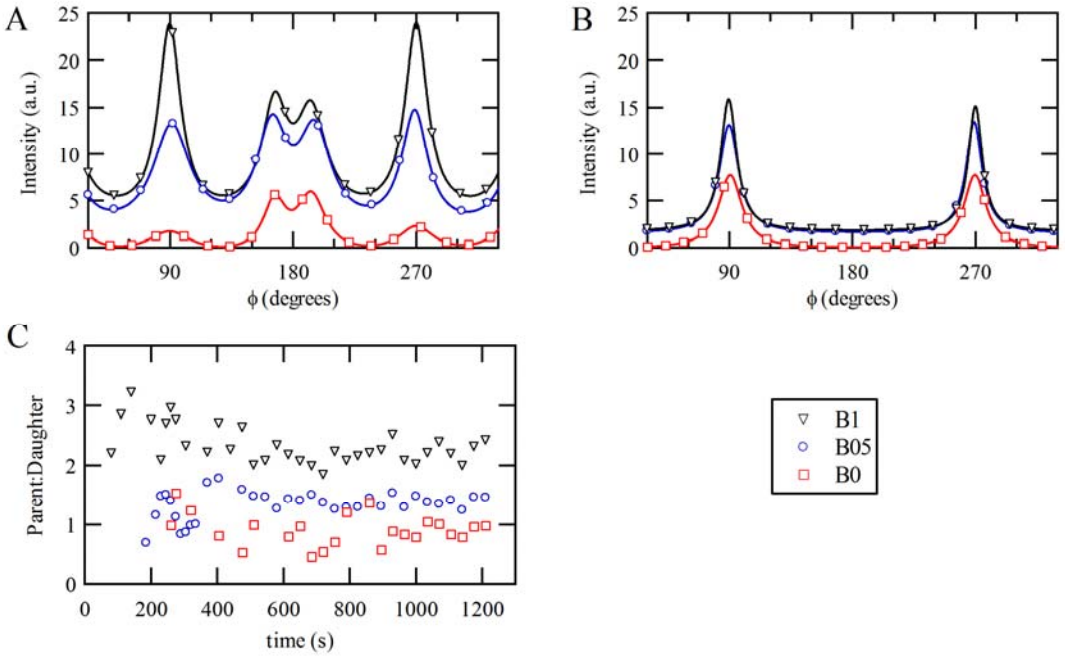

Figure 3.14: Fits of 110 and 040 azimuthal scans show the dependence of oriented crystallization on long chain concentration. A) Fits to the raw azimuthal scans of 110 crystalline reflection at 1200 s after shear. The non-zero isotropic baseline in B) fits of the 040 azimuthal scans for B05 and B1 shows the enhancement in the growth of isotropic crystallites compared to B0. C) The parent:daughter ratio (after correcting for ϕ dependence) strongly depends on long chain concentration (c).

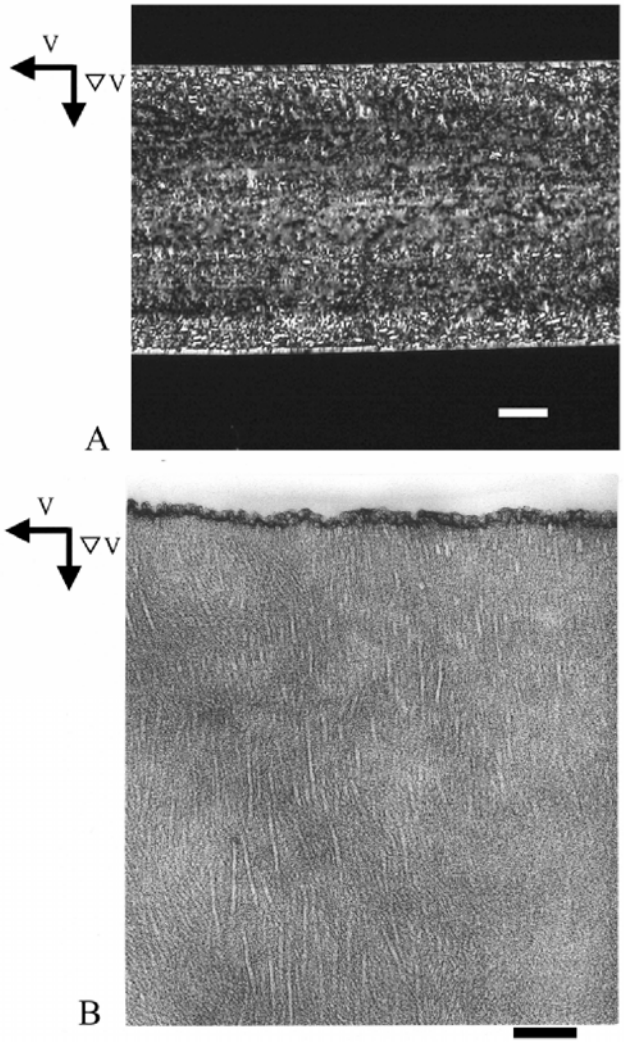

Figure 3.15: (A) Optical and (B) transmission electron micrographs of B2 crystallized at 137 °C after shearing at σ_w = 0.055 MPa for t_s = 7.5 s, corresponding to w_{ex} = 98 mg. Scale bar is (A) 100 μm and (B) 100 nm.

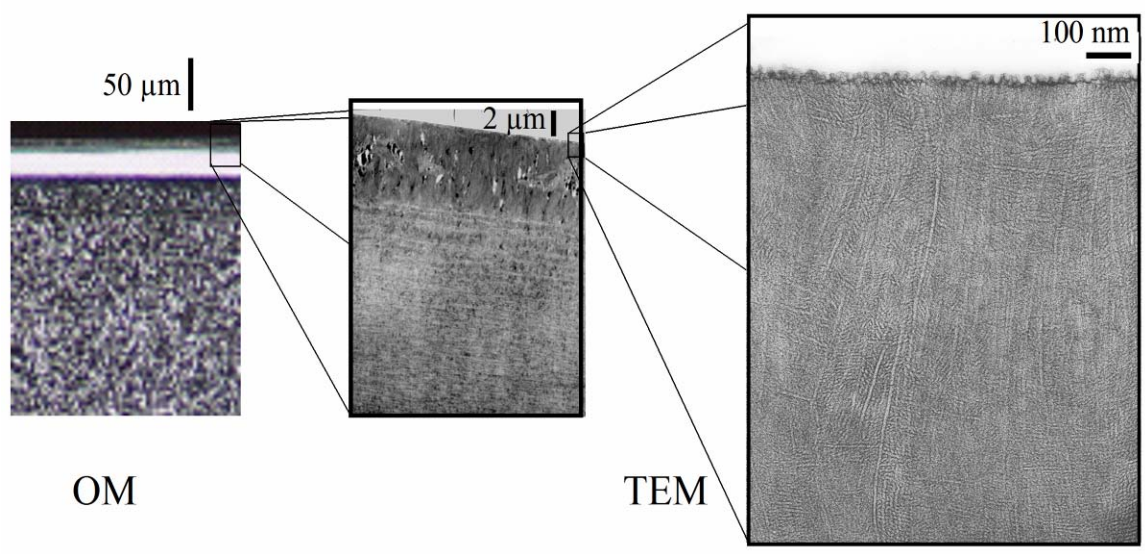

Figure 3.16: Optical and electron micrographs of dense lamellar layer near cell wall in B1 sheared for 1.4 s at σ_w = 0.11 MPa. A 6 μm layer near the wall appears dark between crossed polarizers (left). At larger magnification (center), the layer is distinctly different from the row nucleated structures farther from the wall. At the highest magnification (right), individual cross-hatched lamellae are distinguishable. The significant cross-hatching explains the lack of birefringence from this layer. Length scales are indicated in image.

Figure 3.17: TEM of B0 crystallized quiescently at 137 °C on the surface of a quartz window. The lamellae are not ordered like those that occurred following flow. No transcrystalline layer emanates from the glass, indicating that it does not act as a nucleating surface; instead, the lamellae are part of large spherulites centered away from the glass interface. The scale bar is 100 nm.

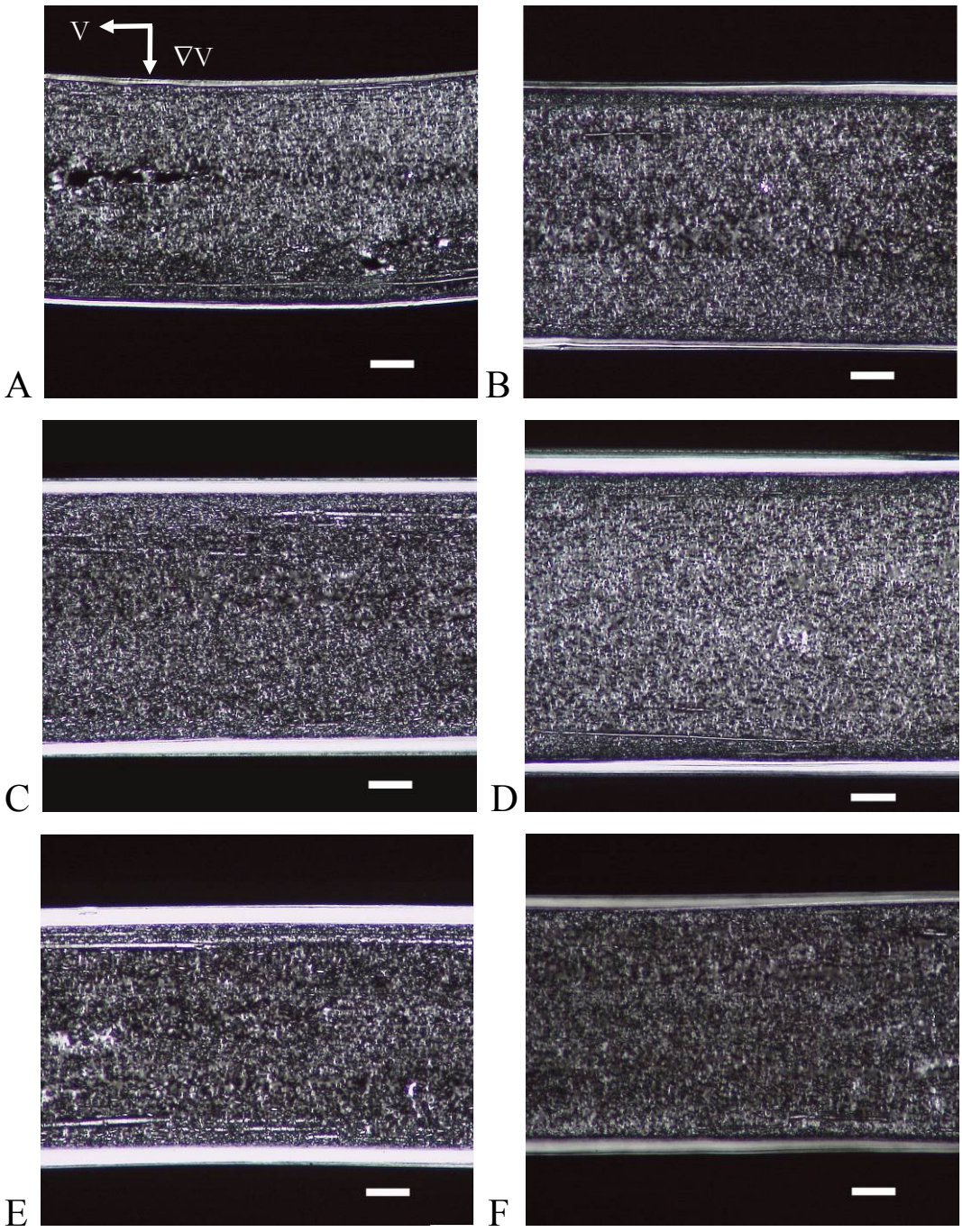

Figure 3.18: Optical micrographs of (A) B0, (B) B025, (C) B05, (D) B1, (E) B2, and (F) B1 crystallized at T_c = 137 °C after shearing at σ_w = 0.12 MPa for t_s = (A) 1.4 s, (B) 1.0 s, (C) 1.2 s, (D) 1.4 s, (E) 1.0 s, and (F) 0.6 s. The corresponding w_{ex} were 97, 99, 99, 112, 91, and 50 mg, respectively. The samples were quenched after crystallizing for (A) 1855 s, (B) 1611 s, (C) 1667 s, (D) 2899 s, (E) 1690 s, and (F) 550 s. The *in situ* birefringence and TEM images are presented in Figures 3.10 and 3.20. Scale bars are 100 μm.

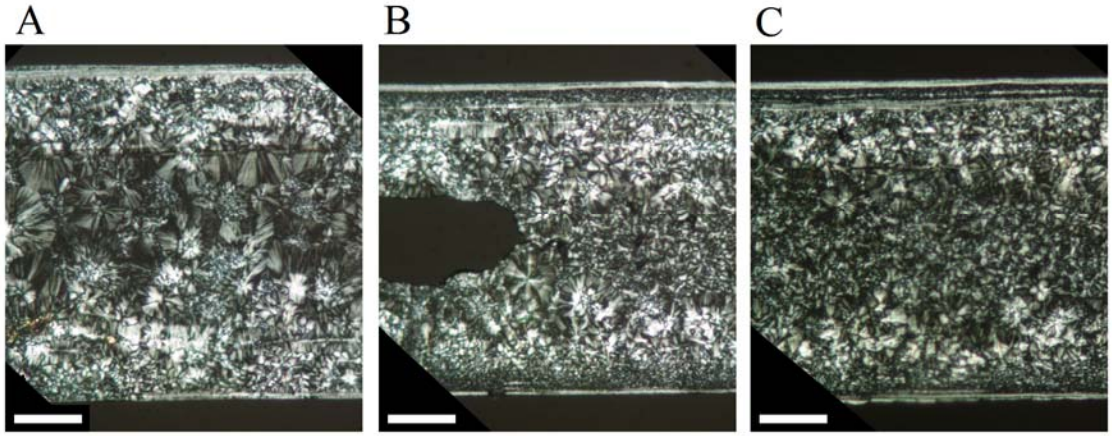

Figure 3.19: Optical micrographs of A) B0, B) B05, and C) B1 which were crystallized isothermally for 5000 – 6000 s following shear in rheo-WAXD experiments before being quenched. Note the contrast between the edge of the fine-grained layer and the sample core. Scale bars are 100 μm.

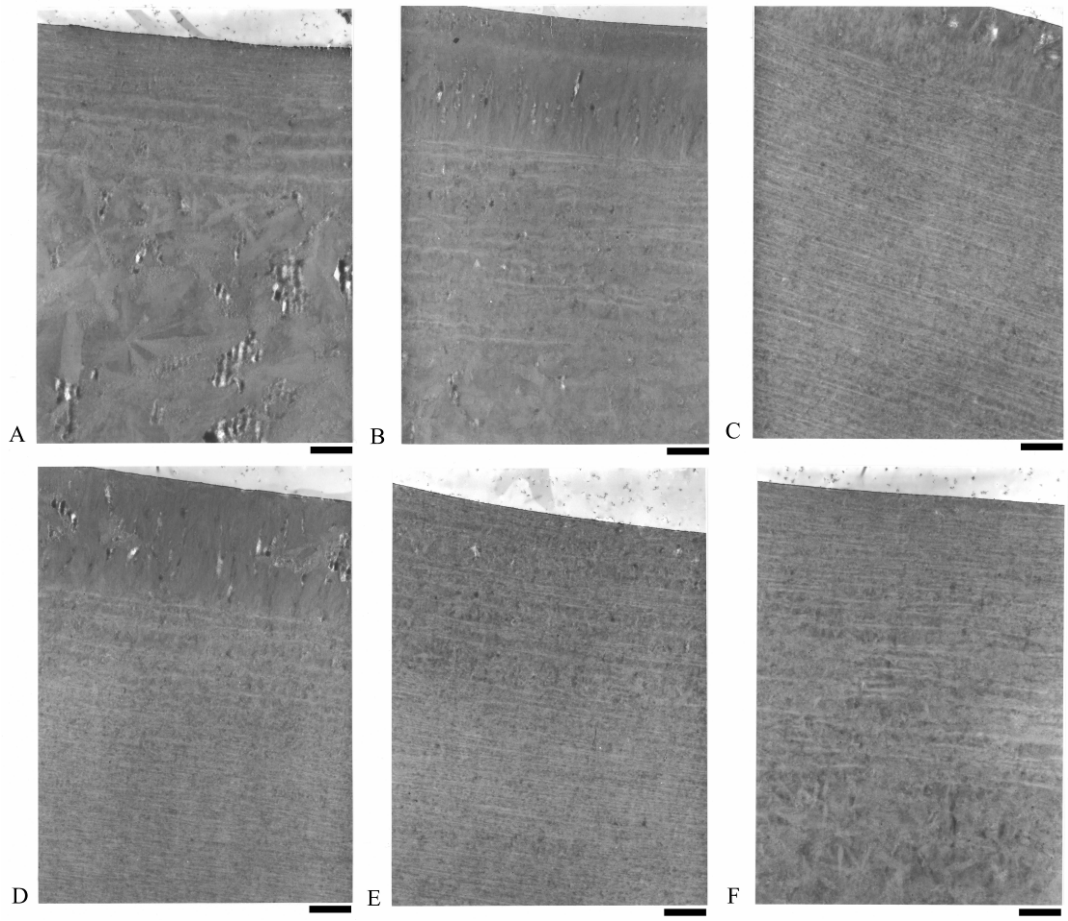

Figure 3.20: TEM micrographs of the skin layer of (A) B0, (B) B025, (C) B05, (D) B1, (E) B2, and (F) B1 for the same conditions as Figure 3.18. The flow direction is parallel to the edge of the sample shown as the boundary between the sample (gray) and the embedding material (white). Sections were cut in the plane of the flow and velocity gradient directions. Scale bars are 2 μm.

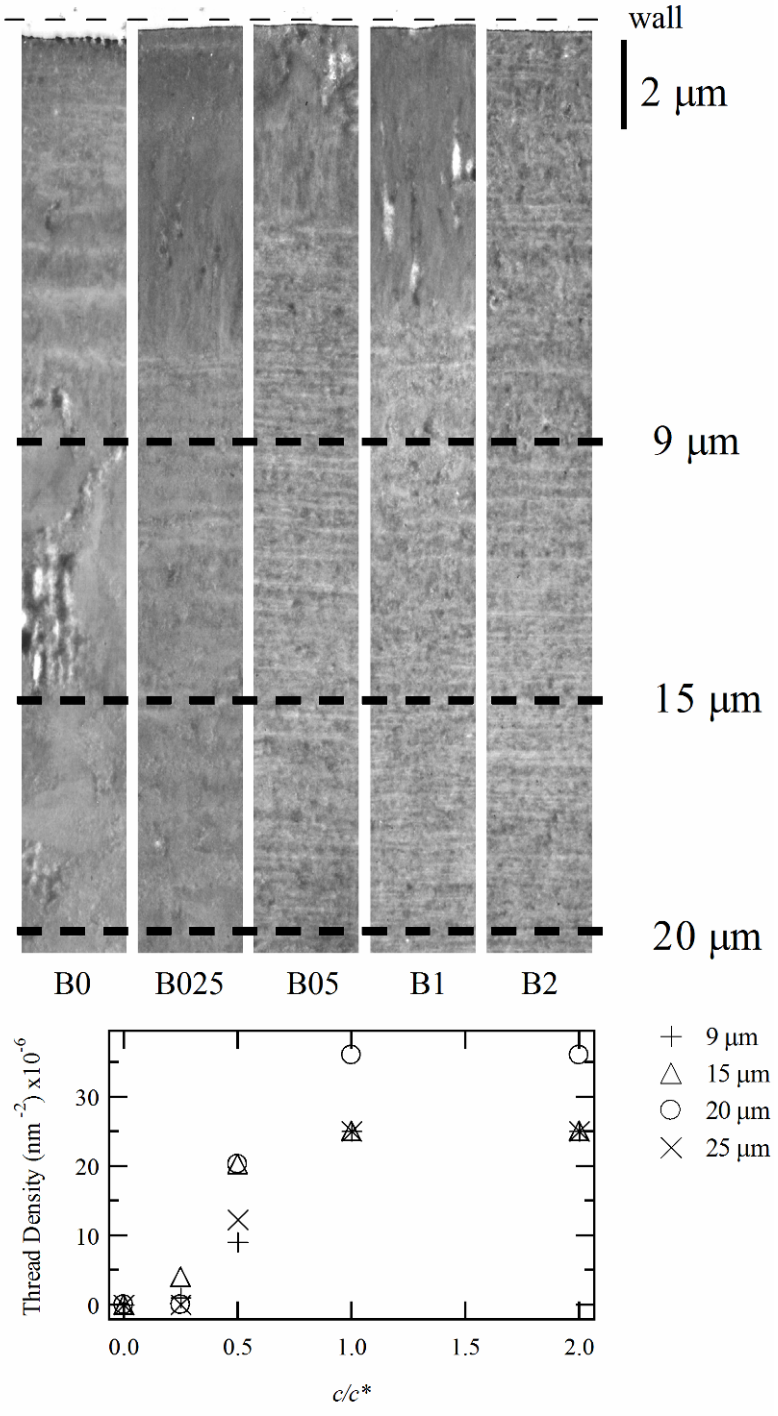

Figure 3.21: Thread length per unit volume determined from TEM. Average shish-kebab spacing gathered from closer examination of TEM (top) from Figure 3.20A-E at several depths from the wall was used to estimate the threadlike precursor density (bottom).

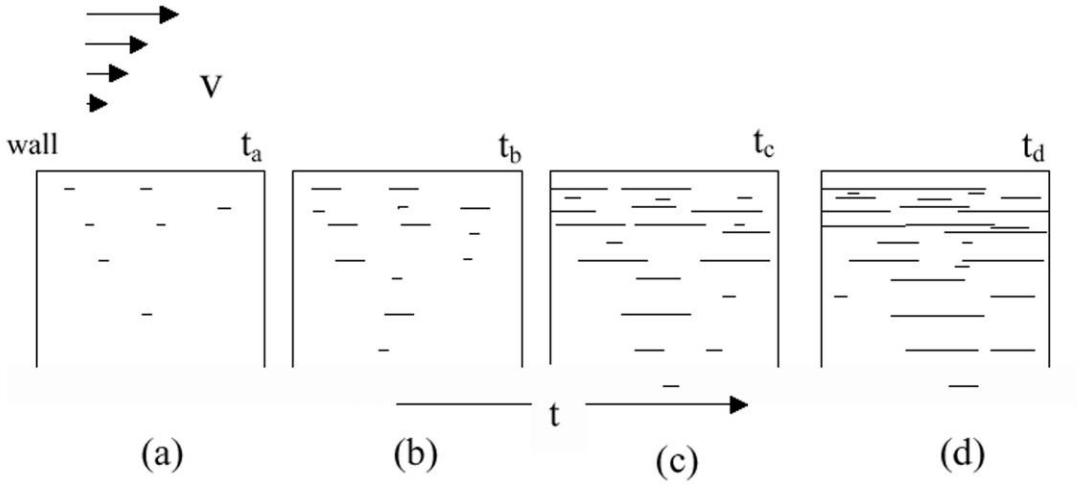

Figure 3.22: Schematic diagram of Janeschitz-Kriegl's model for the formation of the skin layer induced by applying shear above the threshold shear stress. (a) Point nuclei appear in the super cooled melt at t_a. The number density of the nuclei decreases with increasing depth from the wall. (b) Threadlike precursors grow in the flow direction from the point nuclei that appeared at t_a. The lateral growth of lamellae from threadlike precursors begins. Additional pointlike precursors form during the period from t_a to t_b. (c) As threads become long enough that lateral growth would suppress noncrystallographic branching, the template for an oriented skin is created. (d) Further increase in the number and length of threads leads to greatly increased overall crystallization rate and highly oriented growth.

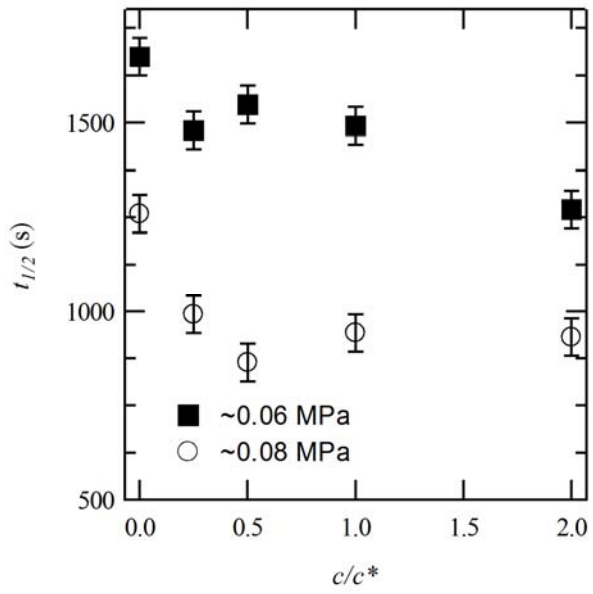

Figure 3.23: The turbidity half-time ($t_{1/2}$) to reach $I_{tot}/I_{tot}(0)$ = 0.5 vs. long chain concentration (c/c^*) for conditions where highly oriented growth did *not* occur. Actual σ_w for each point ~0.06 MPa: B0 0.062 MPa; B025 0.059 MPa; B05 0.061 MPa; B1 0.059 MPa; and B2 0.057 MPa. Actual σ_w for each point ~0.08 MPa: B0 0.074 MPa; B025 0.067 MPa; B05 0.086 MPa; B1 0.088MPa; and B2 0.085 MPa. For each case $w_{ex} \approx 100$ mg.

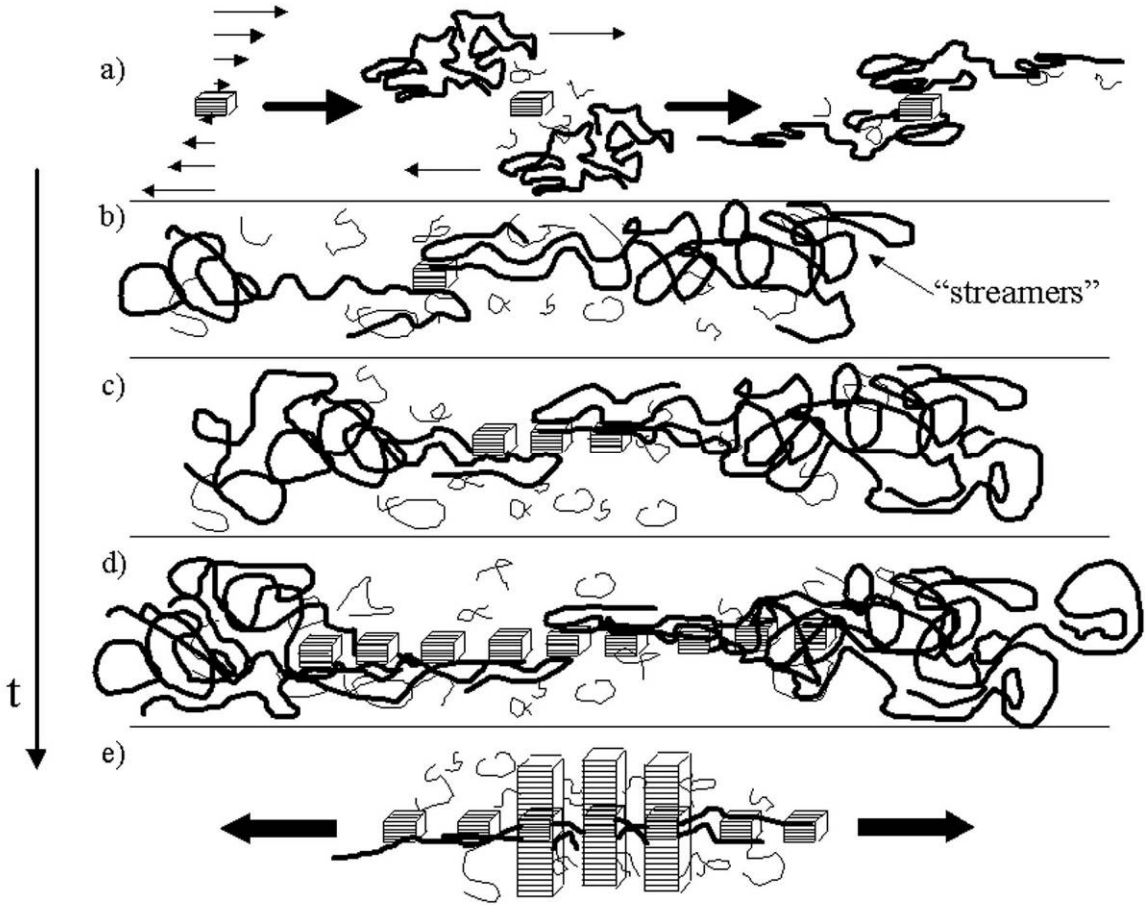

Figure 3.24: Schematic diagram of the nature of shear-induced oriented nucleation and subsequent growth of oriented crystalline lamellae during short-term shearing above the threshold shear stress. (a) A long chain (bold line) dispersed in short chains in a supercooled polymer melt adsorbs to an existing pointlike precursor as it flows past. Dangling segments of adsorbed chains become oriented due to sustained shear. (b) Additional chains adsorb and their dangling segments form "streamers" upstream and downstream of the pointlike precursor. (c) The increased local orientation of the chain segments increases the probability that long-lived ordered structures will form. (d) More chains adsorb to these new nucleation sites and the process propagates a string of nuclei along the line of flow. (e) The nuclei along this thread lead to lateral lamellar growth.

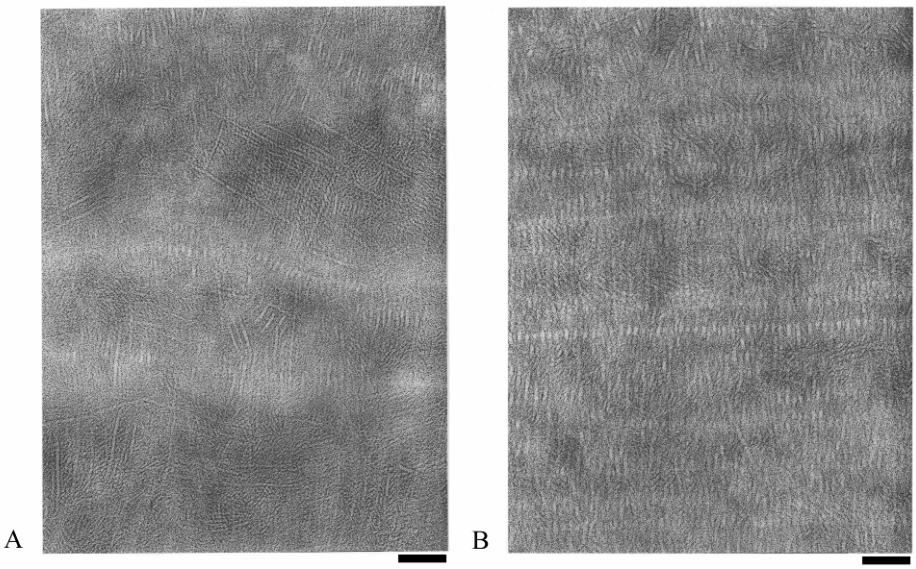

Figure 3.25: TEM micrographs of curved and straight shish in the skin layer of (A) B025 and (B) B2 crystallized at T_c = 137 °C after shearing at σ_w = 0.12 MPa for similar total strain ($w_{ex} \approx$ 100 mg), corresponding to t_s = (A) 1.0 s and (B) 0.75 s. Scale bars are 100 nm.

3.6 Bibliography

1. Hill, M.J. and A. Keller, "*Further Studies on Polyethylene Crystallized under Stress - Morphology, Calorimetry, and Stress Relaxation." Journal of Macromolecular Science-Physics*, **1971**. *B 5*: 591-&.
2. Hill, M.J. and A. Keller, "*Direct Evidence for Distinctive, Stress-Induced Nucleus Crystals in Crystallization of Oriented Polymer Melts." Journal of Macromolecular Science-Physics*, **1969**. *B 3*: 153-&.
3. Pennings, A.J. and A.M. Kiel, "*Fractionation of Polymers by Crystallization from Solution .3. On Morphology of Fibrillar Polyethylene Crystals Grown in Solution." Kolloid-Zeitschrift and Zeitschrift Fur Polymere*, **1965**. *205*: 160-&.
4. Fritzsch, A.K. and F.P. Price, "*Crystallization of Polyethylene Oxide under Shear." Polymer Engineering and Science*, **1974**. *14*: 401-12.
5. Keller, A. and H.W.H. Kolnaar, *Flow-Induced Orientation and Structure Formation*, in *Processing of Polymers*, H.E.H. Meijer, Editor. 1997, Wiley-VCH: New York. p. 189-268.
6. Somani, R.H.; B.S. Hsiao; A. Nogales; S. Srinivas; A.H. Tsou; I. Sics; F.J. Balta-Calleja, and T.A. Ezquerra, "*Structure development during shear flow-induced crystallization of i-PP: In-situ small-angle X-ray scattering study." Macromolecules*, **2000**. *33*: 9385-94.
7. Jerschow, P. and H. JaneschitzKriegl, "*The role of long molecules and nucleating agents in shear induced crystallization of isotactic polypropylenes." International Polymer Processing*, **1997**. *12*: 72-77.
8. Sherwood, C.H.; F.P. Price, and R.S. Stein, "*Effect of Shear on Crystallization Kinetics of Poly(Ethylene Oxide) and Poly(Epsilon-Caprolactone) Melts." Journal of Polymer Science Part C-Polymer Symposium*, **1977**: 77-94.
9. Lagasse, R.R. and B. Maxwell, "*Experimental-Study of Kinetics of Polymer Crystallization During Shear-Flow." Polymer Engineering and Science*, **1976**. *16*: 189-99.
10. Vleeshouwers, S. and H.E.H. Meijer, "*A rheological study of shear induced crystallization." Rheologica Acta*, **1996**. *35*: 391-99.
11. Duplay, C.; B. Monasse; J.M. Haudin, and J.L. Costa, "*Shear-induced crystallization of polypropylene: Influence of molecular weight." Journal of Materials Science*, **2000**. *35*: 6093-103.
12. Elmoumni, A.; R.A. Gonzalez-Ruiz; E.B. Coughlin, and H.H. Winter, "*Isotactic poly(propylene) crystallization: Role of small fractions of high or low molecular weight polymer." Macromolecular Chemistry and Physics*, **2005**. *206*: 125-34.
13. Paukkeri, R. and A. Lehtinen, "*Fractionation of Polypropylenes Using Soxhlet Extraction Methods." Polymer*, **1994**. *35*: 1673-79.
14. Lehtinen, A. and R. Paukkeri, "*Fractionation of Polypropylene According to Molecular-Weight and Tacticity." Macromolecular Chemistry and Physics*, **1994**. *195*: 1539-56.
15. Liedauer, S.; G. Eder, and H. Janeschitzkriegl, "*On the Limitations of Shear-Induced Crystallization in Polypropylene Melts." International Polymer Processing*, **1995**. *10*: 243-50.

16. Andersen, P.G. and S.H. Carr, "*Crystal Nucleation in Sheared Polymer Melts." Polymer Engineering and Science*, **1978**. *18*: 215-21.
17. Wolkowicz, M.D., "*Nucleation and Crystal-Growth in Sheared Poly(1-Butene) Melts." Journal of Polymer Science Part C-Polymer Symposium*, **1977**: 365-82.
18. Kumaraswamy, G.; J.A. Kornfield; F.J. Yeh, and B.S. Hsiao, "*Shear-enhanced crystallization in isotactic polypropylene. 3. Evidence for a kinetic pathway to nucleation." Macromolecules*, **2002**. *35*: 1762-69.
19. Eder, G. and H. Janeschitz-Kriegl, *Crystallization*, in *Processing of Polymers*, H.E.H. Meijer, Editor. 1997, Wiley-VCH: New York. p. 269-342.
20. Eder, G.; H. Janeschitzkriegl, and S. Liedauer, "*Crystallization Processes in Quiescent and Moving Polymer Melts under Heat-Transfer Conditions." Progress in Polymer Science*, **1990**. *15*: 629-714.
21. Janeschitz-Kriegl, H. and G. Eder, "*Basic Concepts of Structure Formation During Processing of Thermoplastic Materials." Journal of Macromolecular Science-Chemistry*, **1990**. *A27*: 1733-56.
22. Mitsubishi Chemical Company
23. Dow Chemical Company
24. Kusano, Y.M., T., *Polymer Prepr., Jpn.*, **1996**. *45*: 3278.
25. Seki, M.; H. Nakano; S. Yamauchi; J. Suzuki, and Y. Matsushita, "*Miscibility of isotactic polypropylene/ethylene-propylene random copolymer binary blends." Macromolecules*, **1999**. *32*: 3227-34.
26. de Gennes, P.G., *Scaling Concepts in Polymer Physics*. 1979, Ithaca, N.Y.: Cornell University Press.
27. Takahashi, Y.; Y. Isono; I. Noda, and M. Nagasawa, "*Zero-Shear Viscosity of Linear Polymer-Solutions over a Wide- Range of Concentration." Macromolecules*, **1985**. *18*: 1002-08.
28. Ballard, D.G.H.; P. Cheshire; G.W. Longman, and J. Schelten, "*Small-Angle Neutron-Scattering Studies of Isotropic Polypropylene." Polymer*, **1978**. *19*: 379-85.
29. The effect of annealing time of the freshly filled flow cell was determined by altering the annealing time while holding crystallization conditions constant. The crystallization kinetics and orientation measured by turbidity and birefringence for samples held more than 5 min at 215 C were identical within experimental error.
30. located at Brookhaven National Laboratory in Upton, NY
31. MarUSA, Inc.
32. Ruland, W., "*X-Ray Determination of Crystallinity and Diffuse Disorder Scattering." Acta Crystallographica*, **1961**. *14*: 1180-&.
33. Dean, D.M.; L. Rebenfeld; R.A. Register, and B.S. Hsiao, "*Matrix molecular orientation in fiber-reinforced polypropylene composites." Journal of Materials Science*, **1998**. *33*: 4797-812.
34. Sano, H.; T. Usami, and H. Nakagawa, "*Lamellar Morphologies of Melt-Crystallized Polyethylene, Isotactic Polypropylene and Ethylene - Propylene Copolymers by the Ruo4 Staining Technique." Polymer*, **1986**. *27*: 1497-504.

35. Kumaraswamy, G.; A.M. Issaian, and J.A. Kornfield, "*Shear-enhanced crystallization in isotactic polypropylene. 1. Correspondence between in situ rheo-optics and ex situ structure determination." Macromolecules*, **1999**. *32*: 7537-47.
36. Kumaraswamy, G.; R.K. Verma; A.M. Issaian; P. Wang; J.A. Kornfield; F. Yeh; B.S. Hsiao, and R.H. Olley, "*Shear-enhanced crystallization in isotactic polypropylene Part 2. Analysis of the formation of the oriented "skin"." Polymer*, **2000**. *41*: 8931-40.
37. Alamo, R.G.; M.H. Kim; M.J. Galante; J.R. Isasi, and L. Mandelkern, "*Structural and kinetic factors governing the formation of the gamma polymorph of isotactic polypropylene." Macromolecules*, **1999**. *32*: 4050-64.
38. Lotz, B.; J.C. Wittmann, and A.J. Lovinger, "*Structure and morphology of poly(propylenes): A molecular analysis." Polymer*, **1996**. *37*: 4979-92.
39. Kornfield, J.A.; G. Kumaraswamy, and A.M. Issaian, "*Recent advances in understanding flow effects on polymer crystallization." Industrial & Engineering Chemistry Research*, **2002**. *41*: 6383-92.
40. Nogales, A.; B.S. Hsiao; R.H. Somani; S. Srinivas; A.H. Tsou; F.J. Balta-Calleja, and T.A. Ezquerra, "*Shear-induced crystallization of isotactic polypropylene with different molecular weight distributions: in situ small- and wide-angle X-ray scattering studies." Polymer*, **2001**. *42*: 5247-56.
41. Janeschitz-Kriegl, H.; E. Ratajski, and H. Wippel, "*The physics of athermal nuclei in polymer crystallization." Colloid and Polymer Science*, **1999**. *277*: 217-26.
42. Lotz, B. and J.C. Wittmann, "*The Molecular-Origin of Lamellar Branching in the Alpha-(Monoclinic) Form of Isotactic Polypropylene." Journal of Polymer Science Part B-Polymer Physics*, **1986**. *24*: 1541-58.
43. Jamieson, A.M.; D.F. Gu; F.L. Chen, and S. Smith, "*Viscoelastic behavior of nematic monodomains containing liquid crystal polymers." Progress in Polymer Science*, **1996**. *21*: 981-1033.
44. Pope, D.P. and A. Keller, "*Study of Chain Extending Effect of Elongational Flow in Polymer-Solutions." Colloid and Polymer Science*, **1978**. *256*: 751-56.
45. Smith, D.E.; H.P. Babcock, and S. Chu, "*Single-polymer dynamics in steady shear flow." Science*, **1999**. *283*: 1724-27.

4 EFFECT OF LONG CHAIN MOLECULAR WEIGHT IN BIDISPERSE BLENDS

4.1 Introduction

The high molecular weight tail in the distribution of molecular weights has been shown to strongly influence the development of oriented crystalline morphologies in flow-induced crystallization (Chapter 3). The effectiveness of these long chains in promoting nucleation under flow derives from the spectrum of relaxation times existing within a broad distribution of molecular weights. For linear chains, the longest molecules have the slowest relaxation dynamics. According to the theory of reptation originally postulated by de Gennes,[1] the relaxation time (τ) of a linear polymer chain scales with chain length (N) as $\tau_{rep} \sim N^3$. The reptation model does not strictly account for the dynamics of an entangled melt,[2] and theories that include constraint release and contour length fluctuations[3,4] give better accord with experimentally observed scaling of the terminal relaxation time ($\tau \sim N^{3.4}$). This molecular weight scaling results in a large disparity in relaxation times between

the average chain and the longest chains and can lead to preferential orientation of the longest chains under sufficiently strong flow conditions.

In 2002 Kumaraswamy reported evidence of a kinetic pathway to oriented nucleation in flow-induced crystallization.[5] The time required to observe the onset of oriented crystallization, manifested as an "upturn" in birefringence during shearing, *decreased* with increasing temperature. Furthermore, the decrease in time matched the rheological time-temperature superposition shift factor, a_T, suggesting that the formation of the oriented precursors tracks the molecular dynamics of the melt. This behavior was unanticipated in models describing crystallization. The role of long chains in the schematic model given in Chapter 3 is compatible with a kinetic pathway: both the time required to sweep long chains over the surface of an existing precursor and the time for the adsorbed long chains to become distorted follow the time-temperature shift behavior of the melt. More recent models[6-8] have begun to incorporate the state of molecular orientation of the longest chains to represent more realistically the underlying physics responsible for flow-induced nucleation. Experimental determination of the effect the length of the long chains on the formation of oriented precursors is needed to test these models.

Having established a relationship between the concentration of long chains in the melt and the formation of threadlike precursors to oriented growth, we aim to determine what constitutes "long chains" in comparison to the weight averaged molecular weight of the short bulk chains, M_S, using well-defined, bidisperse blends of isotactic polypropylene in which the weight averaged molecular weight of the long chain component, M_L, is varied. We anticipate a lower bound in M_L/M_S below which the long chains do not access sufficiently strong orientation compared to the bulk chains and exert no influence on the formation of oriented crystalline morphologies.

4.2 Experimental

4.2.1 Materials

The same "base resin" was used to prepare a series of bimodal blends with a small concentration of long chains added. The base resin (Base-PP) is the same as in Chapter 3,

with moderate molecular weight (186 kg/mol) and narrow polydispersity in terms of both molecular weight (M_w/M_n = 2.3) and stereoregularity ([mmmm] = 96%) provided by Dr. Robert Sammler (Dow Chemical Company). Four high molecular weight iPPs with lengths from 507 kg/mol to 3500 kg/mol were used (Table 4.1). The first three were fractions provided by Mitsubishi Chemical Company: f507-PP (M_w = 507 kg/mol, M_w/M_n = 1.2, [mmmm] = 98%), f862-PP (M_w = 862 kg/mol, M_w/M_n = 1.3, [mmmm] = 98%), and f923-PP (M_w = 923 kg/mol, M_w/M_n = 1.3, [mmmm] = 98%), prepared by fractionation from a parent iPP polymerized with a Ziegler-Natta catalyst as described in Chapter 3. The fourth, 3500-PP, is an ultra-high molecular weight iPP (~3500 kg/mol, M_w/M_n = 1.8) and high stereoregularity ([mmmm] > 98%) prepared by metallocene polymerization.

Bidisperse blends, prepared via the solvent blending procedure described in Chapter 3 (3.2.1), are referenced according to the M_w of the long chains, *e.g.*, B507 denotes the blend of f507-PP with Base-PP. From Equation 3.1 we estimated the overlap concentration, c^*, for long chain materials (Table 4.1). Guided by our earlier findings that $c/c^* = 1$ is sufficiently concentrated to observe a strong influence of long chains on flow-induced crystallization, we formulated blends such that the long chain concentration $c = c^*$ for f507-PP, f862-PP and f923-PP (1.66 wt%, 0.84 wt%, and 0.7 wt%). The blend of 3500-PP contained 1 wt% ($c/c^* = 2.4$) of long chains. Due to the unusually high molecular weight of 3500-PP, even this low concentration caused the solution viscosity to be noticeably higher during solution blending and required a longer time to obtain a homogeneous mixture. Using the extrusion rates (w_{ex}/t_s) of the blends at a stress low enough that crystallization does not affect the rate of extrusion, we estimate the ratio of the viscosity of the blends to the viscosity of the base polymer to be ~ 1.28:1 (B500) – 1.32:1 (B3500).

4.2.2 *In situ* rheo-optical measurements

The experimental conditions applied in this study were similar to those in Chapter 3. To erase any memory effects caused by the channel filling process, the flow cell was initially held at 215 °C for 10 min. All experiments described here were conducted at the same T_c of 137 °C (maintained within ± 0.3 °C). Short-term shear pulses corresponding to wall shear stresses (σ_w) of 0.07 and 0.11 MPa were applied for brief periods such that t_s was much less

than the crystallization time at this temperature. The maximum t_s was determined to be that at which ≈ 100 mg of supercooled polymer was extruded. To make comparisons at constant applied stress and constant total strain, small changes in t_s were chosen to hold the amount of polymer extruded (w_{ex}) for each blend approximately fixed.

The orientation of crystalline microstructure is determined by the development of birefringence in the sample. When the optical retardance is less than a half-wave ($\lambda/2$), the birefringence can be calculated from the ratio of the perpendicular component of transmitted light between crossed-polarizers to the total intensity ($I_{\perp}/I_{tot}$) according to Equation 2.1. The time at which the retardance reaches a half-wave is marked by a maximum in $I_{\perp}/I_{tot}$ and a full-wave is marked by a minimum. Successive minima correspond to increasing, odd multiples of $\lambda/2$ and successive maxima correspond to even multiples of $\lambda/2$. We only consider extrema for determining birefringence when the total transmittance is greater than 20%. However, spectrographic birefringence studies of liquid crystalline polymers by Burghardt and coworkers[9] showed that using extrema to calculate birefringence is robust even in the presence of depolarization.

4.2.3 *In situ* rheo-WAXD

A selected set of shearing conditions was further examined by rheo-WAXD (wide angle X-ray diffraction) to provide detailed information concerning crystallization kinetics and the crystallite orientation distribution. Specifically, we analyze the 2-D X-ray diffraction patterns as described in Chapter 3 to extract the following metrics: crystallinity index (x_c), and the attributes of Lorentzian fits to the azimuthal distribution of intensity at 110 and 040 reflections (peak height, FWHM, and position).

4.2.4 Optical microscopy (OM)

Thick sections (thickness = 5 μm) were taken in the flow-vorticity and flow-gradient planes and examined using a polarized-light microscope to evaluate the presence and thickness of the oriented skin and fine-grained layers induced by flow.

4.2.5 DSC measurements

The quiescent crystallization and the melting of iPPs were characterized using a differential scanning calorimeter (Perkin-Elmer DSC-7) at a scanning rate of 5 °C/min in a N_2 atmosphere.

4.2.6 Measurement of molecular weight

Weight averaged molecular weight (M_w) and polydispersity of molar mass for f507-PP, f862-PP, f923-PP, and Base-PP were measured using GPC with an on-line multi-angle laser light scattering photometer (GPC-MALLS) and differential refractometer by collaborators at Mitsubishi Chemical Company. The measurements were performed on a Waters model 150C with three polystyrene columns (SHODEX KF-806M from Showa Denko Company, Ltd.) at 413.2K using a flow rate of 1.0 mL/min. The sample was injected as a 0.3 mL aliquot of a 1,2,4-trichlorobenzene solution with 2 mg/mL concentration. The differential refractometer was used to detect solute concentration from the specific refractive index increment. Scattered light was measured simultaneously at 17 angles ranging from 18° to 155° using a DAWN DSP from Wyatt Technology Corp., equipped with a He-Ne laser (λ = 632.8 nm). The ASTRA software package from Wyatt was used for analyzing GPC data and scattering data (details[10] are published elsewhere).

4.3 Results

4.3.1 Quiescent crystallization kinetics

Crystallization in the absence of flow reveals no discernible trend in kinetics with increasing long chain molecular weight (Figure 4.1). The differences in overall crystallization kinetics suggest a variation in foreign particles which can act as heterogeneous nucleants and dominate the rate of nucleation under quiescent conditions. With application of flow, the influence of incidental foreign particulates is small compared to the flow-induced nucleation (compare Figure 4.1 and Figure 4.2A).

4.3.2 *In situ* rheo-optical

We examine the effects of long chain molecular weight (M_L) at two shearing conditions: using a wall shear stress σ_w = 0.11 MPa and σ_w = 0.07 MPa. The former is above the

threshold stress σ^* to induce the transition to oriented growth in bimodal blends with long chain $M_L \geq 862$ kg/mol[5,11] and is below the base resin's σ^* (Chapter 3). In contrast, $\sigma_w = 0.07$ MPa is less than σ^* of the binary blends we have examined previously. After cessation of shearing at $\sigma_w = 0.11$ MPa, the birefringence increases with time only for bimodal blends containing long chains of $M_L \geq 862$ kg/mol. This signature of the creation of oriented precursors during flow is absent if the long chains are ~500 kg/mol. The growth of birefringence after shearing is stronger the longer the "long chains" (Figure 4.2A). For the longest two, B923 and B3500, an upturn in birefringence is evident during shear. The timescale of crystallization as gauged by the turbidity of the sample is also unchanged by addition of long chains with $M_L \sim 500$ kg/mol and only mildly changed by addition of long chains with $M_L \sim 862 - 923$ kg/mol (Figure 4.2B). The dramatic increase in flow-induced orientation in B3500 is accompanied by a tremendous acceleration (two orders of magnitude) in crystallization kinetics. Crystalline microstructure that scatters light develops so fast that the total transmitted intensity drops below one-half prior to the end of shearing. Note that the cylinder actuation caused a jump in the position of the flow cell that partially obscures the incident laser beam; withdrawal of the cylinder repositions the cell to its initial placement. This displacement leads to an artificially lowered $I_{tot}/I_{tot}(0)$ value during the pulse. The total intensity should remain constant at 100% up to approximately $t = 1$ s for B3500 [Figure 4.2B]; thereafter the intensity should be understood to fall monotonically with the final value during the pulse equal to that immediately after the pulse.

To further illustrate the tendency of ultra-high molecular weight polymer chains to induce oriented crystallization, we examine a weak shearing condition in which the applied stress is lower than the threshold stress for any of the blends described in the previous chapter ($\sigma^*(c) \geq 0.099$ MPa, Figure 3.8). For $\sigma_w = 0.07$ MPa, only B3500 develops an upturn in birefringence during shearing and an increase of birefringence following cessation of flow (Figure 4.3A), clearly indicating a strong dependence of σ^* on M_L. Following mild shearing, crystallization is slightly slower overall compared to intense shearing and the crystallization kinetics increase mildly with M_L (Figure 4.3B).

4.3.3 *In situ* rheo-WAXD

Time-resolved rheo-WAXD of the bimodal blends following intense shearing (B862 and B923 at σ_w = 0.11 MPa and B3500 at σ_w = 0.065 MPa) shows the degree of crystallinity reaches greater values on faster timescales with increasing M_L. No synchrotron time was spent on B507 in view of the optical results showing it was indistinguishable from Base-PP. Despite imposing a wall shear stress approximately half as intense, the resulting crystallinity for B3500 is nearly double that of B862 and B923 (Figure 4.4). Furthermore, B3500 has a tighter distribution of orientations (FWHM) and a larger population of oriented crystallites (110 parent area) as evident in azimuthal scans of the 110 crystalline reflection (Figure 4.5). The ratio of parent to daughter crystallites is greater for blends containing long chains than it is for Base-PP; however, the enhancement is independent of M_L. An increase in the P:D ratio with M_L might become evident if B3500 is subject to the same shear stress, since the parent to daughter ratio increases with applied shear stress, Chapter 5.

4.3.3 *Ex situ* optical microscopy

Examination of the final crystalline morphology by polarized light microscopy readily reveals the enhancement by long chains with $M_L \geq 862$ kg/mol (Figure 4.6). The boundary between the birefringent skin layer near the wall and the spherulitic core defines the threshold stress (σ^*) necessary to induce highly oriented crystallization. The value of σ^* depends on M_L and shows a strong drop between 923 and 3500 kg/mol (Figure 4.7).

4.4 Discussion

4.4.1 Importance of relaxation-time separation on shish-kebab formation

We have previously established that the formation of threadlike precursors depends heavily on the presence of long polymer chains with slow relaxation dynamics compared to the average. The preferential orientation of the longest chains leads to long-lived anisotropic structures that template further oriented growth. The extent of this preferential orientation is controlled by the melt dynamics of the molecules, specifically the separation in relaxation time scales between the longest chains and the average in the blend. This separation of

relaxation times depends on the relative chain lengths and on the concentration of the long chains. Here both species are well entangled: M_S/M_e = 43 and M_L/M_e ranges from 112 to 800, using M_e = 4400 kg/mol[12] (although the entanglement molecular weight of iPP is still disputed). The relaxation time of the short chains is not affected significantly by the addition of a small concentration of long chains: their reptation timescale, $\tau_{rep,S} \sim (N_S/N_e)^{3.4}$, is independent of c and M_L. The situation is more complex for the long chains.

The long chains are at the concentration threshold for overlap, too low a concentration for them to entangle with each other. The motion of the short chains permits much, or even all, of the distortion of the long chains to relax on timescales much shorter than the reptation time of the long chains, $\tau_{rep,L} \sim (N_L/N_e)^{3.4}$, where N_e is the length of chain per entanglement blob and N_L is the length of a long chain. In this regime of dominant constraint release, there appears to be a threshold ratio of chain lengths $(M_L/M_S)^*$ somewhere between M_L/M_S = 2.5 (too low) and 4.4 (above threshold) required to perceptibly change flow-induced crystallization behavior from that of Base-PP. It is more difficult to specify the corresponding ratio of the relaxation times (τ_L/τ_S), which would enable comparison with theoretical models of flow-induced crystallization and has implications regarding the mechanism of the long chain effect.

Theoretical models of the rheology of binary blends have been developed that estimate the terminal relaxation time of the long chains according to the molecular weights and concentrations of the components.[13,14] In the present blends the short chain constraints last long enough to impose an effective "tube" constraining long chain motion, i.e., they satisfy the criterion $N_S^3/(N_L N_e^2) > 1$.[13,14] Therefore, the terminal relaxation of the long chains can be modeled using a coarse-grained adaptation of the Rouse bead-spring model in which each entanglement blob is represented by a single bead-spring unit. In the literature this mode of relaxation is termed "tube-Rouse"[14] or "hindered-Rouse."[15] Recent experiments on the dynamics of the long chains in dilute binary blends by Wang and coworkers[15] show that long chains at $c = c^*$ exhibit a Rouse-like relaxation spectrum (see Figure 7b of ref. 15). In blends having N_L/N_S from 6.6 to 25 and well-entangled short chains ($N_S/N_e \sim 10$), the increase in viscosity due to the long chains exhibited a regime of linear behavior at low

volume fraction, $\phi < \phi_c$, where ϕ_c is an empirical critical concentration. Based on their finding that ϕ_c was greater than the overlap concentration, the viscosity increase $\Delta\eta$ due to the long chains at $c = c^*$ should conform to the hindered-Rouse regime: $\Delta\eta = \phi\eta_S [N_L/(N_e N_S)^{1/2}]$, where η_S is the viscosity of the pure short chain melt and the factor in square brackets is due in part to the magnitude of the long chain contribution to the modulus, $G_P \approx \phi G_N^o (N_e N_S)^{1/2}/N_L$, and in part due to the long chain hindered-Rouse relaxation time, $\tau_{hR} \approx \tau_S N_L^2/N_e N_S$. This expression captures the fact that the viscosities of three of the blends (B507, B862, and B923) are very nearly equal, all having $\Delta\eta/\eta_S \approx 0.25$ based on their observed extrusion rates. Unfortunately, the underlying expression for τ_{hR} gives unreasonable results for these three blends: $\tau_{hR}/\tau_S \approx 300$ for B507 and $\tau_{hR}/\tau_S \approx 1000$ for B862 and B923, in which time the long chains would instead relax by reptation ($\tau_L/\tau_S \approx 30$ for B507 and $\tau_L/\tau_S \approx 200$ for B862 and B923). The case of the most interesting blend, B3500, is the most ambiguous. Based on hindered-Rouse, addition of 1% of 3500 kg/mol chains would more than double the viscosity relative to the base resin. We did not find this to be the case; instead, its extrusion rate is very similar to that of the other three blends. Future research on the linear visco-elasticity of these specific blends may shed light on this discrepancy (perhaps, the long chain contribution in B3500 is extremely shear thinning, giving $\eta_{app} \approx \eta_S$ at the shear stresses used in our experiment).

The abrupt increase in the effect of the long chains when M_L is increased from 507 to 862 kg/mol is reminiscent of the notion of a critical molecular weight (M^*) originally introduced by Keller[16] to describe the portion of chains in a distribution of molecular weights that become fully extended in an abrupt coil-stretch transition. Keller's experiments were conducted on dilute solutions of polymers in extensional flows, but he believed the same mechanism might apply to entangled systems or even weak flows (i.e., shear flow). For Keller, the presence of shish-kebab structures was an indicator of extended chains. However, in shear flow the polymer conformation is unlikely to approach its fully extended length,[17] although portions of the chain may become stretched. Therefore, we conclude that shish-kebab formation is *not* contingent on fully stretched chains. Instead, a

sufficient degree of segmental orientation, which can be achieved far below full extension, enables propagation of shish.

4.4.2 Dependence of the threshold stress on M_L

The longer the long chains are relative to the average length, the greater the level of orientation they reach at a given stress. In accord with segmental orientation being the determinant of shish propagation, the threshold stress necessary to induce oriented crystallization decreases strongly as M_L/M_S increases (Figure 4.7). All four blends have similar viscosity which is approximately 30% greater than Base-PP. Therefore, comparisons at fixed stress correspond to approximately constant deformation rate as well. The ratio of deformation rate to relaxation rate, characterized in steady shear flow by the Weissenberg number ($Wi \equiv \tau\dot{\gamma}$, the product of the relaxation time and the shear rate), governs the distortion of chain conformation during flow.[18]

Several researchers[7,19] have recently adopted the use of these dimensionless parameters to classify and model flow-induced crystallization as a function of the material relaxation ($\sim M_w$) and the strength of the flow. Van Meerveld[19] defines two Deborah numbers for shear flow: one based on the reptation time (De_{rep}) and the other based on the much shorter time scale for contour length fluctuations related to chain stretching (De_s). For $De_{rep} < 1$ and $De_s < 1$, the chains are at equilibrium, neither stretched nor oriented; for $De_s < 1 < De_{rep}$, flow induces mild orientation (disturbing conformation on length scale greater than the entangled blob size, but not orienting segments within an entanglement blob); and for $De_s > 1$, the onset of chain stretching occurs. Furthermore, van Meerveld posits that the ratio of long chain length to the average in the melt (M_L/M_S) and the concentration of long chains will influence the orientation and stretch experienced by the high molecular weight chains. Increasing M_L/M_S results in an increase in De_s and De_{rep} for the long chains when equivalent flow conditions are imposed. Therefore, long chains in the bimodal blends with greater M_L/M_S experience greater chain orientation and stretching and increase the propensity to form threadlike precursors.

Here we do not pursue a more quantitative treatment of the degree of orientation of the long chains when free in the melt or when adsorbed to propagating shish. In the following chapter we take a substantive step toward quantitative analysis by developing a new method to extract the depth dependence (hence stress dependence) of flow-induced crystallization from average measurements across the entire sample thickness (hence the entire stress range from 0 to σ_w).

Conclusions

Increasing the M_w of the long chains in a bimodal blend increased the tendency to form threadlike precursors to oriented crystallization. This was highlighted by a marked decrease in the threshold stress necessary to induce long-lived oriented precursor structures. Thus, the propagation of shish varies strongly with the separation in time scales between the slowest relaxing chains and the average. Below a threshold ratio of relaxation times ($\tau_L/\tau_S \sim$ 100) addition of long chains did not change the behavior from that of Base-PP itself.

Table 4.1 Characteristics of Base and Long iPP

sample	M_w [a] (kg/mol)	M_n [a] (kg/mol)	M_w/M_n	c^* 10^3 (g/cm^3)	[mmmm] [b] (mol%)	T_m [c] (°C)
Base-PP	186.0	80.9	2.3	15.6	96.0	148.3
f507-PP	507.5	422.9	1.2	9.4	98.3	169.7
f862-PP	862.0	663.1	1.3	7.2	98.5	170.6
f923-PP	923.2	707.3	1.3	7.0	98.0	164.6
3500-PP	3500	1950	1.8	3.6	> 98	145.4

[a]Determined by GPC-MALLS. [b] ^{13}C NMR. [c]Apparent melting temperature obtained from peak position of DSC.

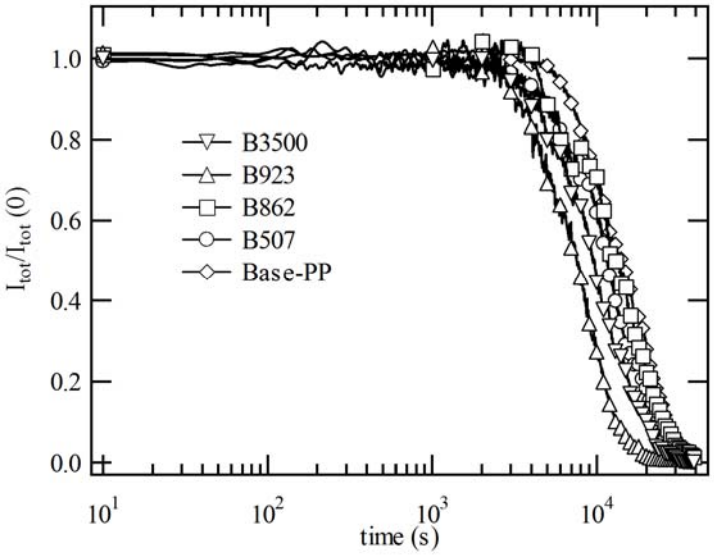

Figure 4.1: Total transmitted intensity between crossed polars of bimodal blends crystallized in the absence of flow at T_c = 137 °C. The M_w of the long chain component (M_L) is varied and denoted by the sample code.

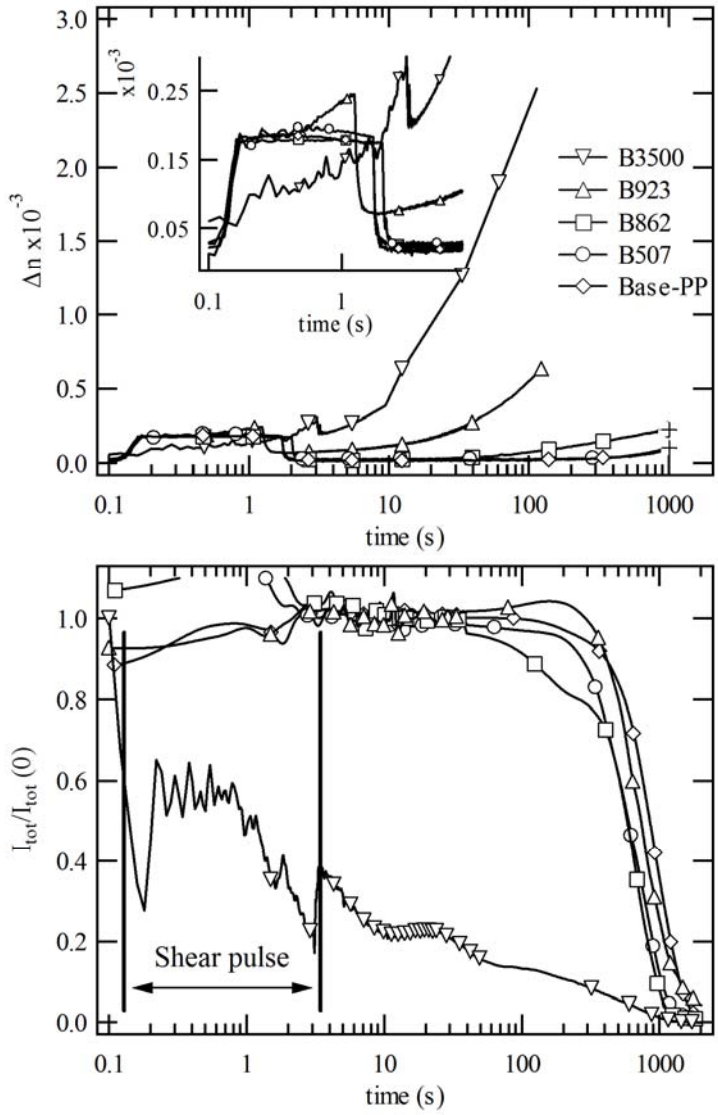

Figure 4.2: Birefringence (top) and total transmitted intensity (bottom) for bimodal blends crystallized at 137 °C after shearing at σ_w = 0.11 MPa for 1.7 s (Base-PP, B507), 2.0 s (B862), 1.25 s (B923), and 3.0 s (B3500). Inset shows birefringence during the shearing pulse. Note the timescale here is an order of magnitude shorter than that of quiescent crystallization shown in Figure 4.1. See text for explanation of large drop in $I_{tot}/I_{tot}(0)$ for B3500 during the pulse.

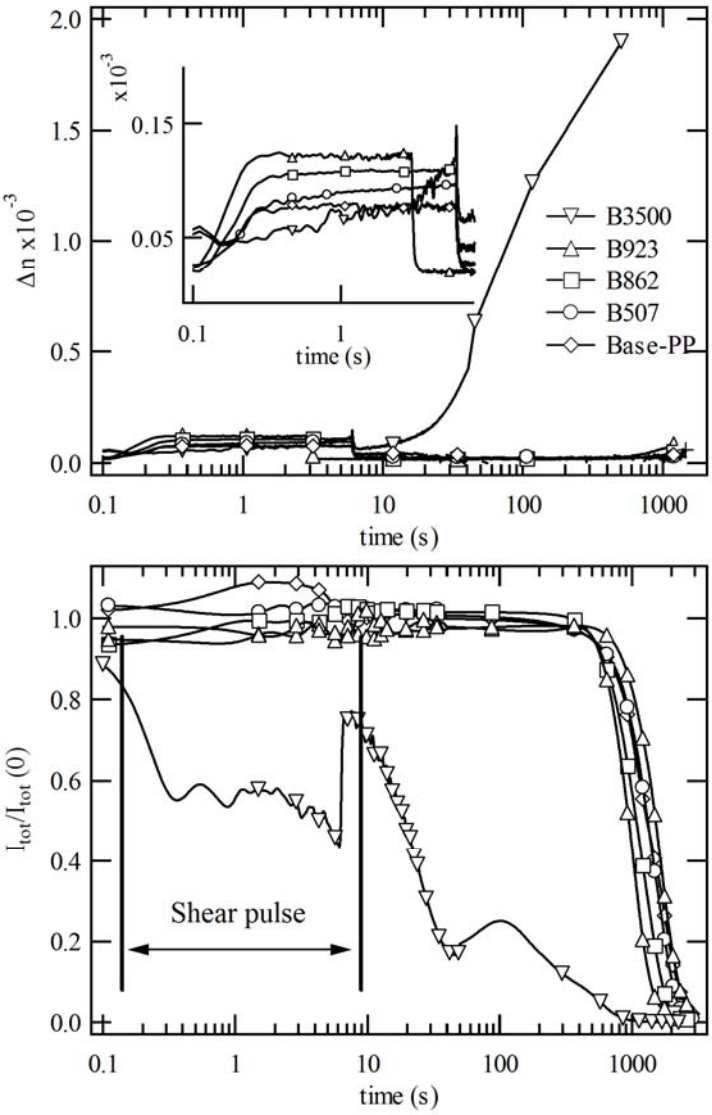

Figure 4.3: Birefringence (top) and total transmitted intensity (bottom) for bimodal blends crystallized at 137 °C after shearing at σ_w = 0.07 MPa for 6.0 s (BASE-PP, B507, B862, and B3500). B923 sheared at σ_w = 0.06 MPa for 7.5 s. Inset shows birefringence during the shearing pulse.

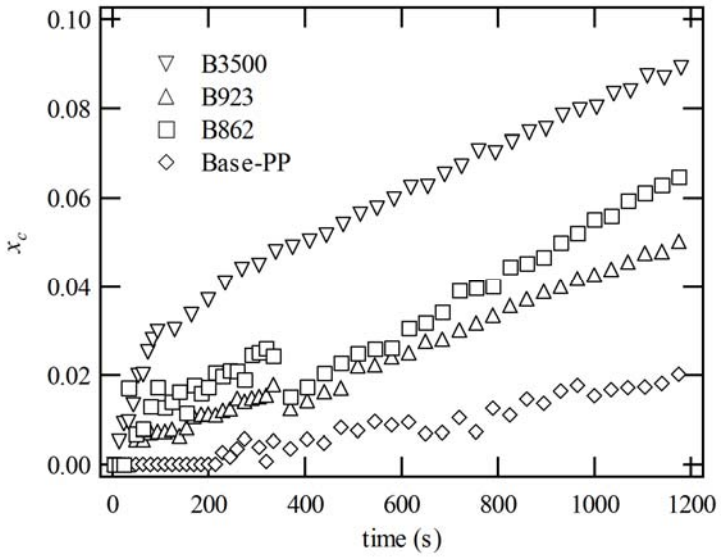

Figure 4.4: Crystallinity index for bimodal blends with increasing M_L. Breaks in the data near 300 s for B862 and B923 are an artifact upon changing data acquisition time. See Figure 4.5 caption for shearing conditions.

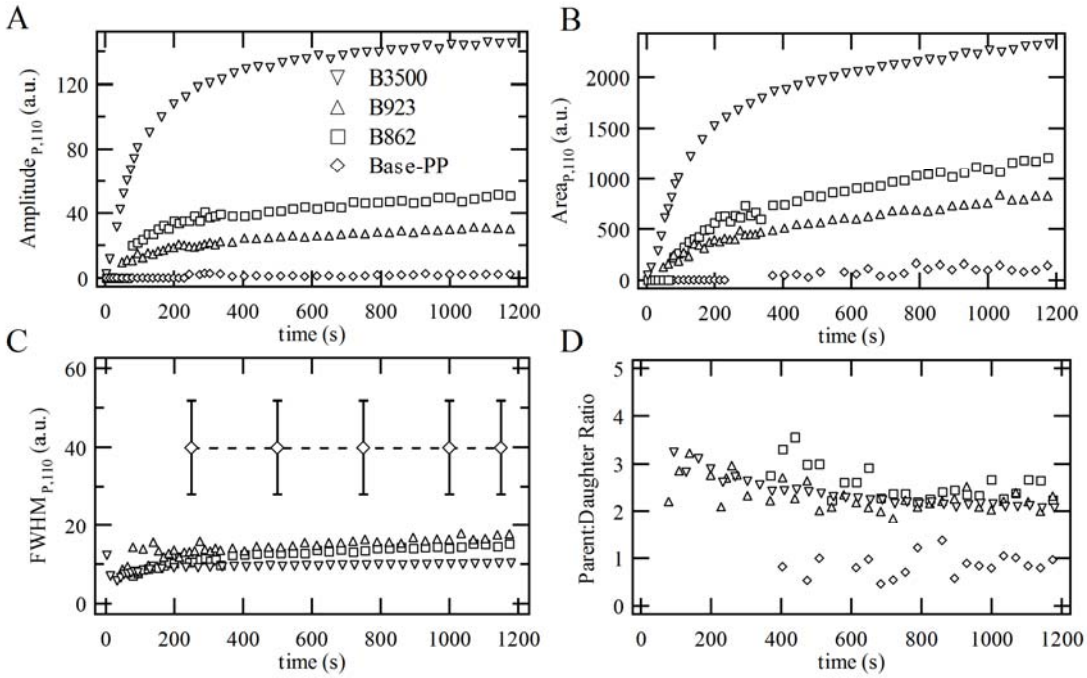

Figure 4.5: Time evolution of peak parameters for fits of parent peaks on azimuthal scans of the 110 reflection. Degree of oriented crystallite A) parent amplitude and B) parent area increased with M_L. The distribution of orientations of parent crystallites, C) FWHM, is more narrow for increasing M_L (the average FWHM for Base-PP is indicated by a dashed line with standard deviation) and D) the parent:daughter ratio was approximately the same. The results are for crystallization at 137 °C following shearing at 0.11 MPa for 1.7 s (Base-PP), 2.0 s (B862), and 2.2 s (B923). B3500 was sheared at 0.065 MPa for 7 s and is presented to demonstrate the magnitude of orientation enhancement caused by the ultra-high molecular weight chains even at mild conditions.

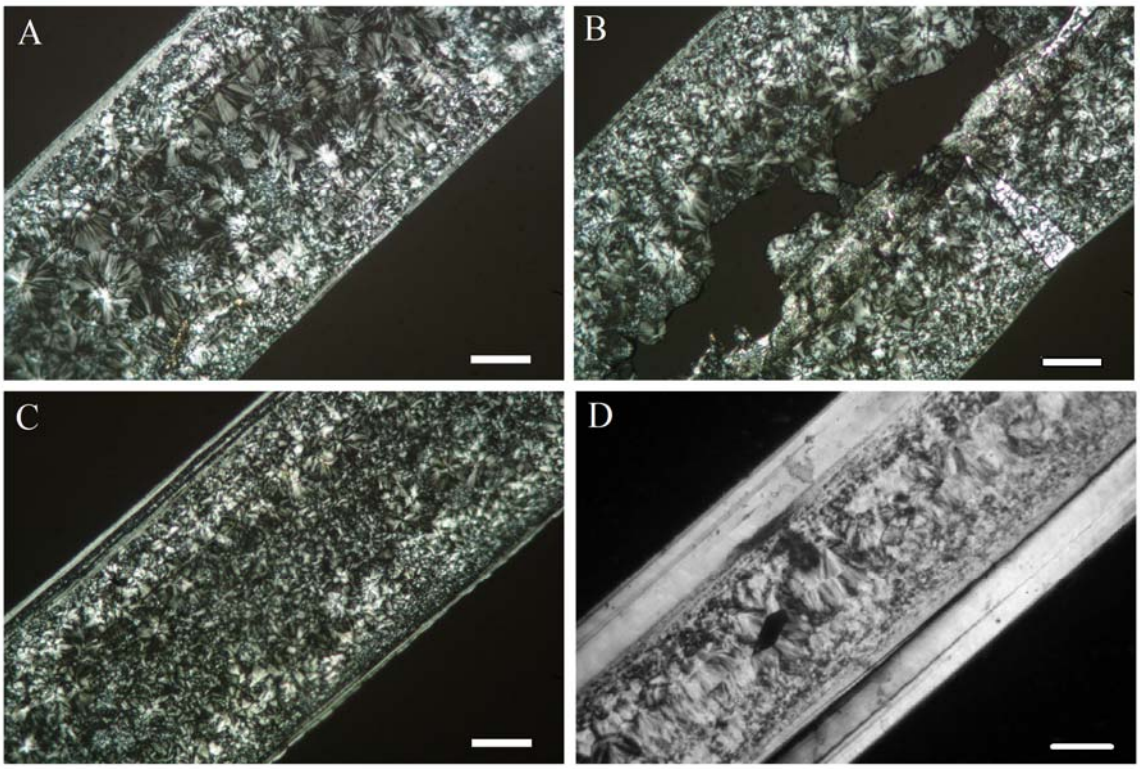

Figure 4.6: Polarized optical micrographs of A) Base-PP, B) B500, C) B923 (representative of B862 micrographs), and D) B3500 for the same conditions as Figure 4.5. Samples were crystallized isothermally at 137 °C for ~2 hrs before quenching. The void in the center of B) B500 is due to rupture caused by contraction of the sample volume as it crystallized. Scale bar is 100 μm.

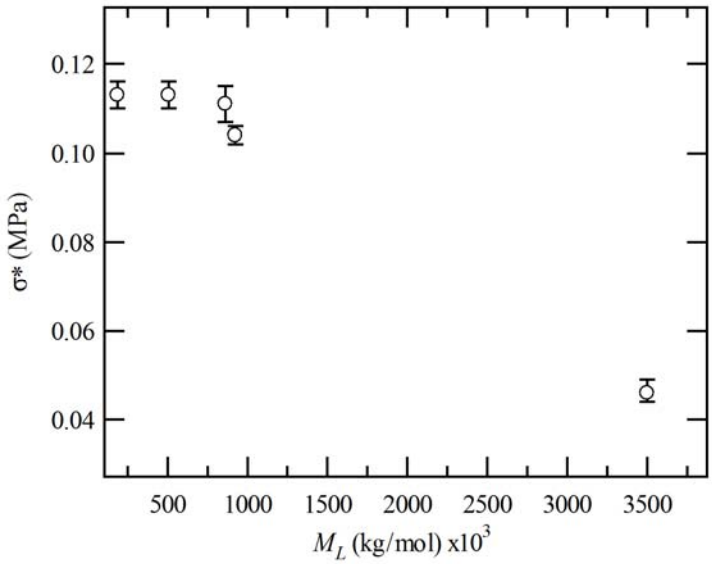

Figure 4.7: Threshold stress for transition to oriented morphology. Error bars represent variation in skin thickness in the micrographs used for determination of the skin-core boundary.

4.6 Bibliography

1. de Gennes, P.G., *Scaling Concepts in Polymer Physics*. 1979, Ithaca, N.Y.: Cornell University Press.
2. Doi, M. and S.F. Edwards, *The Theory of Polymer Dynamics*. 1986, New York: Oxford University Press.
3. Milner, S.T. and T.C.B. McLeish, "*Parameter-free theory for stress relaxation in star polymer melts." Macromolecules*, **1997**. *30*: 2159-66.
4. Milner, S.T.; T.C.B. McLeish; R.N. Young; A. Hakiki, and J.M. Johnson, "*Dynamic dilution, constraint-release, and star-linear blends." Macromolecules*, **1998**. *31*: 9345-53.
5. Kumaraswamy, G.; J.A. Kornfield; F.J. Yeh, and B.S. Hsiao, "*Shear-enhanced crystallization in isotactic polypropylene. 3. Evidence for a kinetic pathway to nucleation." Macromolecules*, **2002**. *35*: 1762-69.
6. Acierno, S.; S. Coppola; N. Grizzuti, and P.L. Maffettone, "*Coupling between kinetics and rheological parameters in the flow-induced crystallization of thermoplastic polymers." Macromolecular Symposia*, **2002**. *185*: 233-41.
7. Coppola, S.; N. Grizzuti, and P.L. Maffettone, "*Microrheological modeling of flow-induced crystallization." Macromolecules*, **2001**. *34*: 5030-36.
8. Zuidema, H.; G.W.M. Peters, and H.E.H. Meijer, "*Development and validation of a recoverable strain-based model for flow-induced crystallization of polymers." Macromolecular Theory and Simulations*, **2001**. *10*: 447-60.
9. Hongladarom, K. and W.R. Burghardt, "*Molecular Alignment of Polymer Liquid-Crystals in Shear Flows .2. Transient Flow Behavior in Poly(Benzyl Glutamate) Solutions." Macromolecules*, **1993**. *26*: 785-94.
10. Seki, M.; H. Nakano; S. Yamauchi; J. Suzuki, and Y. Matsushita, "*Miscibility of isotactic polypropylene/ethylene-propylene random copolymer binary blends." Macromolecules*, **1999**. *32*: 3227-34.
11. Seki, M.; D.W. Thurman; J.P. Oberhauser, and J.A. Kornfield, "*Shear-mediated crystallization of isotactic polypropylene: The role of long chain-long chain overlap." Macromolecules*, **2002**. *35*: 2583-94.
12. van Meerveld, J., "*A method to extract the monomer friction coefficient from the linear viscoelastic behavior of linear, entangled polymer melts." Rheologica Acta*, **2004**. *43*: 615-23.
13. Frischknecht, A.L. and S.T. Milner, "*Linear rheology of binary melts from a phenomenological tube model of entangled polymers." Journal of Rheology*, **2002**. *46*: 671-84.
14. Viovy, J.L.; M. Rubinstein, and R.H. Colby, "*Constraint Release in Polymer Melts - Tube Reorganization Versus Tube Dilation." Macromolecules*, **1991**. *24*: 3587-96.
15. Wang, S.F.; Y. Elkasabi, and S.Q. Wang, "*Rheological study of chain dynamics in dilute binary polymer mixtures." Macromolecules*, **2005**. *38*: 125-33.
16. Keller, A. and H.W.H. Kolnaar, *Flow-Induced Orientation and Structure Formation*, in *Processing of Polymers*, H.E.H. Meijer, Editor. 1997, Wiley-VCH: New York. p. 189-268.

17. Babcock, H.P.; R.E. Teixeira; J.S. Hur; E.S.G. Shaqfeh, and S. Chu, "*Visualization of molecular fluctuations near the critical point of the coil-stretch transition in polymer elongation." Macromolecules*, **2003**. *36*: 4544-48.
18. Larson, R.G., *The Structure and Rheology of Complex Fluids*. Topics in Chemical Engineering, ed. K.E. Gubbins. 1999, New York: Oxford University Press. 663.
19. van Meerveld, J.; G.W.M. Peters, and M. Hutter, "*Towards a rheological classification of flow induced crystallization experiments of polymer melts." Rheologica Acta*, **2004**. *44*: 119-34.

5 TOWARD THE DETERMINATION OF PROPAGATION VELOCITY OF THREADLIKE PRECURSORS USING REAL-TIME "DEPTH SECTIONING"

5.1 Introduction

A fundamental goal in studying flow-induced crystallization is the development of a predictive model that can determine final material properties and relies only on polymer molecular characteristics and flow conditions. A successful model should capture not only the kinetics of crystallization but also the crystalline morphology, since material properties are strongly influenced by the anisotropy of crystallites. A number of empirical models[1-4] have been formulated over the years which rely on comparison to experiments to set their adjustable parameters. These models fail to consider the importance of morphology on the determination of crystallization kinetics, degree of crystallinity, or crystallite orientation. The phenomenological model of Eder[5,6] does account for morphology and predicts the structure of crystallization (number of shish, shish length) but relies only on flow kinematics (a power law dependence on flow rate) rather than the dynamics of the

molecules. An appreciation for the role of molecular dynamics has prompted the development of a micro-rheological model that aims to predict crystallization induction time on a molecular basis with knowledge of a few nonadjustable parameters.[7, 8] While this model successfully predicts crystallization induction times and even predicts the relative increase in flow-induced nucleation with increasing temperature,[9] as reported in our group,[10] it fails to incorporate the anisotropy of nucleation and final crystalline morphology. The model currently being developed by Meijer and co-workers[11] holds the most promise in predicting crystalline structure and kinetics based on the dynamics of molecules deformed by flow and can successfully predict the layer transitions in the skin-core morphology. The model modifies Eder's equations, replacing the shear rate dependence with a material state parameter (recoverable strain) based on the configuration state of the molecules.

Predictive models rely on validation from experimental data to ensure that the model is based on the correct physical mechanisms. Currently, experimental knowledge of the relationships between flow conditions and threadlike precursor formation is limited. Understanding the highly nonlinear effects of stress on formation of anisotropic nuclei is a key to predicting crystallite morphology and final material properties. It is generally accepted that the longest (slowest relaxing) chains are important to formation of threads due to preferential orientation in flow, and the effect is nonlinear with stress. However, much of the experimental effort is focused on determining the nature of the precursor structure, which remains highly debated. The precursors are described as extended chain crystals,[12,13] liquid-crystalline smectic bundles,[14-16] and non-crystalline microfibrils.[17] Here we hope to shed light on the inception and propagation of threadlike nuclei from a sheared melt. We present rheo-optics and rheo-WAXD to characterize the inception and growth of shish as a function of flow conditions. To do so, we also present a novel analysis of macroscopic measurements (such as WAXD, birefringence, dichroism, or light scattering) to infer the depth-dependence of the emerging microstructure during and after flow.

5.2 Experimental

5.2.1 Materials

We further examine the bidisperse blend of 3500-PP (1 wt%) and Base-PP, referred to as B3500. The preparation and molecular details of this blend are described in Chapter 4 (see Section 4.2.1 and Table 4.1).

5.2.2 *In situ* rheo-optical measurements

All rheo-optical experiments described here for B3500 were performed at T_c = 137 °C using the same experimental protocols reported earlier in Chapter 4. The flow cell was initially held at 215 °C for 10 min after filling with polymer melt from the reservoir. The sample was cooled to the crystallization temperature (T_c) and a pressure drop was applied to drive shear flow through the channel for a brief shearing time t_s. Short-term shear pulses with a fixed wall shear stress (σ_w) of 0.06 MPa were applied for brief periods such that t_s (varied from 1 – 12 s) was much less than the quiescent crystallization time at this temperature. The turbidity and birefringence were tracked to monitor the progress and anisotropy of crystallization.

5.2.3 *In situ* rheo-WAXD

An expanded set of shearing conditions were further examined by rheo-WAXD (wide angle X-ray diffraction) to provide more detailed information concerning crystallization kinetics and the distribution of crystallite orientations. In addition to the conditions delineated for rheo-optical experiments, a series of shear stresses (σ_w = 0.037, 0.045, 0.055, and 0.062 MPa) were applied for t_s = 7 and 12 s at T_c = 137 °C.

5.2.4 Real-time “depth sectioning”

In a pressure-driven flow through a rectangular slit, the shear stress imposed on a fluid is highest near the walls of the channel. The stress varies linearly from the wall to the center of the channel where no distortion of the fluid occurs and stress is zero. This robust relationship between distance from the center and stress enables meaningful analysis of the stress dependence of morphological features that appear in solidified samples. Earlier (Chapter 3), we deduced a threshold stress value for the transition from unoriented to

oriented crystallization by *ex situ* microscopic examination of quenched samples (for a given sample). This value was further validated by dynamic experiments at mild conditions ($\sigma_w < \sigma^*$) that showed no evidence of oriented crystallization, consistent with the inferred threshold stress.

Fortunately, the stress-depth relationship also enables meaningful analysis of the depth dependence of real-time data. Using thoughtfully selected sets of shearing conditions (constant t_s with varied σ_w), we can isolate the signal arising from a given depth at each time point using rheo-optical and rheo-WAXD methods. The key feature is examining the incremental contribution to the real-time data from one shear stress to another (with all other conditions fixed), allowing us to attribute the difference to a small spatial region of the sample (Figure 5.1). For example, consider a pair of experiments performed on the same material (B3500) at the same temperature (137 °C) for the same shearing time (12 s) but for two different values of the wall shear stress ($\sigma_{w,1}$ = 0.064 MPa and $\sigma_{w,2}$ = 0.055 MPa). At every moment in time (e.g., 130 s) during and after shear, the depth averaged measurement obtained for the experiment with $\sigma_{w,2}$ = 0.055 MPa corresponds to the depth average signal from the central 86% ($\sigma_{w,2}/\sigma_{w,1}$) of the sample subjected to $\sigma_{w,1}$ = 0.064 MPa, simply rescaled for optical path length. If we subtract the X-ray diffraction pattern captured at 130 s after shearing at $\sigma_{w,2}$ = 0.055 MPa from the X-ray diffraction pattern captured at 130 s after shearing at $\sigma_{w,1}$ = 0.064 MPa, the remaining diffraction pattern can be attributed to the outermost 35 μm of the 500 μm thick sample subjected to $\sigma_{w,1}$ = 0.064 MPa, i.e., where the applied stress was between 0.064 and 0.055 MPa (Figure 5.2). Repeating this procedure with progressively lower wall shear stress yields a depth-dependent profile of X-ray patterns of the sample subjected to $\sigma_{w,1}$ = 0.064 MPa. For comparison with one another, the resultant patterns are normalized based upon the thickness of the region each represents.

5.3 Results

5.3.1 *In situ* rheo-optical

5.3.1.1 Turbidity

The evolution of turbidity following shear treatment occurred faster with increasing shearing time (Figure 5.3). The increasing turbidity as the crystallites grow causes the total transmitted intensity to decay to zero typically with a sigmoidal time profile when viewed against a logarithmic timescale. However, for conditions that induce very strong crystallite orientation, the transmittance decays in two stages. For example, when B3500 is sheared at $\sigma_w = 0.06$ for $t_s > 4$ s, an early decay profile is followed by a second drop in transmittance. Interestingly, the second decay coincides with the timescale of the decay for shearing at 1s $< t_s \leq 4$ s. (Only the shortest shearing time, $t_s = 1$ s, gave a timescale of turbidity development significantly slower than the rest).

5.3.1.2 Birefringence

Following cessation of shear, birefringence developed earlier and reached a higher ultimate value with increasing shearing time at constant stress (Figure 5.4). During the shearing pulse, the birefringence rises quickly to a steady value. For $t_s > 4$ s, the birefringence shows the "upturn" feature associated with oriented crystallites and does not fall back to zero after cessation of shear. For $t_s \leq 4$, no "upturn" occurs and the birefringence drops back to zero following shearing as the stress is relaxed. It is worth noting that the time required for relaxation of the birefringence to zero after the cessation of shear is longer than the observed time in previous blends of Base-PP with long chains of $M_w < 10^6$ g/mol. This is a consequence of the extremely high molecular weight of 3500-PP. For conditions where the birefringence fully relaxed after shear ($t_s < 4$), it takes ~1.6 s for the birefringence to return to the baseline value after cessation of shear. (For comparison, blends from Chapter 3 composed of Base-PP and 923 kg/mol L-PP required only ~250 ms for birefringence relaxation).

After cessation of shearing (for $t_s > 3$ s) and a short delay (1 – 10 s), birefringence from growing, oriented crystallites develops. For $t_s = 2$ and 3 s, the birefringence is low and

develops after a long delay (100 s) but grows while the transmittance is still above 50%, indicating it is not an artifact of depolarization. Negligible birefringence is detected for the condition where t_s = 1 s. The intensity transmitted through crossed polarizers, $I_{\perp}/I_{tot}$, does not rise significantly above the baseline until the total transmittance falls below 50% accompanied by depolarization of the incident light.

5.3.2 *In situ* rheo-WAXD

From inspection of 2-D WAXD patterns, the qualitative trends are evident. The degree of crystallinity, degree of orientation, and ratio of parent- to daughter-crystallites increases with shearing duration (Figure 5.5 and 5.6). A well-defined, fiberlike orientation of α-iPP crystallites with c-axis in the flow direction develops for $t_s > 2$ s. For $t_s \leq 10$ s, no crystalline peaks are detected during the shear pulse, indicating that all measurable crystallization occurs in the absence of flow. For t_s = 12 s, the first detectable crystalline reflections occur in the frame which captures the last 2 s of shearing (5 s acquisition times are used during the first minute with approximately 5 s between frames for CCD readout). The crystallinity index, x_c, is 0.019 for this frame, about 17% the crystallinity at the time of impingement (130 s) for this condition.

The sensitivity of birefringence allows detection of smaller amounts of oriented crystallites than WAXD measurements. However, birefringence tends to underestimate orientation in the presence of a low parent to daughter crystallite ratio, which can mask the orientation of parents when the nearly orthogonal daughters cancel out birefringence of the parents. This is evident in our WAXD data for short shearing times. Despite the similarly low birefringence measured using rheo-optics for the shortest shearing times (Figure 5.4), the population of uniaxially oriented crystallites is noticeably greater for t_s = 3 s than for 2 s at σ_w = 0.06 MPa (Figure 5.6). Furthermore, it is clear from WAXD that t_s = 1 s is insufficient to induce orientation, confirming that the rise in $I_{\perp}/I_{tot}$ at long time is due to depolarization of the light that occurs at low transmittance.

These trends in morphology are evident in the time-dependence of the 2-D WAXD. A striking increase in the rate of crystallization with t_s is readily observable between t_s = 3 s

and 4 s where x_c becomes measurable earlier and grows faster (Figure 5.7A). At early times, the crystallinity is attributable to oriented crystallites only: the initial increase in x_c correlates with an increase in amplitude of the parent peaks in an azimuthal scan of the 110 reflection (Figure 5.7B) and a tighter distribution of orientations (FWHM) of the parents (Figure 5.7C). The FWHM of parent peaks saturates to nearly the same value for $t_s > 4$ s, but is significantly broader for shorter shearing times.

Azimuthal scans of the 110 diffraction indicate that two populations of highly oriented crystallites develop and that the relative intensity of the parent and daughter peaks (P:D ratio) increases with increasing shearing time for $t_s > 4$ s (Figure 5.8). The P:D ratio is nearly identical for $t_s = 3$ s and 4 s. Peak fits for $t_s = 2$ s were too unreliable to calculate a P:D ratio with confidence, and shorter shearing duration induced no orientation.

The parent peak area grows more rapidly with increasing shearing time. For longer shearing times ($t_s > 4$ s), a sharp rise is followed by a change in growth rate (Figure 5.9A). The change in growth rate can be attributed to the impingement of kebabs growing outward from adjacent shish. The impingement time decreases for increasing shear duration but saturates above $t_s > 5$ s: 200 s for $t_s = 4$ s; 65 s for $t_s = 5$ s; and 55 s for $t_s > 5$ s. Prior to impingement, the growth of parent 110 peak is roughly linear with time.

Comparison of the slopes of this linear region of growth against shearing time enables us to evaluate the relative growth front induced by flow. The growth rate of the 110 parent peak area increases gradually with t_s up to 4 s, then strongly with further increase in t_s (Figure 5.9B).

5.3.3 Real-time “depth sectioning”

Using the analysis method described above to assign depth dependence to real-time data, we analyze four depth sections (Figure 5.10 top): the sections represent depths from the wall between 0 – 35 μm, 35 – 74 μm, 74 – 102 μm, and 102 - 250 μm (the channel center). Each of these differential WAXD patterns (Figure 5.10 middle) is normalized by the thickness of the corresponding section and analyzed to compute x_c,and the amplitude and FWHM of parent 110 peak.

According to the "depth sectioning" analysis for a sample sheared for 12 s at 0.064 MPa, the rapid rise of 110 parent peak area, $Area_{P,110}$, occurs within 74 μm of the channel wall, predominantly in the outermost 35 μm (Figure 5.11A). At depths between 74 and 102 μm, $Area_{P,110}$ rises more slowly but plateaus at the same value as the 35 -74 μm section. The outermost section reaches a greater $Area_{P,110}$, suggesting more densely packed crystallites. The onset of impingement, characterized using the time of the maximum rate of increase of $Area_{P,110}$, occurs earlier in sections closer to the wall (25 s for 0 – 35 μm; 55 s for 35 – 74 μm; and 85 s for 74 – 102 μm). With increasing distance from the wall, the orientation distribution of the parent crystallites distinctly broadens and the parent-to-daughter ratio decreases (Figure 5.11B and 5.11C). Peaks in the "core" section are weak, leading to a large uncertainty in the parameters of the Lorentzian fit. We present data for the central section only to indicate that the orientation distribution is much broader than in the sections nearer to the channel walls.

Identical analysis of a series of shearing conditions for t_s = 7 s provides a glimpse of the depth-dependent effects of shearing time (Figure 5.12). Within 35 μm of the wall, the growth of $Area_{P,110}$ with time following 7 s of shear is very similar to that after 12 s of shear, including the impingement time (35 s for t_s = 7 s; 25 s for t_s = 12 s). Based on our prior work, this suggests that the length of shish per unit volume created during the first 7 s of shear hardly changed during continued shearing for 5 s more: the nucleation enhancement in the outermost 35 μm saturates within 7 s of shear at $\sigma = 0.060 \pm 0.005$ MPa. Deeper than 35 μm into the sample, decreasing t_s from 12 s to 7 s resulted in much slower growth of $Area_{P,110}$, a lower final value of $Area_{P,110}$, and a longer time before impingement (Figure 5.12A). Likewise, at depths greater than 35 μm, the FWHM shows a monotonic broadening with increasing depth and broader values for 7 s compared to 12 s of shearing (Figure 5.12B). The P:D ratio at each depth for t_s = 7 s was lower than at the equivalent depth for t_s = 12 s. The depth dependence of P:D that was seen for t_s = 12 s is absent for t_s = 7 s (Figure 5.12C).

From the depth dependent results, it is clear that the initial growth rate of $Area_{P,110}$, $[dArea/dt]_0$ is a highly nonlinear function of stress (Figure 5.13).

5.4 Discussion

Recent rheo-optical and rheo-WAXD experiments have provided rich information regarding the development of anisotropic crystalline morphology during and after flow.[18-24] However, the nature of pressure driven flow through a channel combined with orientation of the optical axis along the velocity gradient direction restricted real-time measurements to averaged quantities over the depth of the flow channel. Study of depth dependent effects have been performed "post mortem" following quench and removal of the sample. The "depth sectioning" analysis employed here enables us to extract depth dependent information in a time-resolved fashion.

5.4.1 Propagation of threadlike precursors

Our interpretation of the present results is strongly influenced by the conclusions of earlier work[20, 25] in which we combined *ex situ* electron microscopy with *in situ* optical and X-ray measurements. The material was a conventional Ziegler-Natta iPP (ZN-iPP) that behaved at 141 °C in a manner analogous to the B3500 in the following respects: at stresses above a threshold value (~0.047 MPa for ZN-iPP, ~0.044 MPa for B3500), it is possible to induce the transition to oriented growth if shearing is sustained for a long enough time (≥ 2 s for ZN-iPP, ≥ 3 s for B3500); the transition to oriented growth is marked by formation of oriented crystals after flow has ceased. Images of the nanostructure in ZN-iPP showed that increasing shearing time led to the following sequence of morphologies in the region where $\sigma^* < \sigma < \sigma_w$: for t_s = 1 s, sparse needle-like precursors templating growth of oblong spherulites; for t_s = 2 s, row-nucleated structures with threadlike precursors many micrometers in length; for t_s = 4 s, a decreased average distance between the rows in the oriented skin; t_s = 8 s, indistinguishable from t_s = 4 s. Thus, there was an initial 1 s induction period during which pointlike precursors formed and some started to elongate into needles. Over a time interval of 1 s during shear (from 1 s to 2 s), threads formed prolifically; we infer that the threads elongate by propagation upstream and downstream (by symmetry) and that their propagation velocity is of order 10 μm/s. The increase in length of shish per unit volume ceases by 4 s into the shear pulse. Thereafter, flow enhancement of crystallization that is evident in birefringence and WAXD results must

occur predominantly by lateral thickening of the threadlike precursors without significant change in their length. The fully saturated array of shish had row spacings that varied with depth in the sample, increasing from ~250 nm apart at a distance of approximately 10 μm from the wall to ~750 nm apart at a depth of 50 μm from the wall. How the depth-dependent structure formed in real-time was unknown, inspiring the design of the present experiments.

In qualitative accord with our prior findings, the real-time data here shows that threads grow longer and denser with increasing shearing time. For the series of shearing times t_s = 1, 2, 4, 5, and 7 s (Figure 5.5), almost all of the observed crystallization occurred after cessation of shearing by growth at the quiescent growth velocity. The quiescent growth rate is the same for each condition since the material composition and crystallization temperature remain unchanged. Therefore, the increase in the initial rate of oriented crystallite growth seen with increasing t_s reveals a greater total available surface area for growth templated during flow. During flow, the nucleating surface available on threadlike precursors increases by a combination of increasing thread length and increasing thread diameter. The impingement time manifested by the decrease in the rate of growth of the parents provides an indirect estimate of the distance between shish: (impingement time)*(growth velocity) ~ (distance the growth front advanced). The impingement time changes little with further increase in t_s beyond 5 s. From this we infer that increase in thread length was the dominant effect for $t_s \leq 5$ s and that thickening of the threads was dominant for $t_s > 5$ s.

5.4.2 A depth dependent sequence of events

Based on our previous schematic model (Chapter 3), we add a depth dependent facet to our sequence of events leading to the development of the shish-kebab morphology induced by shear flow. At early times, the orientation of chain segments induces the formation of stable pointlike precursors which lead to primary nucleation events from the melt. The pointlike nuclei form first nearest the wall where the stress is highest and the orientation of chain segments is greatest. As flow continues, long chains that are participating in (and anchored to) the incipient nuclei become much more distorted than the surrounding chains leading to

the growth of an anisotropic precursor structure. This occurs first near the wall where stress is highest (greatest orientation) and pointlike precursors first formed. Continued flow causes the threadlike precursors to grow in length and perhaps diameter as surrounding chains are recruited to participate and stabilize the structure. At longer flow times, pointlike precursors continue forming at depths farther from the channel wall and threadlike structures also propagate from these points. Prolonged flow acts to lengthen the existing threads, leading to a more dense thread spacing. Stable threadlike precursors nucleate crystallite growth in the form of oriented kebabs that grow radially away from this central structure. There is some evidence that the linear growth velocity of crystallites is greater during flow than in the quiescent condition;[20] however, in the current study we can not confirm this since detectable crystallization occurs after cessation of flow.

For B3500, a sufficient length per unit volume of these threadlike structures has developed to become detectable, as an upturn in birefringence, after 4 s of shearing time (Figure 5.4). However, the development of anisotropic crystalline orientation detected by WAXD at later times indicates that oriented precursor structures developed after as little as 2 s of shearing. The impingement of kebabs from neighboring shish begins at 25 s in the outermost 35 μm, causing a slow down in the growth of oriented crystalline diffraction seen in WAXD (Figure 5.9). Impingement times at greater depth from the wall are longer, implying that the distance between threads increases with depth. Thus the real-time data accords with the distribution of thread spacing seen in prior TEM studies in ZN-iPP under similar crystallization conditions[18] and in bimodal blends of narrow distribution polypropylenes (Chapter 3), although the depth dependence was mild in the blends with ~1000 kg/mol long chains.

We interpret our results in terms of shish formation during flow. Petermann and co-workers[26] have recently shown evidence of shish propagating into an undeformed melt for an isotactic polystyrene. They describe the extension of shish into the melt as an “autocatalytic” process involving ordering ahead of the growing shish as polymer chains are “reeled in” to the crystal. However, they state that the phenomenon required a material with a low crystallization rate and that resisted refolding to form chain-folded lamellae

(i.e., unpublished experiments in more common semicrystalline polymers that form chain-folded lamellae did not show shish-propagation after cessation of deformation). They concluded that the phenomenon occurs only in a relatively narrow range of systems (to date only in a low tacticity polystyrene). Highly isotactic polypropylene has a high crystallization rate and strong tendency to form chain-folded lamellar crystals; therefore, it is unlikely that iPP shish propagate after cessation of flow. Furthermore, Petermann reports shish extension of < 1 μm, which is negligible relative to the length of the shish-kebab structures seen in our TEM images (> 20 μm).

Flow suppresses the formation of daughter crystallites. Depth sectioning shows that in the outer 35 μm section the parent crystallite peak area grows at the same rate (with impingement occurring within a span of seconds) and reaches nearly the same value for a sample subject to 7 s or 12 s of flow. However, the parent to daughter ratio is about twice as high for the 12 s flow condition (Figure 5.8 and 5.13). Flow tends to direct the chain axis into the velocity direction and so tends to frustrate the growth of daughter crystals in which the polymer chain axis is nearly perpendicular to the flow direction. This finding is consistent with results reported previously by our laboratory.[20]

5.4.3 Toward determination of thread propagation velocity

The propagation of threadlike structures appears to saturate once a certain thread density is achieved. The small change in impingement time in the outer 35 μm section when comparing 7 s and 12 s shearing times suggests negligible increase in the thread *length/vol* near the wall after 7 s of shearing. The arrest of further thread propagation may be a consequence of collisions with kebab overgrowth. Since we see crystalline scattering in the first WAXD frame following 7 s of shearing and an upturn in birefringence that does not decay to zero, it is reasonable to deduce that kebabs have begun to grow prior to the end of 7 s of shearing even though they are below the sensitivity of WAXD (insensitive to < 1% crystallite volume).[27] So, any determination of thread propagation velocity should be based on conditions where shearing ceased prior to saturation

For t_s < 5 s, the initial slope $[dArea_{P,110}/dt]_0$ increases linearly with shearing time (Figure 5.9B), suggesting that thread length increases approximately linearly with time during shear at the stress level in the outermost 35 μm (σ = 0.064 - 0.055 MPa). Further, the subsequent delay (> 90 s) in the onset of detectable crystallization following short shearing times lends assurance that kebab growth did not progress significantly during flow. Therefore, these conditions are promising for estimating the thread propagation velocity. However, translating the real-time data into a linear propagation velocity for shish awaits future *ex situ* images of the final morphology for at least one shearing time.

Without real-space images, the best we can do is use the impingement time as a "ruler": the roll-off in the rate of growth of parent crystallites for the saturated structure is in the range 100 – 200 s, which would correspond to a separation between shish in the range 350 – 700 nm based on our prior work, and the quiescent growth velocity. If we took 400 nm as an estimate of the shish separation in the saturated case, we would infer that the length of shish per unit volume is roughly 4 μm^{-2}. Based on Figure 5.9B, this population of shish developed between 1 and 4 s at a roughly linear rate of 1.3 $\mu m^{-2}s^{-1}$. Again, the lack of TEM images limits our ability to translate this into a growth velocity. To illustrate how the calculation would be performed, suppose shish in the fully saturated state were observed to be 20 μm long; the real time results would suggest that the first second of shear created approximately 0.2 sites/μm^3 from which shish propagated at a velocity, v_{prop}, of roughly 7 μm/s. This example illustrates how real time measurements for a series of t_s and for a series of σ_w could be used with just a small amount of (expensive and time consuming) electron microscopy to determine the propagation velocity of shish. This method can be used to provide theorists with the first determinations of $v_{prop}(\sigma,T,$ *ultimately* as a function of molecular parameters (e.g., length, stereoregularity and concentration of long chains).

5.5 Conclusion

Our analysis of real-time rheo-optical and rheo-WAXD experiments combined with depth dependent information from "depth sectioning" confirms several existing results and uncovers several new keys to understanding how anisotropic crystalline is induced by flow.

As seen previously, threads first form near the channel wall where stress is highest and grow in length with prolonged flow. After sufficient time, thread length per unit volume saturates, perhaps due to collisions with other threads or crystalline overgrowth from those threads. The propagation of threads varies in a nonlinear manner with stress. With our current findings, we can now see that prior to saturation, when crystalline overgrowth is negligible, the thread propagation is linear with shearing time. Here we identified a promising set of conditions that can be used to measure the thread propagation velocity for this material if the appropriate length scale can be assigned by microscopy. This result moves us closer toward a previously unavailable experimental measurement of a fundamental mechanistic aspect of flow-induced crystallization necessary for modeling improvements. Future experiments might aim to deduce the effects of other conditions (temperature, molecular weight distribution, etc.) on the thread propagation velocity.

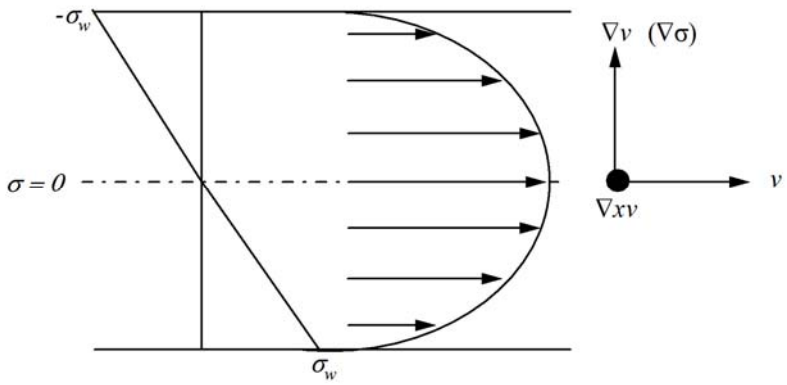

Figure 5.1: Schematic of stress profile in channel flow and a qualitative velocity profile. At the channel wall, the fluid velocity is zero (assuming the no-slip condition) due to high frictional forces resulting in a maximum stress at wall. The stress gradient is linear between the center of the channel (σ = 0) and the wall (σ_w). This linear relationship allows correlation between morphological features viewed *ex situ* and stress. Likewise, the depth dependence of real-time data can be inferred from a series of stress conditions.

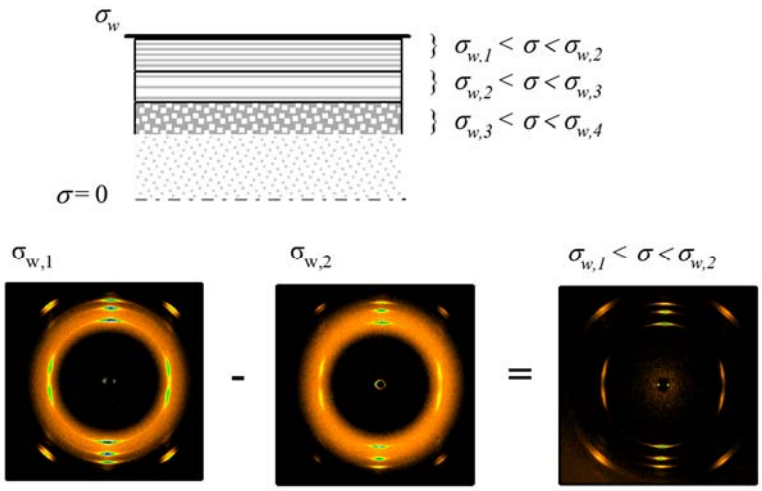

Figure 5.2: Schematic of depth sectioning profile. Examination of the difference in scattering, A, between specimen #1 and #2 enables a real-time look at crystallinity developing in a small region below the wall. A series of such specimens allows further partitioning of real-time results into depth related slices (i.e., segments B, C, and D). The specimens shown above were sheared for 12 s at 137 °C but at different stress levels: specimen #2 (σ_w = 0.064 MPa) and specimen #1 (σ_w = 0.055 MPa). WAXD patterns captured 130 s after imposition of shearing.

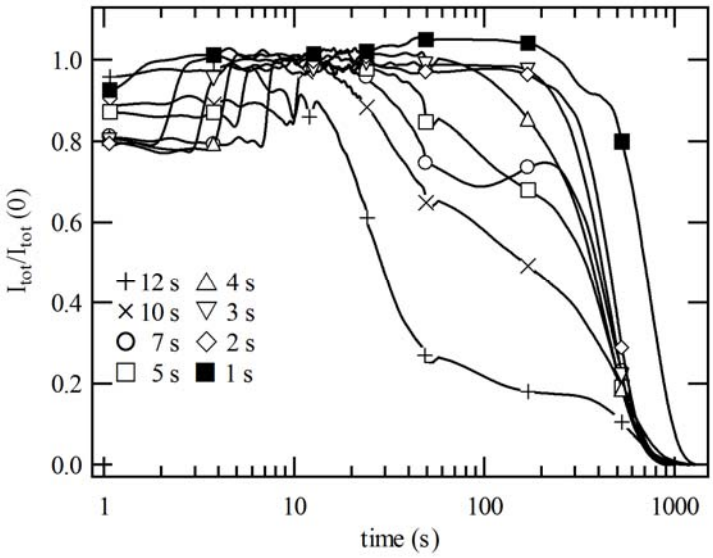

Figure 5.3: Total transmitted intensity, $I_{tot}/I_{tot}(0)$, vs. time for B3500. All samples crystallized at 137 °C following shear at σ_w = 0.06 MPa and t_s varied from 1 - 12 s.

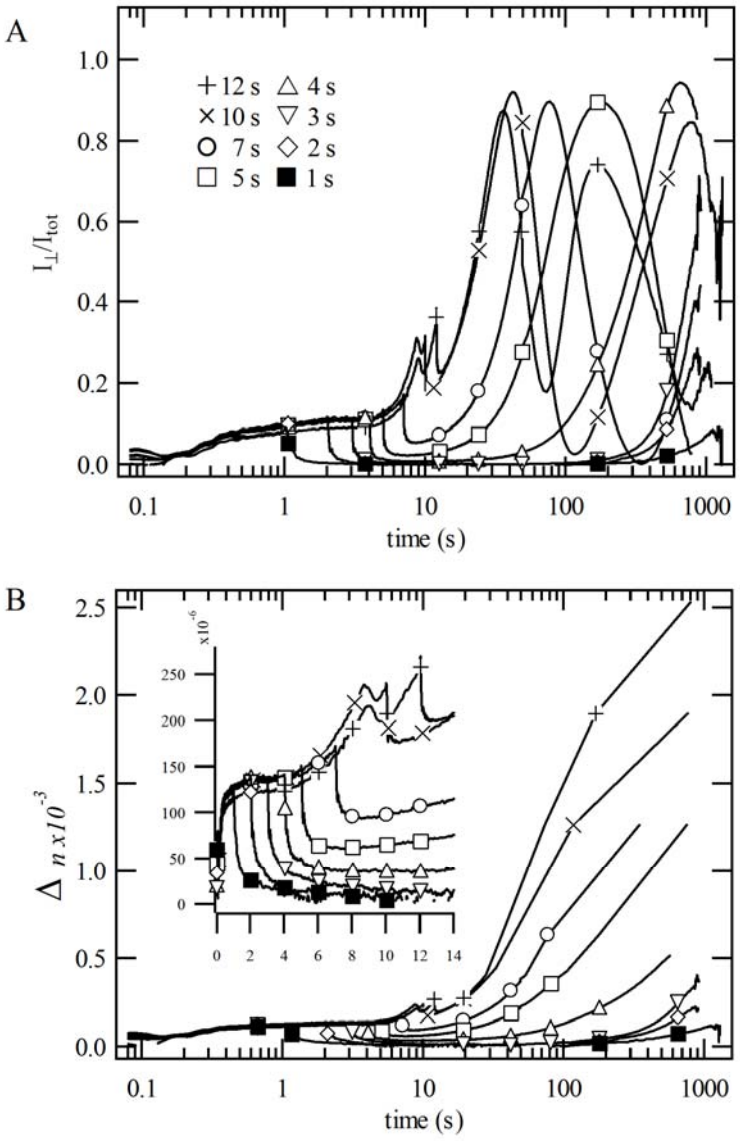

Figure 5.4: Birefringence of B3500 during crystallization at 137 °C following shearing (σ_w = 0.06 MPa) for various shearing times (t_s = 1 – 12 s) noted in the legend. A) The normalized intensity of light transmitted between crossed polarizers, $I_{\perp}/I_{tot}$, vs. time. B) The average birefringence Δn ($n_{33} - n_{11}$) vs. time calculated from $I_{\perp}/I_{tot}$ to emphasize the differences in final birefringence of the samples vs. shearing time.

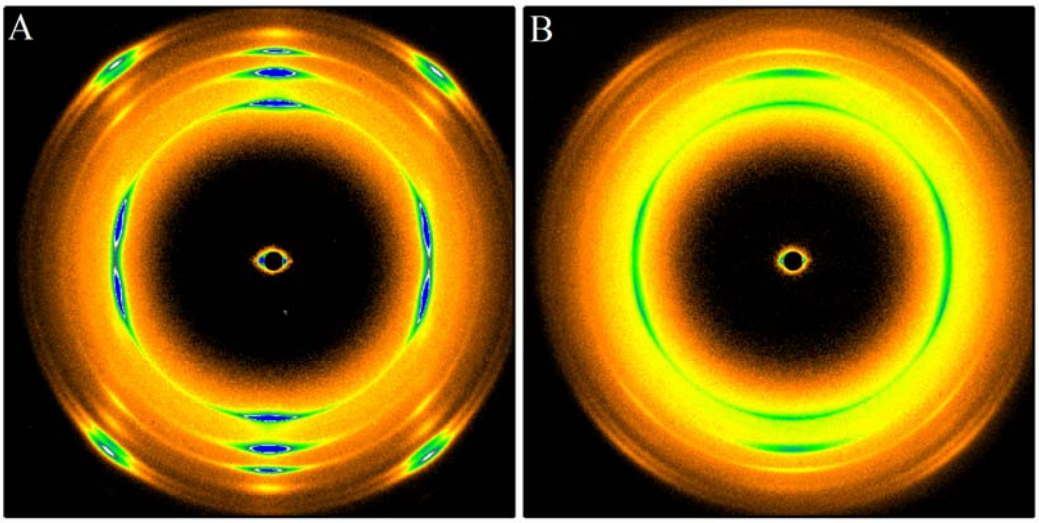

Figure 5.5: Two-dimensional WAXD patterns of B3500 at 1250 s after shearing. A strong fiberlike crystallite orientation developed in B3500 at 137 °C after shearing at σ_w = 0.06 MPa for A) 12 s and B) 3 s. Acquisition time = 30 s.

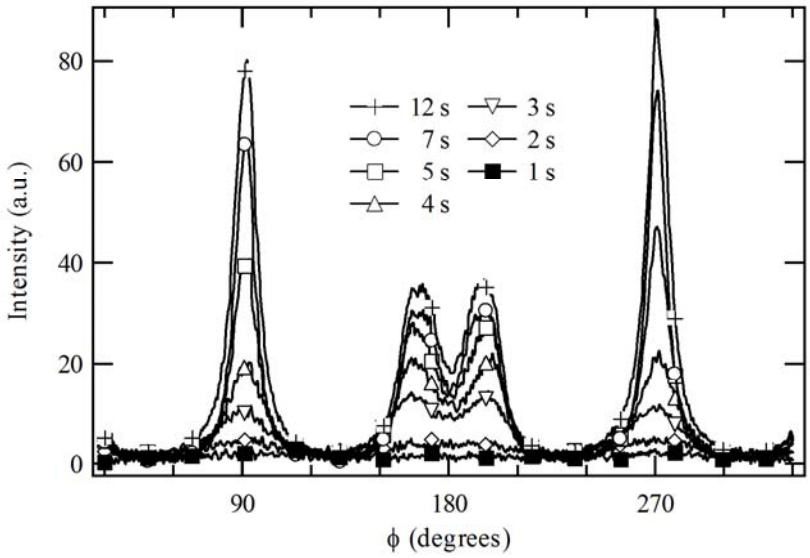

Figure 5.6: Azimuthal scans of the 110 WAXD reflection at 1250 s after shearing. It is remarkable that with as little as 2 s of shearing, (weakly) oriented crystallites are growing. For t_s = 1 s, crystallization does not have a preferential orientation.

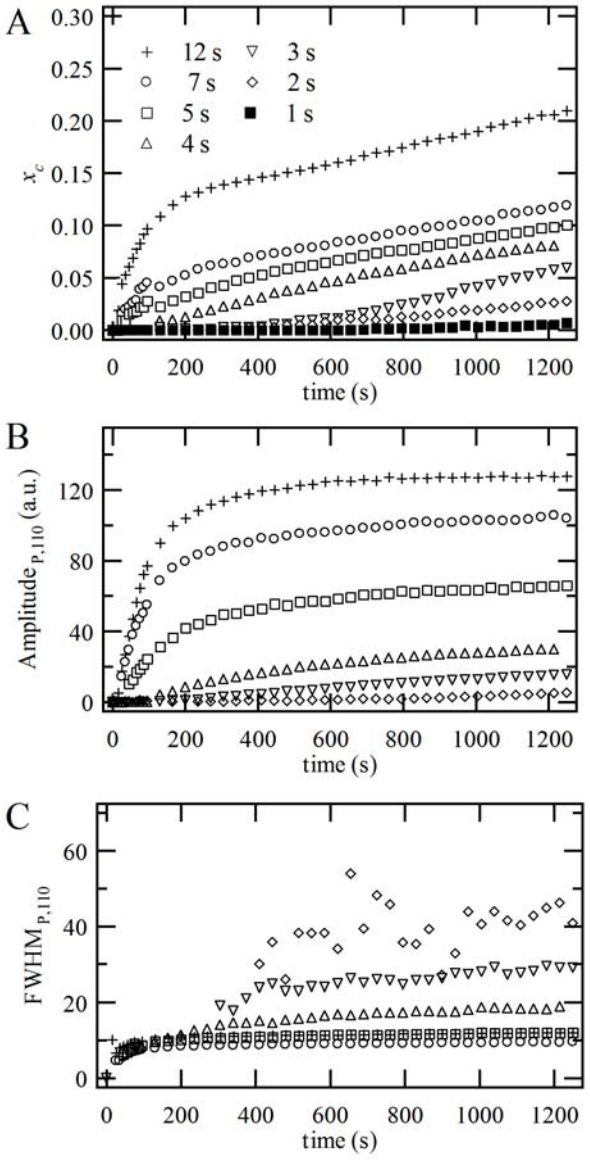

Figure 5.7: Degree of crystallinity and orientation increase with increasing shearing time. A) The crystallinity index (x_c) rises sharply for conditions where flow was imposed for longer than 3 s. A corresponding increase in the B) amplitude of parent peaks on the 110 azimuthal indicates the growth in crystallinity is due to oriented crystallites. C) The FWHM decreases for longer shearing duration up to 5 s. Further shearing does not affect a decrease in orientation distribution.

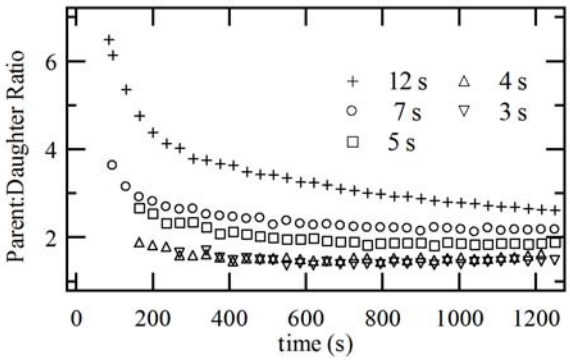

Figure 5.8: Time evolution of parent to daughter ratio of 110 peaks for different shearing durations.

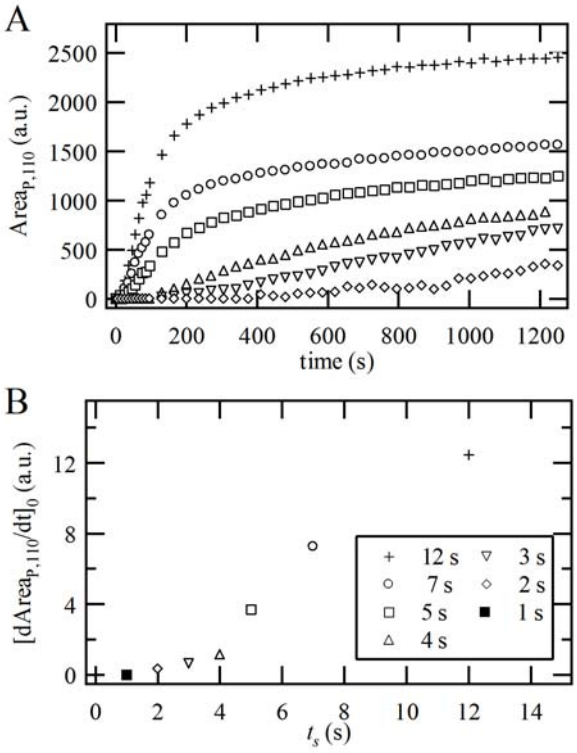

Figure 5.9: Area of the 110 parent peak. A) The area of parent 110 peaks grows faster and to substantially higher values for greater shearing times. A change in growth rate occurs when growing shish-kebabs impinge upon one another. Prior to impingement the growth rate is linear and B) the initial rate of increase, $[dArea_{P,110}/dt]_0$, of the parent area curves increases with increasing shearing time (t_s).

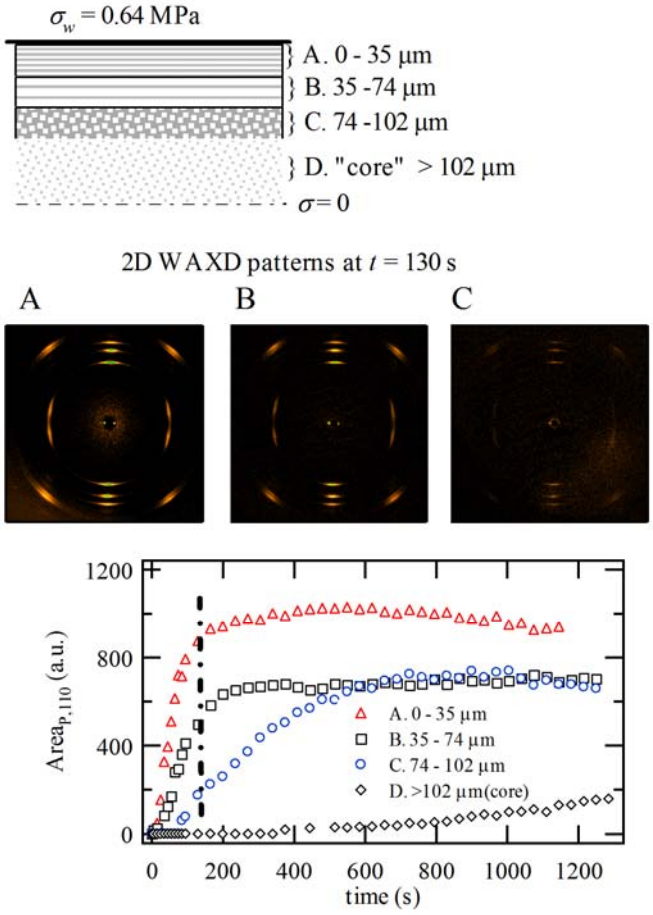

Figure 5.10: Real-time "depth sectioning" of WAXD for B3500 during crystallization at 137 °C following shear for 12 s at σ_w = 0.064 MPa. A schematic representation of the depth profile vs. stress relationship is shown (top). Examples of the resultant WAXD difference patterns at 130 s after shear (dashed line on bottom graph) for regions listed in the schematic (core not shown) are displayed (middle). Real-time development of 110 parent peak area for each depth (bottom). The depth from the wall of each section is A) 0 – 35 µm, B) 35 – 74 µm, C) 74 – 102 µm, and D) 102 µm to the center.

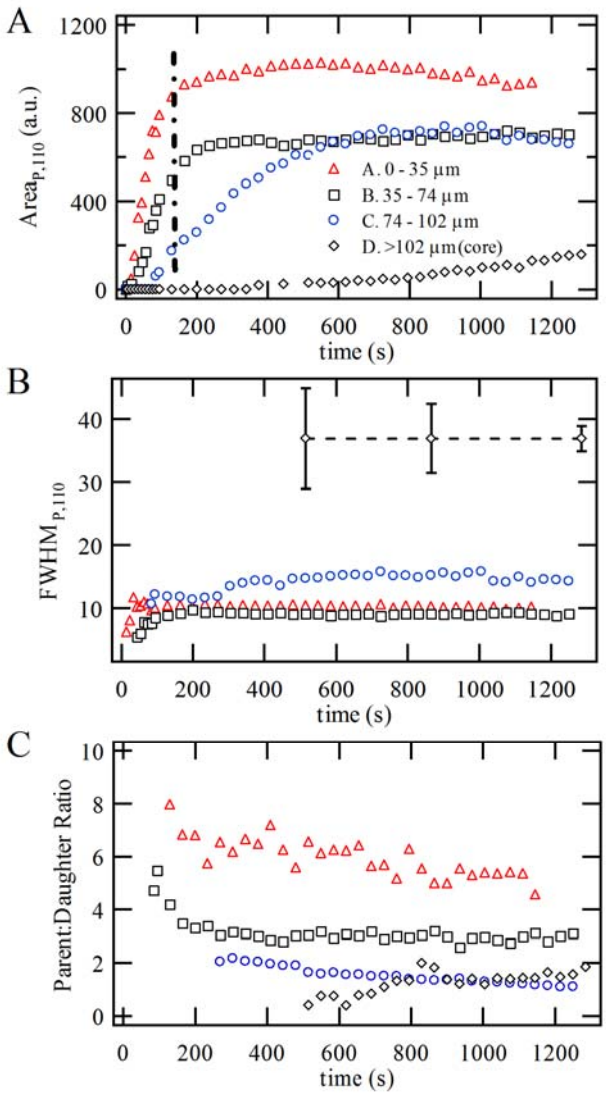

Figure 5.11: Real-time "depth sectioning" of oriented crystallites for B3500 after 12 s shearing (σ_w = 0.064 MPa). A) Area of 110 parent peaks. B) FWHM of parent 110 peaks indicates a broadening of the orientation distribution at depths closer to the center of the channel. FWHM for the "core" was difficult to determine accurately. The dashed line indicates an average of the fit values and the error bars indicate the spread. C) Parent to daughter crystallite ratio decrease at greater depth.

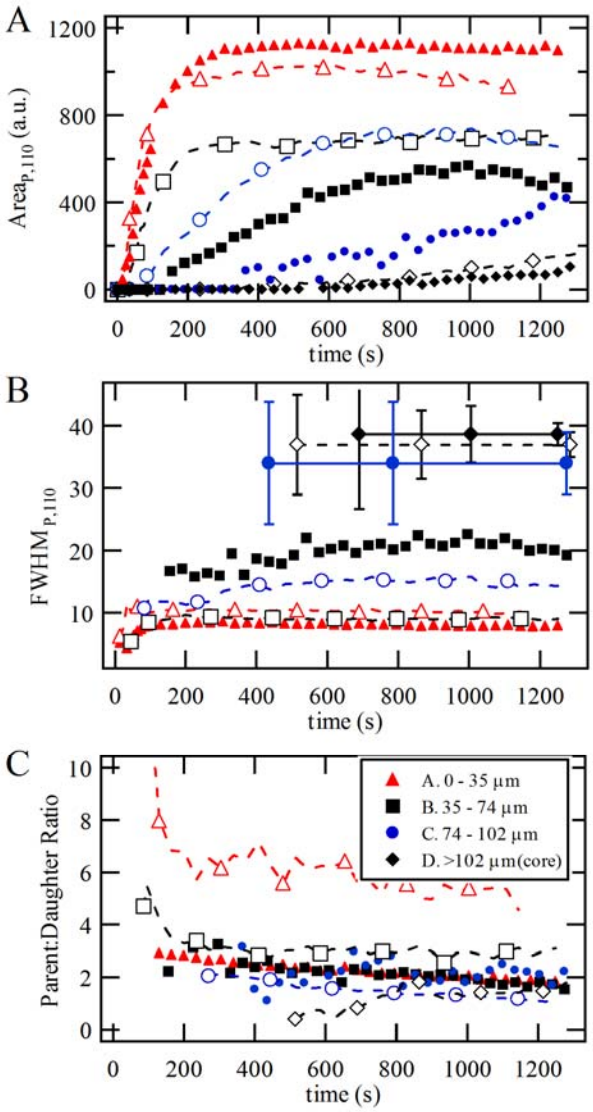

Figure 5.12: Real-time "depth sectioning" of oriented crystallites of B3500 after shearing at σ_w = 0.064 MPa for 7 s (filled symbols) and 12 s (empty symbols). A) Area of 110 parent peaks. B) FWHM of parent 110 peaks. FWHM for the "core" was difficult to determine accurately. The dashed or solid lines indicate an average of the fit values and the error bars indicate the spread. C) Parent to daughter crystallite ratio.

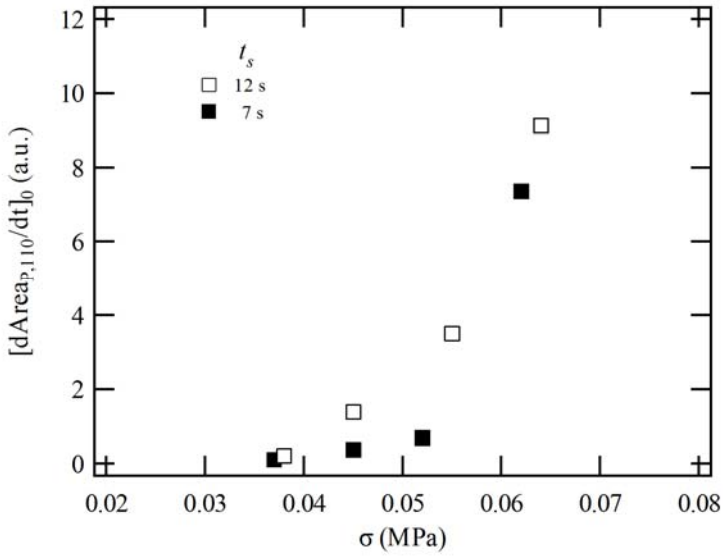

Figure 5.13: Initial rate of increase of 110 parent peak area vs. stress for "depth sections" of B3500 sheared for 7 s (filled symbols) and 12 s (empty symbols).

5.6 Bibliography

1. Doufas, A.K.; I.S. Dairanieh, and A.J. McHugh, "*A continuum model for flow-induced crystallization of polymer melts." Journal of Rheology*, **1999**. *43*: 85-109.
2. Guo, X.; A.I. Isayev, and L. Guo, "*Crystallinity and microstructure in injection moldings of isotactic polypropylenes. Part 1: A new approach to modeling and model parameters." Polymer Engineering and Science*, **1999**. *39*: 2096-114.
3. Isayev, A.I. and C.A. Hieber, "*Toward a Viscoelastic Modeling of the Injection-Molding of Polymers." Rheologica Acta*, **1980**. *19*: 168-82.
4. Bushman, A.C. and A.J. McHugh, "*A continuum model for the dynamics of flow-induced crystallization." Journal of Polymer Science Part B-Polymer Physics*, **1996**. *34*: 2393-407.
5. Eder, G. and H. Janeschitz-Kriegl, *Crystallization*, in *Processing of Polymers*, H.E.H. Meijer, Editor. 1997, Wiley-VCH: New York. p. 269-342.
6. Eder, G.; H. Janeschitzkriegl, and S. Liedauer, "*Crystallization Processes in Quiescent and Moving Polymer Melts under Heat-Transfer Conditions." Progress in Polymer Science*, **1990**. *15*: 629-714.
7. Coppola, S.; N. Grizzuti, and P.L. Maffettone, "*Microrheological modeling of flow-induced crystallization." Macromolecules*, **2001**. *34*: 5030-36.
8. Acierno, S.; S. Coppola; N. Grizzuti, and P.L. Maffettone, "*Coupling between kinetics and rheological parameters in the flow-induced crystallization of thermoplastic polymers." Macromolecular Symposia*, **2002**. *185*: 233-41.
9. Coppola, S.; L. Balzano; E. Gioffredi; P.L. Maffettone, and N. Grizzuti, "*Effects of the degree of undercooling on flow induced crystallization in polymer melts." Polymer*, **2004**. *45*: 3249-56.
10. Kumaraswamy, G.; J.A. Kornfield; F.J. Yeh, and B.S. Hsiao, "*Shear-enhanced crystallization in isotactic polypropylene. 3. Evidence for a kinetic pathway to nucleation." Macromolecules*, **2002**. *35*: 1762-69.
11. Zuidema, H.; G.W.M. Peters, and H.E.H. Meijer, "*Development and validation of a recoverable strain-based model for flow-induced crystallization of polymers." Macromolecular Theory and Simulations*, **2001**. *10*: 447-60.
12. Keller, A. and H.W.H. Kolnaar, *Flow-Induced Orientation and Structure Formation*, in *Processing of Polymers*, H.E.H. Meijer, Editor. 1997, Wiley-VCH: New York. p. 189-268.
13. Hsiao, B.S.; L. Yang; R.H. Somani; C.A. Avila-Orta, and L. Zhu, "*Unexpected shish-kebab structure in a sheared polyethylene melt." Physical Review Letters*, **2005**. *94*.
14. Li, L.B. and W.H. de Jeu, "*Shear-induced smectic ordering as a precursor of crystallization in isotactic polypropylene." Macromolecules*, **2003**. *36*: 4862-67.
15. Li, L.B. and W.H. de Jeu, "*Shear-induced smectic ordering in the melt of isotactic polypropylene." Physical Review Letters*, **2004**. *92*.
16. Li, L.B. and W.H. de Jeu, "*Shear-induced smectic ordering and crystallisation of isotactic polypropylene." Faraday Discussions*, **2005**. *128*: 299-319.
17. Somani, R.H.; L. Yang; I. Sics; B.S. Hsiao; N.V. Pogodina; H.H. Winter; P. Agarwal; H. Fruitwala, and A. Tsou, "*Orientation-induced crystallization in*

isotactic polypropylene melt by shear deformation." Macromolecular Symposia, **2002**. *185*: 105-17.

18. Kumaraswamy, G.; R.K. Verma; A.M. Issaian; P. Wang; J.A. Kornfield; F. Yeh; B.S. Hsiao, and R.H. Olley, "*Shear-enhanced crystallization in isotactic polypropylene Part 2. Analysis of the formation of the oriented "skin"." Polymer*, **2000**. *41*: 8931-40.
19. Kumaraswamy, G.; A.M. Issaian, and J.A. Kornfield, "*Shear-enhanced crystallization in isotactic polypropylene. 1. Correspondence between in situ rheo-optics and ex situ structure determination." Macromolecules*, **1999**. *32*: 7537-47.
20. Kumaraswamy, G.; R.K. Verma; J.A. Kornfield; F.J. Yeh, and B.S. Hsiao, "*Shear-enhanced crystallization in isotactic polypropylene. In-situ synchrotron SAXS and WAXD." Macromolecules*, **2004**. *37*: 9005-17.
21. Liedauer, S.; G. Eder; H. Janeschitzkriegl; P. Jerschow; W. Geymayer, and E. Ingolic, "*On the Kinetics of Shear-Induced Crystallization in Polypropylene." International Polymer Processing*, **1993**. *8*: 236-44.
22. Liedauer, S.; G. Eder, and H. Janeschitzkriegl, "*On the Limitations of Shear-Induced Crystallization in Polypropylene Melts." International Polymer Processing*, **1995**. *10*: 243-50.
23. Jerschow, P. and H. JaneschitzKriegl, "*On the development of oblong particles as precursors for polymer crystallization from shear flow: Origin of the so-called fine grained layers." Rheologica Acta*, **1996**. *35*: 127-33.
24. Jerschow, P. and H. JaneschitzKriegl, "*The role of long molecules and nucleating agents in shear induced crystallization of isotactic polypropylenes." International Polymer Processing*, **1997**. *12*: 72-77.
25. Kornfield, J.A.; G. Kumaraswamy, and A.M. Issaian, "*Recent advances in understanding flow effects on polymer crystallization." Industrial & Engineering Chemistry Research*, **2002**. *41*: 6383-92.
26. Lieberwirth, I.; J. Loos; J. Petermann, and A. Keller, "*Observation of shish crystal growth into nondeformed melts." Journal of Polymer Science Part B-Polymer Physics*, **2000**. *38*: 1183-87.
27. Wang, Z.G.; B.S. Hsiao; E.B. Sirota, and S. Srinivas, "*A simultaneous small- and wide-angle X-ray scattering study of the early stages of melt crystallization in polyethylene." Polymer*, **2000**. *41*: 8825-32.

6 EFFECTS OF LONG CHAIN REGULARITY IN BIDISPERSE BLENDS

6.1 Introduction

The strength, hardness, permeability, and clarity of semicrystalline polymers are strongly affected by the degree of crystallinity and orientation distribution of the crystallites formed under the influence of the thermal and flow history imposed during processing.[1-4] The most dramatic effects on material properties are associated with the morphological transition from qualitatively spherulitic growth to highly oriented, “row-nucleated” crystallization. Although the exact mechanism responsible for anisotropic nucleation is not known,[5-11] it is generally accepted that the longest molecules preferentially obtain a higher orientation state

during flow, leading to anisotropic crystallization. Therefore, molecular strategies for optimizing flow-induced crystallization to confer desired processing behavior may be developed based on modifying the participation of the longest chains. Here we explore the possibility of reducing the extent of oriented crystallization of isotactic polypropylene (iPP) by deliberately placing molecular defects (ethylene comonomers) in chains on the high-end of the molecular weight distribution (MWD).

The present blends are designed based on knowledge of binary blends in which the long chains (< 2% wt.) and the bulk of the chains ("base resin") are both strongly isotactic ([mmmm] > 96%) homopolymers (Chapter 3). Addition of long chains of $M_L/M_{base} > 4.5$ strongly contributes to the transition to oriented morphologies.[12] The effect is very sensitive to the relative length of the long chains and their concentration (Chapter 4). Therefore, adjustment of the length of the uppermost 1 – 2% of the MWD can profoundly alter flow-induced crystallization behavior in qualitative accord with the long-standing hypothesis put forward by Keller[13] and supported by subsequent study.[12, 14-17]

Blending polypropylenes that differ in molecular attributes such as molar mass, stereoregularity, or comonomer content provides a facile route to diverse materials. The overall molar mass distribution of the blend can be tuned to optimize melt rheology for a process of interest. In principle, the distribution of monomer-level defects (stereo- or regio-errors or comonomer) across the molar mass distribution can be use to independently optimize flow-induced crystallization characteristics. However, there is little experimental or theoretical literature to guide the design of this "defect distribution." The impetus to establish design principles has grown with the development of technologies for commercial production of bimodal and multimodal PP's. Such material can be prepared in a single reactor with two reaction zones or with two catalysts present.[18-20] Alternatively, a chain of two or more reactors can produce materials having disparate modes finely dispersed on a microscale (within "reactor granules").[3, 19-21]

It is known that monomer-level defects profoundly affect the solid-state structure and material properties (density, modulus, etc.)[22-24] and the quiescent crystallization kinetics[25-28]

of iPP. The literature is scant regarding flow-induced crystallization of bimodal distribution of monomer-level defects, particularly materials that place the defects preferentially on the long chains in the binary blend. Most studies of binary blends preferentially placed defects on the short chains in an overall distribution,[29-31] perhaps motivated by the desire to better understand the distribution of defects seen in ZN-iPP.

To expose the effects of the distribution of defects, we examine materials that have similar overall distribution of chain length and similar average comonomer content. To make contact between conclusions based on well-defined, isothermal "short term" shearing experiments and behavior in realistic (nonisothermal, extensional flow) processing histories, we examine blends that can be prepared in large enough quantity to perform pilot scale production of non-woven fabric. Indeed, the desire for fibers that are tough and extensible illustrates the motivation for establishing principles for reducing the tendency toward oriented crystallization under the influence of flow. Specifically, the high yield stress and low strain at break associated with highly oriented iPP fibers make it difficult to bond the fibers together to form the fabric, reduce the extension that the fabric can accommodate without failure, and increase the tendency of the fabric to shed fiber fragments.[32-34] We demonstrate that preferential placement of comonomer on the high end of the MWD is effective in moderating the degree of orientation induced by flow, both in isothermal shear and in fiber spinning. The conclusions based on large scale blends are confirmed by experiments on model materials in which the usual increase in oriented crystallization due to the addition of well-defined long chains is essentially "turned off" by placing molecular defects on the long chains.

6.2 Experimental

6.2.1 Materials

The samples used in the study to demonstrate the effects of monomer-level defects distributed on the high molecular weight portion of the MWD include both model polymer systems available in gram quantities and systems designed to be produced commercially. The model blends comprise a relatively low molecular weight, narrow distribution iPP (Base-PP: M_w = 186 kg/mol, M_w/M_n = 2.3, [mmmm] = 96%) with a small quantity (~1%)

of either high molecular weight (~1000 kg/mol) isotactic polypropylene, iPP, or atactic polypropylene, aPP. The long iPP has M_w = 923 kg/mol M_w/M_n = 1.3 and [mmmm] = 98%. The long aPP has M_w = 1073 kg/mol M_w/M_n = 2.2. Blends are denoted BiPP, containing 0.7 wt% iPP, and BaPP, containing 1 wt% aPP.

A large scale set of bimodal materials were designed to include pilot-scale nonwoven fabric production in the scope of experiments. So that a large enough amount of each blend could be made, we chose to use melt extrusion blending and selected the individual components from commercial resins available in large quantity. Materials intended for industrial use were provided by Procter & Gamble (Table 6.1). To produce blends having similar rheological properties and overall comonomer content, we chose pairs of "long" and "short" polymers that had similar length ("long" having M_w = 209 ± 6 kg/mol and "short" having M_w = 147 ± 4 kg/mol), one polymer in each pair being an iPP homopolymer and the other an iPP with a small amount of ethylene comonomer (2.6 – 2.9 wt% ethylene). The long homopolymer is denoted L and the long copolymer L_{EP}. Likewise, the short homopolymer and copolymer are denoted S and S_{EP}. The propylene components are commercially available iPPs: S is a metallocene-type (Exxon Achieve 3825) and L is a Ziegler-Natta-type (Exxon PP1154). The metallocene-catalyzed random copolymer (RCP) components (Japan Polychem), S_{EP} and L_{EP}, are approximately matched in ethylene content and melting point. The binary blend samples used in the study have blend ratios chosen so that both materials have M_w = 150 ± 10 kg/mol and ethylene content (C2) = 1 ± 0.2%. This represented a trade off: adjusting blend ratio to better match C2 content would increase the disparity in M_w and vice versa.

6.2.2 Molar mass

Molecular weight and molecular weight distribution for L/S_{EP} and L_{EP}/S and each component was determined at The Procter & Gamble Company by high temperature gel permeation chromatography (GPC) with multi-angle laser light scattering and refractive index detection. Measurements were conducted in trichlorobenzene (TCB) at 150 °C using three 10 μm x 300 mm mixed –B-LS columns. Samples and standards were dissolved in

TCB and filtered using 2.0 μm filter cups. BHT (2,6-di-*t*-butyl-4-methylphenol) was used as an antioxidant in the eluent.

6.2.3 Melt flow rate (MFR)

The flow characteristics of the blends and components were characterized by the melt flow rate (MFR) using ASTM standard method D1238. The MFR is commonly used as a simple metric to characterize material viscosity as the mass of polymer extruded through an orifice under specific conditions of temperature and pressure. For polypropylene, the MFR is reported in units of dg/min at 230 °C under 2.16 kg of extrusion weight. MFR values provided by The Procter & Gamble Company.

6.2.4 Quiescent crystallization

Quiescent crystallization kinetics and crystallization and melting points for L/S_{EP} and L_{EP}/S were characterized at Procter & Gamble by differential scanning calorimetry (DSC) using a TA Instruments C3A04 DSC equipped with autosampler . Crystallization kinetics were characterized using peak crystallization times for a series of crystallization temperatures. Samples were annealed at 215 °C, well above the highest estimate of T_m^0 for iPP,[35] to erase prior thermal history and mimic conditions used in shear experiments. Crystallization and melting points were determined after constant cooling and heating cycles at 10 °C/min. Melting point temperatures are reported for the second heating. In contrast to homopolymers, for which the equilibrium melting temperature can be estimated by extrapolation of observed melting points according to the Hoffman-Weeks method,[36, 37] the present blends are composed of components with widely separated melting points. At deep enough subcooling (blend crystallization temperature, T_c (blend) << T_m (RCP)), both components are incorporated into crystals; however, at shallower subcooling there are temperatures at which the RCP component does not crystallize (T_c (blend) > T_m (RCP)). Consequently, at high T_c the corresponding melting points deviate upward from a linear trend established at lower crystallization temperatures. Therefore, the estimated equilibrium melting points reported for the blends are only used for comparison of the blends to each other. Given the uncertainty in determining T_m^0, we report results in terms of T_c rather than subcooling.

6.2.5 Comonomer content

Nuclear Magnetic Resonance (NMR) spectroscopy, performed at The Procter & Gamble Company, was used to determine ethylene content in the component polymers and their blends, L/S_{EP} and L_{EP}/S. All samples were run at 135 °C in 1,2-dichlorobenzene-d4 on an INOVA 500 NMR spectrometer using a 10 mm tube without spinning. Samples were approximately 10% polymer (wt./vol.) and were heated in an oven at 145 °C for 1 – 2 hours before data collection. Data collection lasted several hours to overnight, and samples were exposed to a limited air headspace.

The approximate value of the T1 relaxation parameter was measured for each resonance using the T null method. T1 was found to be less than 1 second for each resonance. Inverse gate decoupled ^{13}C spectra were collected with D1 = 10 s (> 5*T1 so integrals would be quantitative). The methyl resonances (in the expansions of the methyl only region) were assigned based on the data in the literature.[38, 39]

6.2.6 Flow-induced crystallization

Rheo-optical characterization of flow-induced crystallization was conducted using protocols reported earlier (Chapter 2). Short-term shearing is achieved using pressure driven flow through a rectangular channel with thickness 500 μm ± 4%. To establish a consistent thermal and flow history for each experiment, the sample cell was filled with material from the reservoir and held for 5 minutes at 215 °C to ensure molecular relaxation and melting of residual crystallites. The sample cell was cooled to the crystallization temperature, T_c, and a brief shearing pulse was applied. The crystallization temperatures (T_c) were chosen such that quiescent crystallization times that were long compared to the time required to cool to T_c, ensuring that no quiescent crystallization occurred prior to application of the shearing pulse. Further, the selected T_c led to completion of flow-induced crystallization on an experimental time scale (~10^2-10^3 s) conducive to synchrotron X-ray experiments.

For model blends the effects of composition are compared at a single temperature (T_c = 137 °C) since this represents nearly constant subcooling given that all three samples are

between 99 – 100% Base-PP. For the large-scale blends, T_c's were chosen such that the quiescent crystallization times of the two blends matched. The ratios of the long and short components that gave the best match of MFRs and C2-contents of L_{EP}/S and L/S_{EP} represent a compromise that gave a somewhat greater MFR and higher melting point for L/S_{EP} (despite a greater weight percentage of comonomer defects, owing to the difference between the PP homopolymer components, mPP vs. ZN-PP, Table 6.1). Consequently, the two blends differ in terms of quiescent crystallization kinetics (Figure 6.1). To compensate for the mismatch in kinetics, the choice of crystallization temperatures (142 °C for L_{EP}/S and 145 °C for L/S_{EP}) was guided by both DSC and turbidity results (Figure 6.3), which differed from each other. Turbidity half-times ($t_{1/2}$) were 14,900 ± 5000 s for L/S_{EP} (145 °C) and 8800 ± 2400 s for L_{EP}/S (142 °C), indicating faster crystallization for L_{EP}/S at the chosen temperatures. In contrast, isothermal crystallization times from DSC (peak of the transient exotherm) were 7590 s for L/S_{EP} (145 °C) and 14,250 s for L_{EP}/S (142 °C), indicating, L/S_{EP} was faster. The results of turbidity half-times may be an indication that L_{EP}/S scatters light more prolifically than L/S_{EP} as it crystallizes. We will demonstrate that the difference in quiescent crystallization kinetics is moot in light of the overwhelming effects seen in flow-induced crystallization.

Results from rheo-optical experiments identified selected conditions for synchrotron rheo-WAXD (wide-angle X-ray diffraction) experiments at the Advanced Polymers beamline (X27C) at the National Synchrotron Light Source, a department of Brookhaven National Laboratories. The X-ray wavelength was 1.366 Å. The X-ray probes provide a relative measure of crystallinity, identification of crystalline phase, and anisotropy. Raw WAXD patterns were collected and analyzed according to the methods reported in Chapter 3 to extract crystallinity index (x_c), and metrics of oriented crystallization based on 110 azimuthal scans: parent peak area, FWHM, amplitude, and ratio of parent to daughter crystallites.

6.2.7 Flow-induced solid-state morphology

In addition to *in situ* investigation, samples were removed from the shearing apparatus for *ex situ* morphological characterization at Procter & Gamble, specifically the delineation of

the “skin-core” boundary evidenced by a highly birefringent skin. The quenched samples were sliced into thin sections (5 μm) using a Leica EM FC6 ultramicrotome for observation via polarized light optical microscopy (OM) using a Zeiss Axioplan 2 light microscope. Samples are situated with the experimental flow direction oriented at 45° relative to the crossed polarizers. The number of spherulitic superstructures within the core of the sample can be used to determine nucleation density.

6.2.8 Fiber morphology and properties

L/S_{EP} and L_{EP}/S were melt spun into fibers at take up rates of approximately 1200 m/min and collected for characterization using WAXD and tensile testing. For WAXD, fibers were gathered into small bundles and oriented in the X-ray beam with the fiber axis horizontal (direction of flow for shearing experiments).

Low speed tensile properties were measured at Procter & Gamble according to ASTM standard D3822 using an MTS Synergie™ 400 tensile testing machine (MTS Systems Corporation, Eden Prairie, MN) equipped with a 10 Newton load cell and pneumatic grips. Tests were conducted at a crosshead speed of 200% per minute on single fiber samples with a 2.54 cm gage length. Coupon mounted fibers were loaded into the tester grips and the paper was then cut away so as not to interfere with the test result. Samples were pulled to break.

6.3 Results

6.3.1 Shear-induced crystallization of model blends

The effect of long chains on the transition to oriented crystallization is strongly affected by molecular defects: following shear at σ_w = 0.11 MPa at 137 °C, the blend with < 1% of long iPP added exhibits more rapid and oriented growth than Base-PP, while the blend with 1% long aPP shows no increase in crystallization kinetics or orientation relative to Base iPP (Figure 6.2A). Thus, the addition of long iPP reduces the threshold stress required to trigger the transition to oriented crystallization. Following shear at σ_w = 0.06 MPa, none of the model materials exhibited anisotropy in optical characterization, showing that σ^*_{BiPP} is between 0.06 and 0.11 MPa. Note that the experiments shown in Figure 6.1A are not only

matched in terms of the imposed stress: the concentration is so low that the shear rate is nearly constant. Base-PP and BaPP were subjected to the same shearing time and, consequently, the same total strain and total work; BiPP was subjected to a shorter shearing time, emphasizing its increased sensitivity to flow-induced crystallization.

Oriented crystallization can be induced in Base-PP if the shear stress is sufficiently high. For example, a stress of 0.124 MPa is sufficient to induce oriented growth in Base iPP (Figure 6.2B). Thus, $\sigma^*_{Base\text{-}PP}$ is between 0.11 and 0.124 MPa. When BaPP is subjected to a stress (0.127MPa) that is greater than $\sigma^*_{Base\text{-}PP}$, it also undergoes oriented growth. This may explain the discrepancy between our findings and prior reports that long aPP can enhance the transition to oriented growth.[11] If experiments on a short iPP at $\sigma < \sigma^*_{Base}$ are compared to experiments on its blend with long aPP using the same shear rate, and hence greater shear stress, an observation of oriented growth may simply reflect the inherent characteristics of the short iPP if the imposed stress exceeds σ^*_{Base}.

6.3.2 Shear-induced crystallization of large-scale blends

Intermediate shear stress ($\sigma^*_{L/SEP} < \sigma < \sigma^*_{LEP/S}$): There is a striking contrast between the development of highly oriented crystalline microstructures in L/S_{EP} and the lack of oriented crystallization in L_{EP}/S after equivalent shear treatment over a range of shear stresses, indicating that L/S_{EP} has a lower threshold stress than L_{EP}/S. To highlight this difference, we will focus on a particular set of flow conditions and the quiescent condition at the corresponding T_c for each sample. Following shear at σ_w = 0.11 MPa, L/S_{EP} exhibited a decrease in $t_{1/2}$ by two orders of magnitude compared to the quiescent case; yet L_{EP}/S demonstrated only a modest acceleration in crystallization kinetics (Figure 6.3). To achieve comparable total strain (i.e., mass extruded, w_{ex}) at the chosen T_c, L/S_{EP} was sheared for 1.3 s and L_{EP}/S for 1.5 s. Shearing time is a relatively weak variable, so the present comparisons may be regarded as holding strain constant and shearing time nearly constant.[40] Despite the higher crystallization temperature (145 °C vs. 142 °C), slower quiescent crystallization, and shorter shearing time, L/S_{EP} has a faster timescale for shear-induced crystallization than L_{EP}/S. Crystallization of L/S_{EP} was accompanied by rapid

development of birefringence indicating the growth of anisotropic crystallites, while L_{EP}/S showed no birefringence growth after corresponding shear treatment (Figure 6.4). Thus, the large reduction in the crystallization timescale of L/S_{EP} correlates with the development of strongly oriented crystallization.

In addition, the shape of the transmittance profile over time for L/S_{EP} decreased in a two-step fashion after cessation of flow, in contrast to the simple decay observed for L_{EP}/S. Below, WAXD results show that for L/S_{EP} the first decay is associated with the rapid growth and impingement of the shish-kebab structure in the skin region near the wall, and the later decay correlates with the slower growth of the spherulitic core. The single decay observed in L_{EP}/S under these conditions is attributed solely to spherulitic growth based on rheo-optical ($I_{\perp}/I_{tot}$) and WAXD results.

The strong orientation evident in the transient birefringence correlates with growth of highly oriented crystallites observed by WAXD (Figure 6.5A). The 2-D diffraction patterns captured 30 minutes after cessation of shear indicated L/S_{EP} crystallized in the α modification for iPP with the c-axis oriented along the flow direction. The onset of crystallization in L_{EP}/S had not yet occurred after 30 minutes. L/S_{EP} shows signs of significant cross-hatching with reflections from parent crystallites oriented along the meridian and daughter crystallite reflections flanking the equator.

Following shear treatment and isothermal crystallization at T_c for 90 minutes, the solidified samples from rheo-WAXD experiments were removed for *ex situ* microscopy (Figure 6.5B). An oriented "skin" layer (39 ± 1 μm) was induced in L/S_{EP}, but no oriented crystallites were visible in L_{EP}/S. The drastic difference in morphology evident from microscopy confirms the correlation between an oriented morphology and *in situ* observation of birefringence growth after cessation of flow. Since the stress varies linearly from the wall to the channel center, the position of the "skin-core" boundary corresponds to $\sigma^* = 0.09$ MPa for L/S_{EP}. Due to the lack of an oriented skin in L_{EP}/S at $\sigma_w = 0.11$ MPa, we deduce that its threshold stress is $\sigma^* \geq 0.11$ MPa. The results indicate that introducing

irregularities (e.g., comonomer) preferentially in the high end of the MWD can moderate the effect of the long chains on flow-induced orientation.

High shear stress ($\sigma^*_{L/SEP} < \sigma^*_{LEP/S} < \sigma$): By increasing the shear stress, it was possible to induce oriented crystalline growth in L_{EP}/S. (Thus, the comonomer distribution can be regarded as changing the threshold stress). Shear treatment with σ_w = 0.15 MPa applied for 0.7 s at 142 °C was adequate to produce anisotropic crystallization in L_{EP}/S as indicated by the development of birefringence after cessation of flow. The total transmittance ($I_{tot}/I_{tot}(0)$) exhibited a bimodal decay similar to that noted earlier for L/S_{EP}. However, the initial decrease in transmitted intensity was small, corresponding to ~20% of the total intensity, followed by a plateau and final decay of the remaining transmitted intensity at longer times. As a result, application of this more intense shear stress did not alter $t_{1/2}$ for L_{EP}/S (see section 6.3.4). Corresponding rheo-optical experiments for L/S_{EP} (σ_w = 0.15 MPa, t_s = 0.7 s, T_c = 145 °C) caused rapid oriented crystallization with faster growth of birefringence and shorter $t_{1/2}$ times than L_{EP}/S, as expected based on its behavior for σ_w = 0.11 MPa.

In corresponding WAXD experiments at σ_w = 0.15 MPa, L_{EP}/S crystallized with anisotropic α-iPP structure qualitatively similar to L/S_{EP} (Figure 6.6A). However, the degree of orientation and the intensity of the reflections were much weaker for L_{EP}/S than L/S_{EP}. Further analysis of the real-time structure development is given below (see section 6.3.5).

Ex situ optical microscopy (Figure 6.6B) showed that the oriented "skin" layer induced in L/S_{EP} (94 ± 4 μm) was roughly twice the thickness of that in L_{EP}/S (48.5 ± 1.5 μm). Based on the position of the "skin-core" boundary, the threshold stress, σ^*, was calculated to be 0.09 MPa for L/S_{EP}, in accord with the results reported above, and 0.11 MPa for L_{EP}/S. L/S_{EP} had no discernable fine-grained layer, but an irregular transcrystalline layer (< 40 μm thick) extended toward the core from the inner edge of the skin. A few large spherulites appeared below the skin, most likely due to contaminants. Neither large spherulites nor a fine-grained layer were visible in L_{EP}/S. The cores of both samples were composed of tiny spherulites indicating that negligible nucleation and crystallization had occurred and that

the polymer near the center of the channel remained molten at the time the samples were quenched, 1 hour after cessation of shearing.

6.3.3 Trends with stress

The complete suite of experiments (Appendix A), which covered a range of temperatures, stresses, and shearing times, is consistent with the results outlined above. A lower threshold stress for L/S_{EP} translates into greater acceleration of crystallization kinetics and higher orientation compared to L_{EP}/S at intermediate and high stresses, $\sigma > \sigma^*$ (L/S_{EP}) (Figure 6.7A). As noted earlier, the two-stage decay of total transmitted light complicates comparison of turbidity half-times between the two blends. For instance, a plateau in the decay of transmittance for L/S_{EP} occurs near $I_{tot}/I_{tot}(0) = 0.5$, making the choice of a single $t_{1/2}$ value difficult; meanwhile, $t_{1/2}$ for L_{EP}/S hardly changed vs. stress despite changes in morphology, rendering this metric useless to differentiate the two cases. Therefore, we plot the time for the total transmitted intensity to reach 80%, $t_{0.8}$, against stress. At each stress, the $t_{0.8}$ times are shown for various shearing times. As mentioned earlier, the effect of shearing time is much weaker than that of stress, allowing meaningful comparisons to be made for the effect of stress despite variations in t_s. A strong nonlinear decrease in $t_{0.8}$ was born out for L/S_{EP}. With increasing wall shear stress, the timescale for crystallization dropped by orders of magnitude in conjunction with the development of strongly oriented crystallites. However, a relatively shallow, nonlinear trend was produced for L_{EP}/S across the same stress range. The relatively weak effect of shearing on crystallization kinetics for L_{EP}/S in response to stress is consistent with its final morphology. Even at the highest stress, L_{EP}/S formed few oriented nucleation sites confined to a thin skin.

Upon decreasing the value of T_c, we note an unexpected trend for L/S_{EP} (Figure 6.7B). The crystallization kinetics at T_c = 142 °C as a function of stress overlapped very nearly with those at 145 °C, especially at moderate to high shear stresses. This is in contrast to the trend for L_{EP}/S which shows an overall shift to faster times when comparing experiments at T_c = 137 °C and 142 °C, as expected.

6.3.4 Transient morphology development

In situ rheo-optical and rheo-WAXD probes enable the observation of real-time development of crystalline morphology. Subject to σ_w = 0.11 MPa, L_{EP}/S shows only isotropic growth in azimuthal scans of the 110 peak position (Figure 6.8A), with crystalline reflections in WAXD appearing on a timescale that accords with turbidity development in rheo-optical experiments (~2000 s). Oriented crystallization in L_{EP}/S only occurs at 0.15 MPa. Peaks in WAXD appeared about 50 s after shear with corresponding development of birefringence occurring between 25 – 40 s after shearing. The growth of oriented crystallites proceeds rapidly for approximately 1000 s at which point the overall growth of crystallinity slows (Figure 6.10A) and further oriented crystallization becomes negligible (Figure 6.8B).

Closer comparison between WAXD and rheo-optical results reveals a correlation between the initial drop in total transmittance and the change in growth rate of the 110 parent peak area (Figure 6.9). The end of the initial drop in transmittance (~40 – 54 s) coincides with the strong rise in parent peak area correlating with the rapid growth of oriented kebabs. The start of the second decay in transmittance correlates with the change in slope of parent peaks. This slope change is indicative of the onset of shish-kebab impingement. For L/S_{EP}, the impingement onset time occurs approximately 150 s after shearing at σ_w = 0.15 MPa and 180 s after shearing at σ_w = 0.11 MPa. In light of the final skin-core morphology seen in optical micrographs (Figure 6.6B), the early growth can be attributed to crystallization of shish-kebabs in the skin until impingement with further crystallization occurring mainly within the spherulitic core of the sample.

For L/S_{EP}, oriented crystallization becomes detectable by WAXD in the frame immediately after cessation of flow, at both 0.11 MPa and 0.15 MPa, and is similarly manifested as an upturn in birefringence (Figure 6.3) during the shear pulse in optical experiments. In this case the complementary optical results enable a faster detection timescale, revealing crystalline orientation with 20 ms time resolution during the shearing pulse, far faster than the 15 s required for WAXD acquisition. At 0.11 MPa, L/S_{EP} rapidly crystallizes with strong orientation. Within 35 s, the intensity due to oriented crystallites (Figure 6.8B)

grows to half of the value it eventually reached after 2500 s. This rapid crystallization behavior is evident in the two-stage development of turbidity in rheo-optical experiments (Figure 6.3), resulting in a rapid drop in transmitted intensity to approximately 0.5 within the first 50 s followed by a brief plateau and secondary drop beginning about 180 s after shearing. Between 35 s and 200 s in the WAXD experiment, the slope of x_c becomes increasingly flat (Figure 6.10A) and the intensity of the oriented crystalline peaks saturates (Figure 6.8B). L/S_{EP} behaves similarly at σ_w = 0.15 MPa only on a slightly faster timescale. WAXD and optical measurements reflect the real-time development of microstructure—oriented crystallization near the walls of the cell followed by isotropic crystallization in the core. These results are consistent with our previous findings.[41, 42] It is noteworthy that the skin thickness for L/S_{EP} at 0.11 and 0.15 MPa approximately doubles, as does the ratio of x_c at 200 s when oriented crystallization saturates. This implies that at early times, x_c is proportional to the total thread *length/vol*.

Both L/S_{EP} and L_{EP}/S crystallize more rapidly at 0.15 MPa (Figure 6.10A) and with greater crystallite orientation (Figure 6.8B); although, the crystallization kinetics and level of orientation of L_{EP}/S still lag far behind L/S_{EP} at this stress. In fact, L/S_{EP} demonstrates faster crystallization at σ_w = 0.11 MPa than L_{EP}/S at σ_w = 0.15 MPa. We analyze the transient development of oriented crystallization by fitting peaks azimuthal scans of the 110 reflection. The FWHM (Figure 6.10B) of the fits to the parent peaks (ϕ = 90° and 270°) indicates that the orientation distribution is established early in the crystallization process—templated with high fidelity by the precursors generated during flow. The distribution of c-axis orientations about the flow direction does not differ greatly for L/S_{EP} at either stress; however, FWHM is roughly twice as broad for L_{EP}/S compared to L/S_{EP} at 0.15 MPa, indicating a lower degree of orientation.

The ratio of parent to daughter crystallites indicates a decrease in cross-hatching for L/S_{EP} compared with L_{EP}/S (Figure 6.10C). For σ_w = 0.15 MPa, the parent:daughter ratio is more than two times greater for L/S_{EP} than L_{EP}/S. Since no oriented crystallites formed for L_{EP}/S at 0.11 MPa, no comparisons can be drawn between the blends at moderate stress. Comparison of the parent:daughter ratio for L/S_{EP} at both moderate and high stress reveals

a significant decrease in cross-hatching with increasing stress, in accord with our previous results[42] (Chapter 5).

6.3.5 *Ex situ* WAXD on spun fibers

The intense flow and rapid quenching involved in fiber spinning resulted in significant differences in crystallization behavior between L/S_{EP} and L_{EP}/S (Figure 6.11). Bundles of fibers of each material were examined by WAXD to ascertain level of crystalline orientation and crystal type. Fibers produced from L/S_{EP} give highly oriented diffraction patterns that closely resemble the oriented patterns captured at early times during isothermal shear-induced crystallization experiments. Some peak overlap is evident in the reflections at large scattering angles, but may be due to imperfect alignment of the fibers within the bundle rather than crystalline defects. On the other hand, L_{EP}/S fibers exhibit an entirely different behavior from the shear-induced crystallization experiments or compared to L/S_{EP} fibers. Two broad, diffuse peaks dominate the fiber pattern indicative of iPP mesophase crystallites, historically referred to as the "smectic" phase, resulting from rapidly quenched PP samples.[43,44] The mesophase has been described as paracrystalline,[45,46] microcrystalline,[47] and as distortions of either α- or β-modifications of iPP,[47,48] and remains a subject of debate.[48-50] A few very weak arcs in the positions expected for the 110, 040, and 130 reflections indicate that a small amount of α-iPP is present among the mesophase crystals. It is clear that well ordered crystallization is suppressed in L_{EP}/S fibers, but is not so in L/S_{EP} fibers.

6.3.6 Fiber mechanical properties

Tensile property tests conducted on the fibers reveal a significantly different behavior between the two blends (Figure 6.12). For fibers spun at take-up rates ~1200 m/min, the yield stress at ~30% strain is 55 MPa and 22 MPa for L/S_{EP} and L_{EP}/S, respectively. Despite a much lower yield stress, the tensile strength for L_{EP}/S (142 MPa) is not greatly diminished compared to L/S_{EP} (161 MPa). Fibers produced from L_{EP}/S demonstrate improved extensibility as indicated by the lower yield stress and higher strain at break value (L_{EP}/S: 470%; L/S_{EP}: 440%).

6.4 Discussion

The present results show that for a given molar mass distribution (designed to optimize processing rheology in this instance), the distribution of monomer-level defects can be used to produce very different flow-induced crystallization behavior in iPP. In relation to the strong role of the longest chains in an overall distribution, the results imply that placement of comonomer (or stereo-errors) on the long chains substantially reduces their ability to enhance propagation of thread-like precursors. Results obtained in short-term shearing experiments correlate well with the behavior in fiber spinning, suggesting that shear flows at high stresses can be used to determine molecular design principles that are relevant to processing flows that impose extensional or mixed flows under nonisothermal conditions. In accord with previously established relationships between solid-state morphology and fiber material properties, the ability to use molecular variables to modulate oriented crystallization translates into control of the modulus and strength of fibers.

6.4.1 Shear-induced morphology and kinetics

To expose the effect of the molecular regularity of the long chains it is necessary to hold other variables constant. One approach is to use a base resin as a control and add small amounts of long chains that are either highly uniform or have a desired frequency of local defects in chain structure. This approach definitively demonstrates that the participation of long chains in the formation of threadlike precursors can be eliminated by molecular irregularities that prevent them from crystallizing (here, atactic chain structure): long chains containing stereo-defects provide no enhancement in the formation of oriented crystallites compared to the base resin alone, in stark contrast with the blend with highly stereo-regular long chains. Technologically, however, solution blending is not acceptable economically or environmentally, and achieving a uniform dispersion of a small concentration of long chains into a bulk of shorter chains cannot be accomplished by melt blending.

Our goal is to establish the relationship between molecular structure, processing behavior, solid-state structure and properties. Therefore, one of us (JPA) designed bimodal blends that can be prepared in large amounts by melt blending. To produce homogeneous blends, the ratio of the viscosities of the long and short components was kept less than 5.

Consequently, the chain length distributions of the iPP and copolymer components overlap, and we no longer know the precise length or amount of "long chains." Instead we know average quantities and compare bimodal blends designed to hold overall comonomer content and melt rheology nearly constant. In turn, this permits comparisons under nearly matched flow conditions, particularly temperature and shear stress. Despite nearly matched ethylene comonomer content, L/S_{EP} and L_{EP}/S resins exhibited widely differing flow-induced morphologies and kinetics of crystallization, indicating the role the longest chains play in flow-induced crystallization is not only a function of their segmental orientation state but also their molecular regularity.

Monomer-level defects in the longest chains interfere with the propagation of threadlike precursors from pointlike ones. Based on a conceptual model of the strong effect of long chains in blends with uniform molecular regularity (Chapter 3), we envision (Figure 6.13) the effect of molecular defects on the participation of long chains in the events leading to oriented crystallization under flow. Our model assumes that propagation requires the adsorption of long chains to existing pointlike precursors (Figure 6.13b). Chain adsorption to the nucleus surface depends on the molecular-regularity of the adsorbing chains. The presence of various chain defects (i.e., stereo- or regio-errors, comonomers) will reduce the ability of chains to come into crystallographic registration and remain attached to the precursor surface.

A critical step in our model is the propagation of the threadlike precursor (Figure 6.13c). Chains tethered to precursor surfaces have much slower relaxation dynamics than the corresponding chains free in the melt; therefore, the adsorbed chains access higher degrees of orientation than their free counterparts and have a greater tendency to undergo chain stretching. The high level of segmental orientation just upstream and downstream of the precursor causes the local probability of ordering to be high—provided that the oriented strands can participate in ordering and recruit neighboring chains to order with them. In our model, this step is essential to the formation of threadlike precursors that eventually template oriented semicrystalline morphologies. Chain defects will frustrate the formation of stable, ordered structures from the oriented, but still molten strands adsorbed to the

precursor. In order to crystallize, polypropylene must adopt a 3_1 helical structure. Stacking of helical stems depends on interaction of the pendant methyl groups that protrude from the helix.[51] Chain defects undoubtedly disrupt the regularity of the helical structure and the ability of multiple helical stems to pack and form a long-lived structure. Without the addition of new ordered material immediately upstream and downstream of the precursor, the propagation of the oriented structure halts and crystallization proceeds with spherulitic morphology.

6.4.2 Interpretation of transient morphology development in the skin

Careful consideration of *in situ* and *ex situ* results as a whole permits a more complete understanding of the events involved in oriented crystallization. Rheo-optical and rheo-WAXD data should be interpreted in light of the final morphology to explain the underlying physical changes. For example, the two-step decay in transmittance during rheo-optical experiments was initially thought to be related to greatly suppressed crystallization kinetics in the RCP portion of the blends. However, the correlation with a change in parent crystallite growth rate measured by rheo-WAXD (Figure 6.9) shows it is instead a consequence of rapid growth and impingement of shish-kebab structures in the skin. The two-stage drop in transmittance is exhibited only when a strong crystallite orientation is induced. This interpretation is in line with results reported in Chapter 5 for a bimodal blend of highly isotactic PPs that also show two-step turbidity growth but do not possess a high defect concentration.

6.4.3 Effect of long chain regularity on spun fiber structure and properties

Current understanding of the effects of molecular characteristics of iPP on fiber processing-structure-property relationships is based primarily on experience with traditional Ziegler-Natta polypropylenes. It is known that a broad molecular weight distribution gives desirable shear thinning and melt elasticity for the melt-spinning process. In traditional ZN-iPP, the longest chains in the broad distribution are also the most stereo-regular.[52, 53] Single-site catalysts offer the potential to synthesize iPP with designed distribution of molecular regularity across the distribution in chain length. Here we explore the possibility that a series of resins could be prepared with equally desirable melt rheology but very

different solidification behavior. For some applications it is desirable to have strongly oriented crystallites (to increase tensile modulus), while in other applications mild orientation is desired (to improve fiber toughness). The results show that for fixed average comonomer content, the distribution of molecular regularity can be used to adjust the flow-induced crystallization characteristics: the tendency toward oriented crystallization is increased if defects are preferentially on the low-end and decreased if defects are mainly on the high-end of the molecular weight distribution.

Threads spun from L_{EP}/S resin demonstrated noticeably different molecular ordering and material properties. The rapid thermal quenching experienced in the fiber spinning process led to the formation of disordered α and mesophase PP crystallites. The decrease in formation of threadlike nuclei in L_{EP}/S, demonstrated in shear experiments, suppressed early growth of α-phase crystallites in the spinning process, with the consequence that highly disordered crystallites formed as the temperature plunged. Recent studies by Choi and White[54] found that low tacticity iPP (in their case isotactic triad [mm] = 0.89) led to mesophase formation in spun fibers. This is consistent with our findings for fibers of L_{EP}/S. In contrast, L/S_{EP} fibers crystallized as strongly oriented α-iPP like typical Ziegler-Natta iPP fibers. Thus, the extensional deformation imposed on the melt during fiber spinning induces formation of threadlike precursors in L/S_{EP} that template the growth of ordered α-phase crystallites as the fiber cools.

The differences in crystalline phase and microstructure give rise to the different physical properties measured for the two fiber types. In accord with prior literature,[22,34,55] strong orientation and high crystallinity correlate with a relatively high yield stress and relatively low yield strain. The transition from the yield plateau to the strain-hardening regime is also relatively low for the strongly oriented fiber (L_{EP}/S shows a pronounced plateau, and it is virtually absent in L/S_{EP}). Similarly, the stress required to break the strongly oriented fiber is greater, but the strain at break is lower than for the moderately oriented fiber.

This can be understood by considering the molecular mechanism involved in plastic deformation. For fiber samples with uniaxial orientation, plastic yield will involve several

crystalline chain slip mechanisms.[56, 57] Slip only occurs above a critical value of the shear stress resolved upon the slip plane and in the slip direction known as the critical resolved shear stress (CRSS). The relationship between the force (F) applied to the slip plane (A) and the resolved shear stress (τ) takes into account the angles between the slip plane normal and the force axis (ϕ) as well as between the slip direction and the force axis (λ), known as the Schmid factor:[57, 58]

$$\tau = \frac{F}{A}\cos\phi\cos\lambda\,, \tag{6.1}$$

In the case of extensive "shish-kebab" growth during fiber formation, one can expect high crystal chain alignment in the direction of spinning (whether in the "shish" or the "kebabs"), hence $\lambda \sim 0°$ and $\phi \sim 90°$ (with fiber symmetry). Thus, for a given critical resolved shear stress (τ_c), it takes a very high force (F_c) to initiate the chain slip process. Therefore, it is reasonable to expect a higher yield stress for fibers of L/S_{EP} that contain highly oriented crystallites. Concomitantly, one can reasonably assume that the higher the original alignment of chains, the smaller the natural draw ratio and the higher the final alignment after cold drawing, leading to lower extensibility and the higher breaking stress of the fibers.

6.4.4 Relationship to prior literature and directions for future research

Many researchers have studied the effects of comonomer content and comonomer blends on the crystallization behavior of iPP,[22, 24, 26, 28-31, 59] but most studies have focused on quiescent crystallization. Studies that did examine effects of flow[22, 29-31] had not included blends in which the defects were inversely distributed according to molecular weight (i.e., high M_w low regularity chains blended with low M_w with high regularity chains). Recently Somani, et al.[11] examined the effect of adding of a small amount of high molecular weight atactic polypropylene to a low molecular weight iPP base resin and concluded that it enhanced flow-induced crystallization. They appreciated the fact that aPP would be rejected from the crystallites, but argued that enhanced orientation of the long chains would

influence neighboring chains and explain the weak but noticeable enhancement in crystallization that they observed.

Our results for a corresponding model blend of high molecular weight atactic PP blended into a base resin do not agree with the findings of Somani. Unfortunately, Somani's experiments were not performed at the same shear stress, but at constant shear rate. Given the highly nonlinear effect of stress on crystallization, it may be that the higher stress imposed on the blend of short iPP with long aPP would have induced a similar enhancement in the crystallization of the short iPP itself. In addition, Somani investigated stresses below the threshold to produce highly oriented row structures, limiting comparison with our findings that defective long chains do not enhance the formation of oriented crystallites. However, we found no evidence of crystallization enhancement at any stress in the blend with atactic long chains compared to the base resin alone

The following predictions based on the present results and our conceptual model may serve as a guide for future research. For a fixed base resin, the addition of a given, small concentration of long chains will produce little effect on the flow-induced crystallization behavior if the long chains are atactic, moderate enhancement if their tacticity matches the base resin, and strong enhancement if the long chains are substantially more isotactic than the base resin. In particular, the threshold stress to induce oriented growth may decrease and the rate of propagation of threads may increase as the perfection of the long chains is increased (all other parameters held fixed). Analogous predictions are made for the effects of comonomer content. In the context of our simple model, disruptive comonomers on the long chains will have similar effects whether they represent a missing methyl group (ethylene comonomer) or a bulky pendant group (butene or larger comonomer). Based on our prior observation that the effects of long chains on point-like precursors are much weaker than on threadlike precursors, we expect that the effect of defects on the long chains will likewise strongly affect formation of threadlike precursors and weakly affect formation of pointlike ones.

6.5 Conclusions

It is noteworthy that the qualitative behavior observed in the melt-spinning process accords well with the trends evident in isothermal shear-induced crystallization. This has value in two respects. Scientifically, it is significant that idealized flow and thermal conditions may well reveal the physics relevant to polymer processing, which involves mixed shear and extension under non-isothermal conditions. Technologically, the ability to screen different resin compositions on a small scale can be used to optimize flow-induced crystallization characteristics prior to scale up.

We found that the addition of chain defects to the high-end of the MWD mitigates the formation of oriented precursors induced by flow. The presence of defects (comonomer content or stereo-errors) effectively lowers the threshold stress, σ^*, required to induce oriented crystallization. This effect is in accord with a simple mechanistic model of the long chains' role in the propagation of threadlike precursors.

Table 6.1 Summary of material characteristics

Blend/components	*Wt.%*	M_w [b] (kg/mol)	M_w/M_n	T_m [c] (°C)	T_m^0 [d] (°C)	*MFR*	*C2* (*Wt.%*)[e]
L/S_{EP}	100	140	3	157	174	20.2	1.2
L (ZN-PP)[a]	60	203	3.2	161		13	--
S_{EP} (mRCP)[a]	40	143	2.3	128		40	2.9
L_{EP}/S	100	159	2.2	148	171	17.6	0.8
L_{EP} (mRCP)[a]	30	215	2.4	125		7	2.6
S (mPP)[a]	70	151	2.2	150		32	--

[a]Synthetic nature of the individual component is indicated in parentheses: ZN, Ziegler-Natta catalyst; m, metallocene catalyst; PP, homopolymer; RCP, random copolymer. [b]Determined by GPC. [c]Apparent melting temperature obtained from peak position of DSC upon second heating. [d]Estimated using Hoffman-Weeks extrapolation (see text). [e]Ethylene comonomer content determined by ^{13}C NMR.

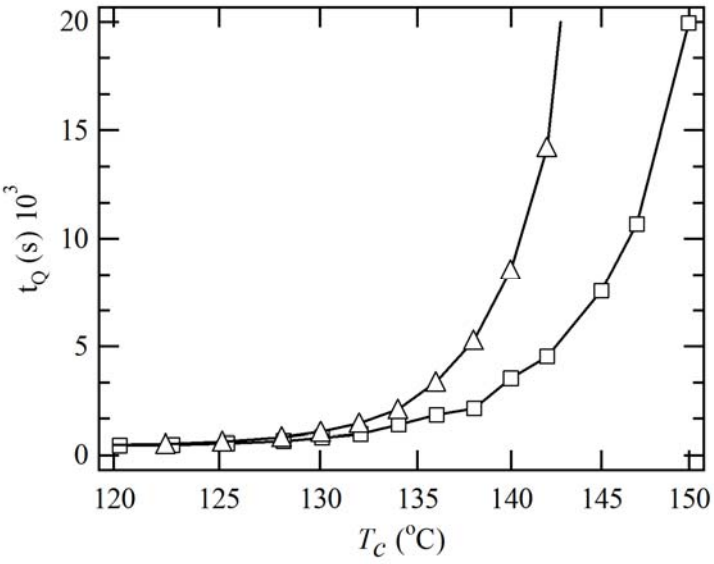

Figure 6.1: Quiescent crystallization kinetics determined by DSC for L/S_{EP} (□) and L_{EP}/S (Δ).

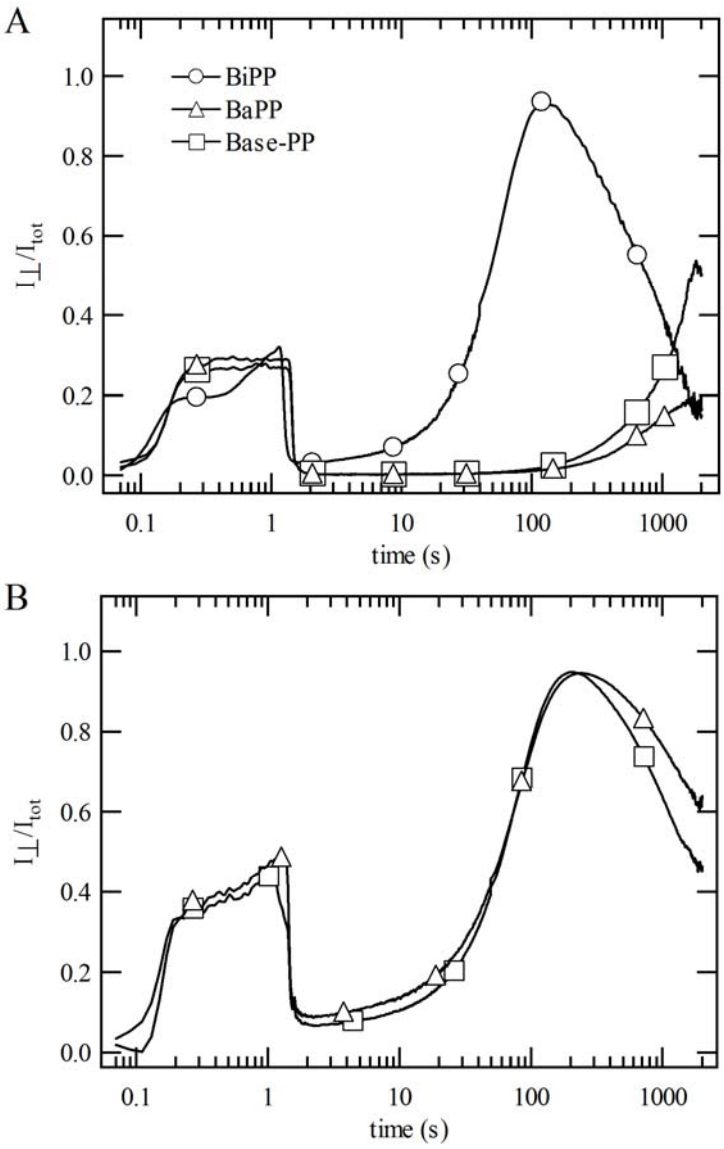

Figure 6.2: Birefringence and total transmitted intensity for model blends of isotactic and atactic polypropylenes after shearing A) at σ_w = 0.11 MPa at 137°C for 1.4 s (Base-PP and BaPP) and 1.25 s (BiPP) and B) at σ_w = 0.124 MPa (Base-PP) and σ_w = 0.127 MPa (BaPP) for 1.4 s. (Under quiescent conditions their crystallization times gauged by the turbidity half-time at 137 °C are: Base-PP, 14,000s; BaPP, 18,000s; and BiPP, 9,000s.)

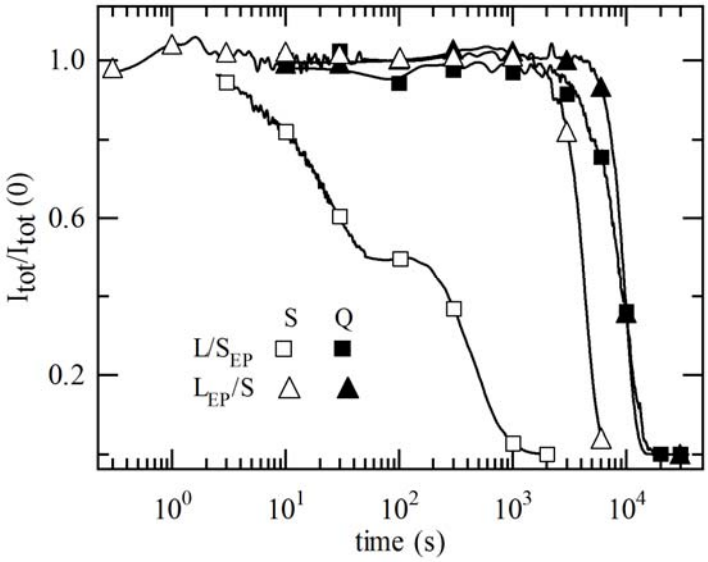

Figure 6.3: Total transmitted intensity for L/S_{EP} (145 °C) and L_{EP}/S (142 °C) under quiescent (Q) and shearing (S) conditions σ_w = 0.11 MPa. The experimental crystallization temperatures were chosen to approximately match quiescent crystallization (see text). Shearing times were chosen to match total strain (L/S_{EP}, t_s = 1.3 s; L_{EP}/S, t_s = 1.5 s),

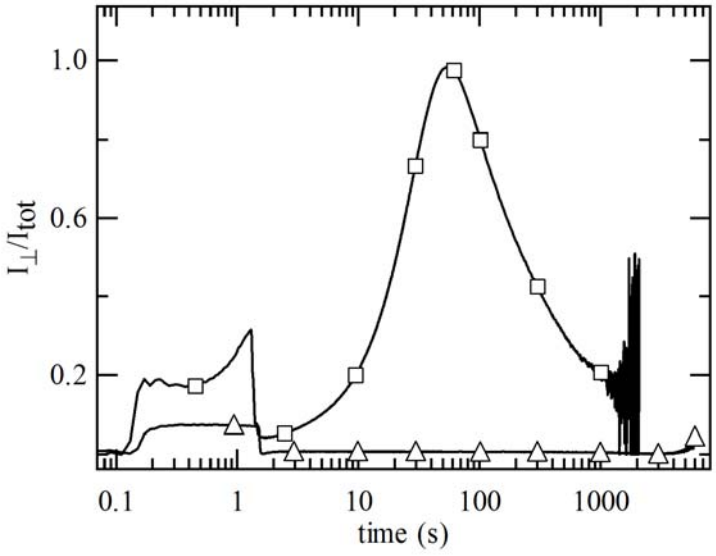

Figure 6.4: Birefringence development in L/S_{EP} (□, 145 °C, t_s = 1.3 s) and L_{EP}/S (Δ, 142 °C, t_s = 1.5 s) for σ_w = 0.11 MPa, such that $\sigma^*_{L/SEP} < \sigma_w < \sigma^*_{LEP/S}$.

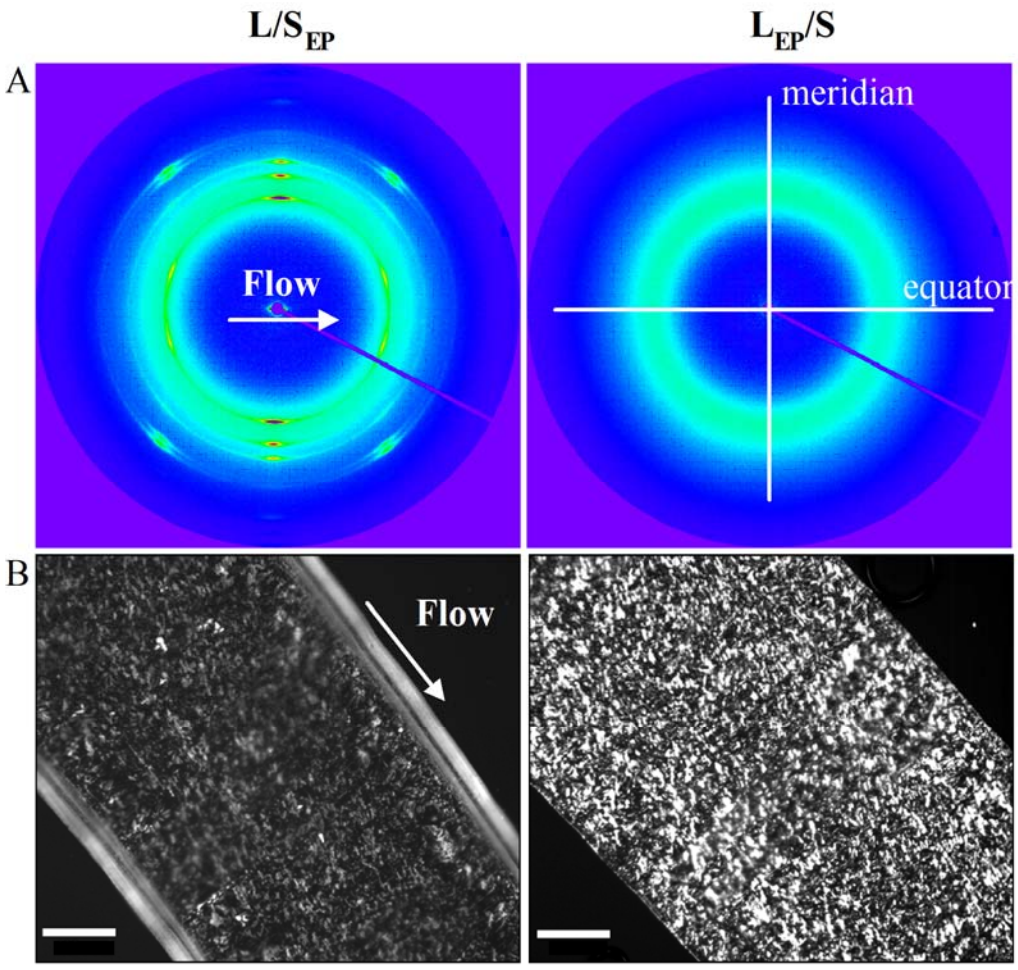

Figure 6.5: A) WAXD patterns captured for L/S_{EP} (145 °C) and L_{EP}/S (142 °C) 30 minutes after cessation of shearing at 0.11 MPa. Linear intensity scale is used. B) *Ex situ*, optical micrographs of L/S_{EP} and L_{EP}/S viewed through crossed polarizers after being subjected to shear pulse (σ_w = 0.11 MPa for t_s = 1.0 and 1.5 s, respectively) and crystallizing isothermally for 1 hour. (Note that t_s for L/S_{EP} was reduced to maintain matching total strain between rheo-optical and rheo-WAXD experiments). Scale bar, 100 μm.

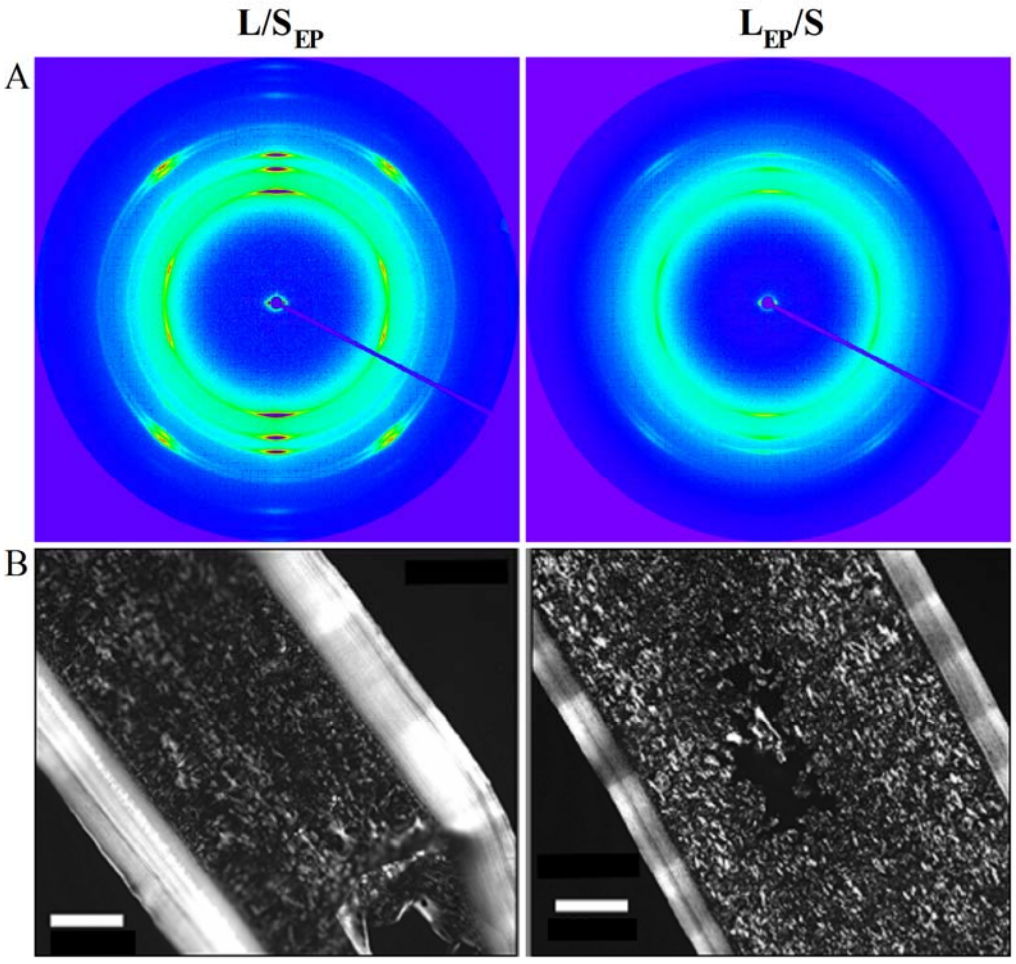

Figure 6.6: A) WAXD patterns captured for L/S_{EP} (145 °C) and L_{EP}/S (142 °C) 30 minutes after cessation of shearing at 0.15 MPa. Linear intensity scale is used. B) *Ex situ*, optical micrographs of L/S_{EP} and L_{EP}/S viewed through crossed polarizers after being subjected to shear pulse (t_s = 0.7 s at σ_w = 0.15 MPa) and crystallizing isothermally for 1 hour. Scale bar, 100 μm.

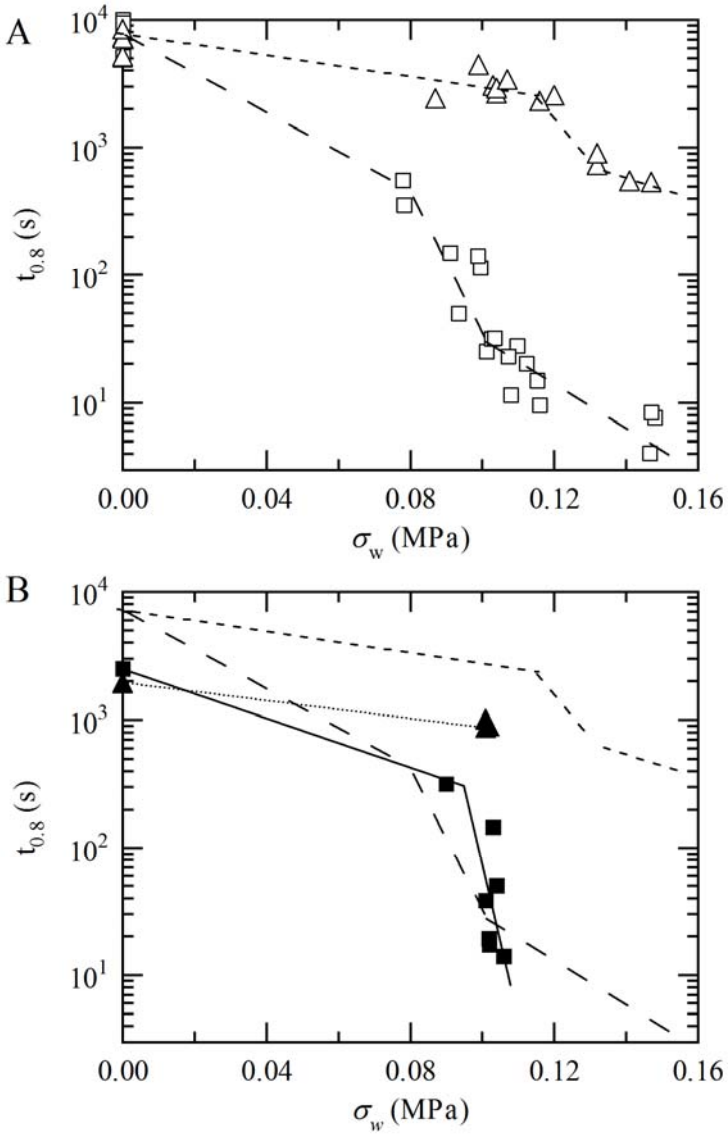

Figure 6.7: Time for transmitted intensity ($I_{tot}/I_{tot}(0)$) to reach 0.8 ($t_{0.8}$) for A) L/S_{EP} (□, 145 °C) and L_{EP}/S (Δ, 142 °C) and B) L/S_{EP} (■, 142 °C) and L_{EP}/S (▲, 137 °C) at a series of shear stresses. Trend lines are added to guide the eye. Dashed lines in A) are reproduced in B) for comparison.

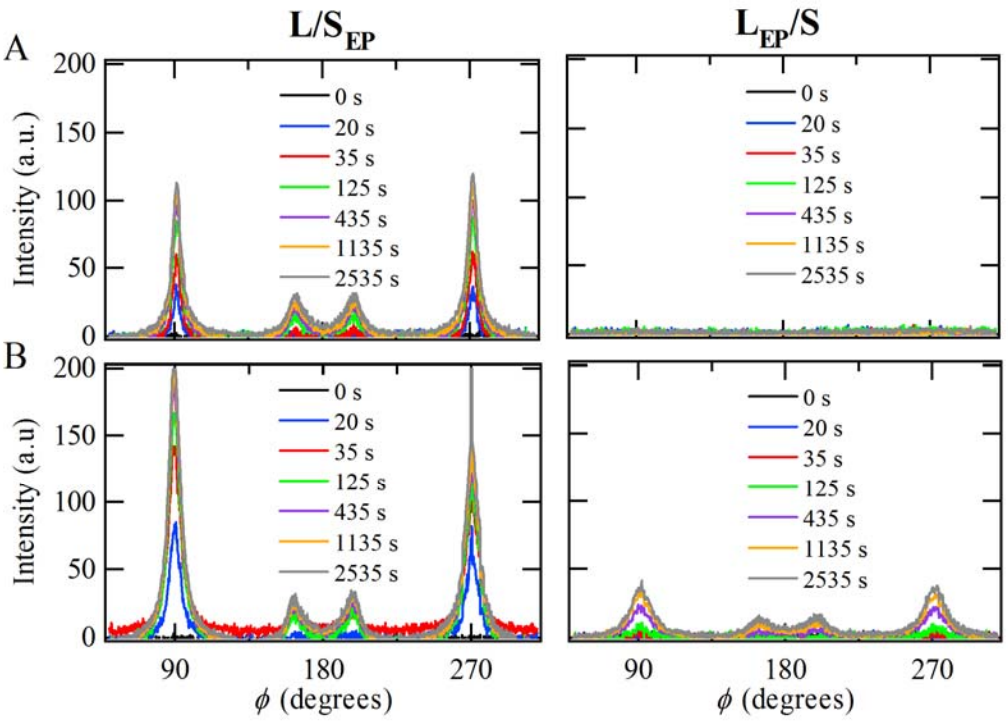

Figure 6.8: Azimuthal scans of the α-iPP 110 diffraction plane for L/S_{EP} (145 °C) and L_{EP}/S (142 °C). Results for σ_w of A) 0.11 MPa and B) 0.15 MPa. Intensity has been normalized for acquisition time and time-dependent beam intensity.

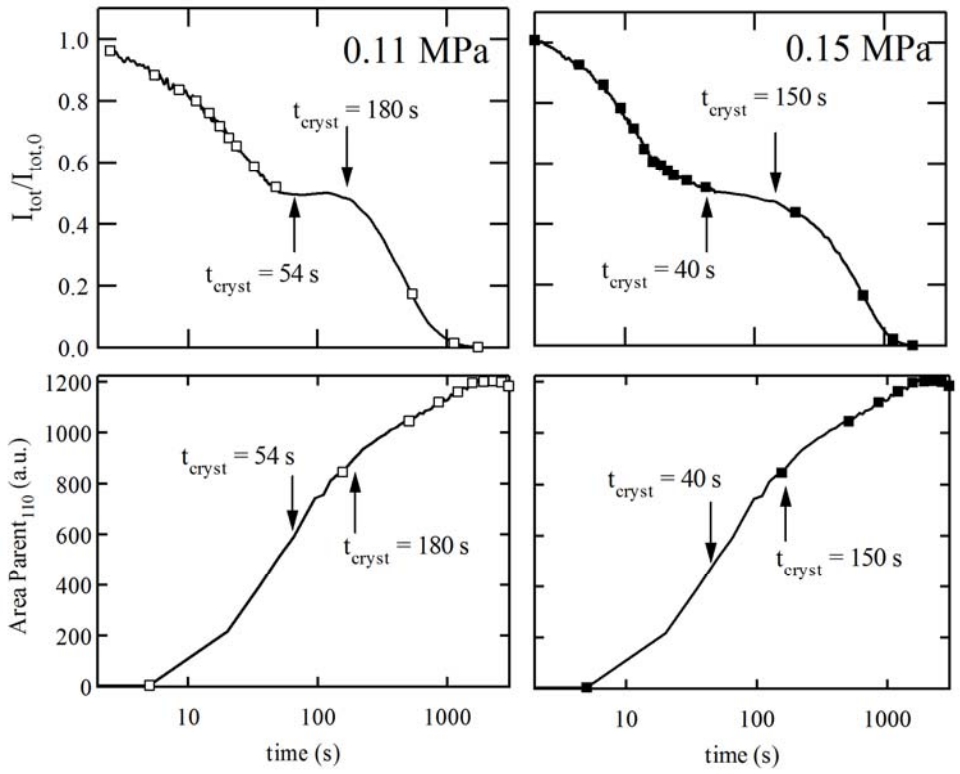

Figure 6.9: Total transmitted intensity through crossed polarizers (top) and parent peak area from azimuthal scan of 110 WAXD reflection (bottom) for L/S_{EP} at σ_w = 0.11 MPa and 0.15 MPa. Transient morphology development in the skin layer results in distinct slope changes in the real-time transmittance correlating with the onset of shish-kebab impingement indicated by change in parent peak area growth rate.

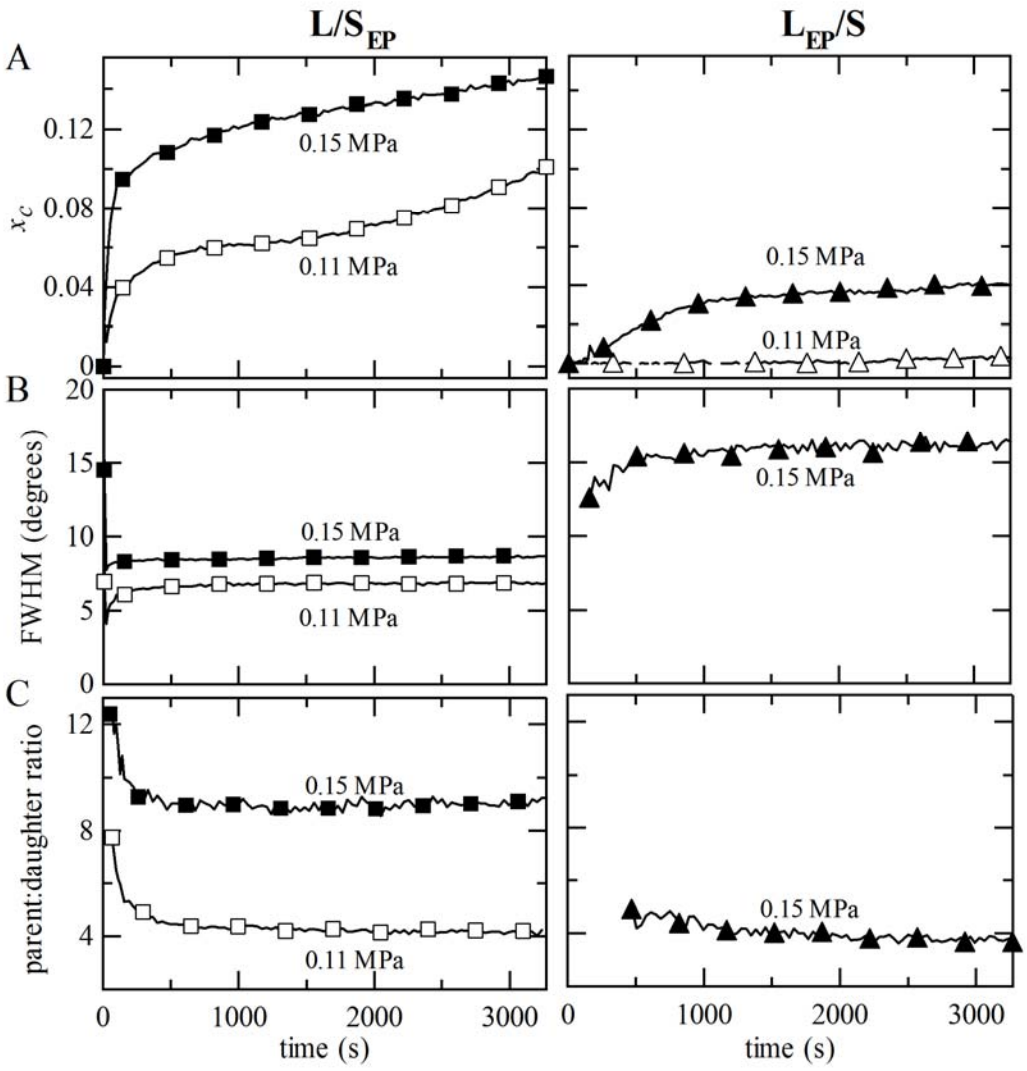

Figure 6.10: Time-resolved WAXD analysis of A) crystallinity index (x_c), B) full-width at half-maximum (FWHM) of Lorentzian fits to parent 110 peaks, and C) parent:daughter ratio (see text) for 110 peaks for L/S_{EP} (145 °C) and L_{EP}/S (142 °C).

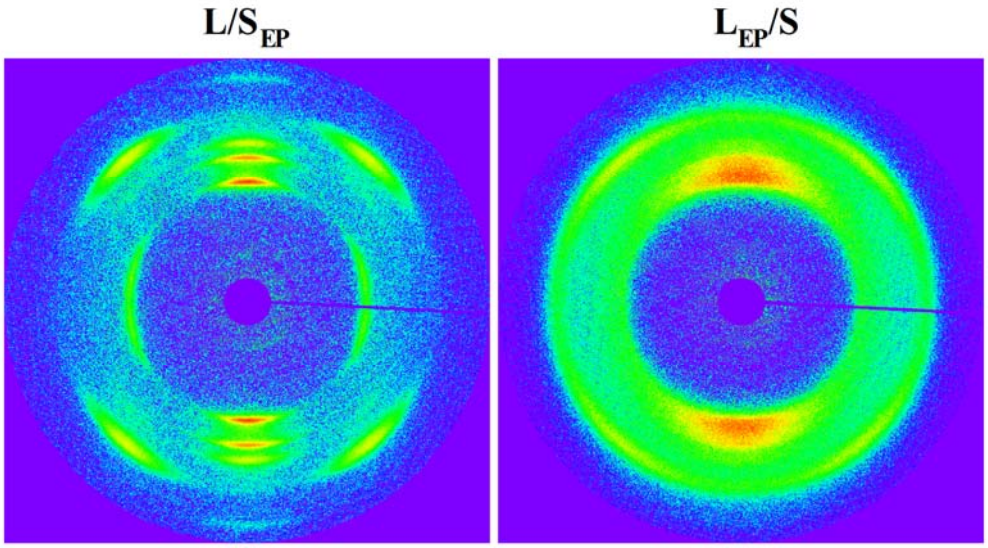

Figure 6.11: Two dimensional WAXD patterns for fibers spun from L/S_{EP} (left) and L_{EP}/S (right) blends.

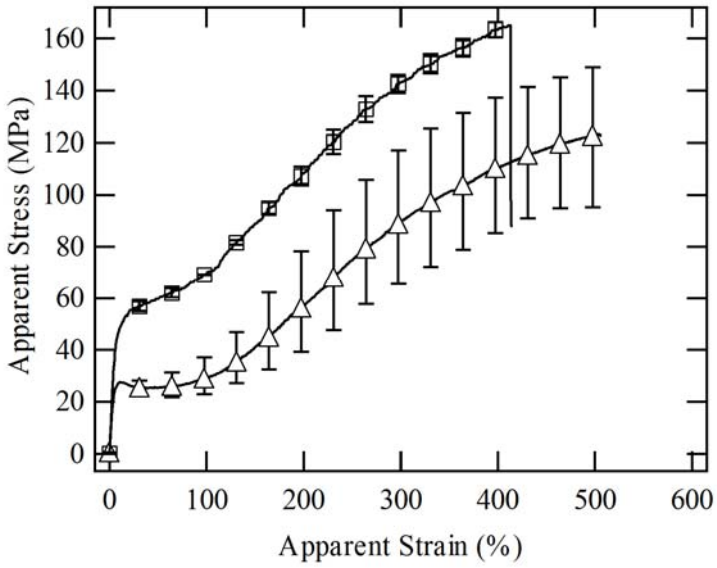

Figure 6.12: Tensile stress curves for spun fibers of L/S_{EP} (□) and L_{EP}/S (Δ) drawn at approximately 1200 m/min. Fiber diameters were ~ 30 μm.

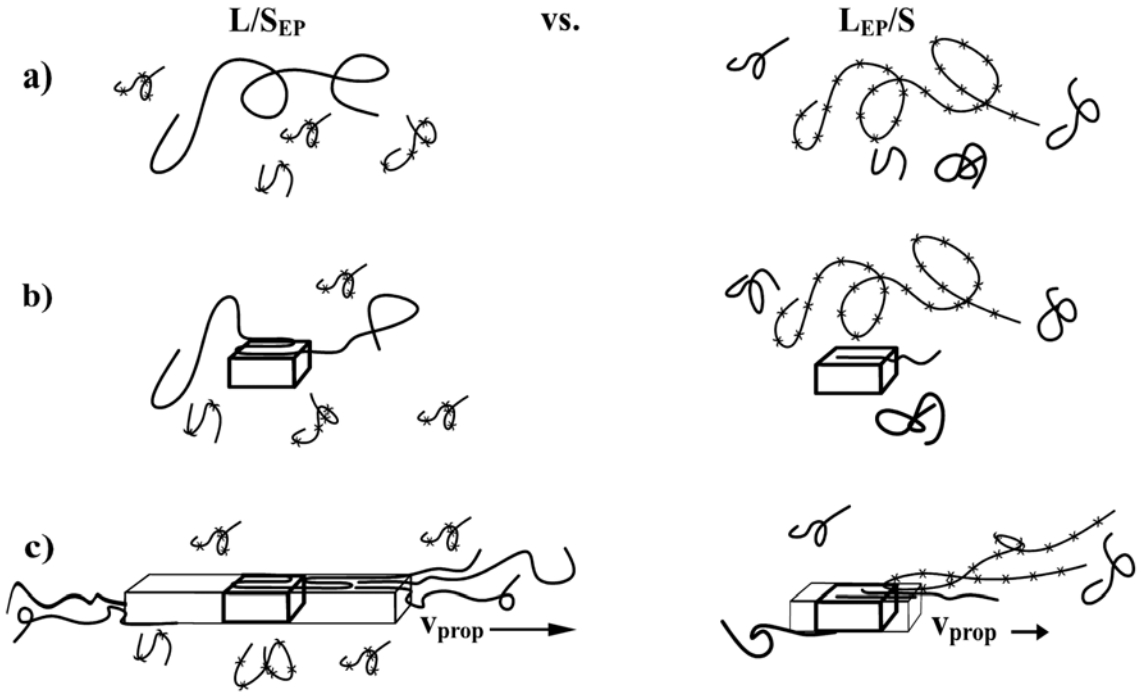

Figure 6.13: Schematic representation of the effect of chain defects on the events leading to oriented crystallization. a) Chain defects on short chains (L/S_{EP}) vs. long chains (L_{EP}/S). b) Chain defects retard the process of adsorption to a point-like nucleus. For L/S_{EP} the effect is minimal since long chains dominate this process, but for L_{EP}/S there is a profound effect since defective long chains are difficult to attach. Further, propagation accomplished by short chains requires a higher stress. c) A local concentration of oriented, "crystallizable" segments is necessary to propagate threadlike nuclei. In L/S_{EP} this is readily available. However, in L_{EP}/S any long chains that attach to the point-like nucleus are less effective due to reduce ability to crystallize. This creates a discrepancy in the apparent thread propagation velocity (v_{prop}).

6.6 Bibliography

1. Karger-Kocsis, J., ed. *Polypropylene: Structure, blends and composites*. 1st ed. Vol. 1. 1995, Chapman & Hall: New York.
2. Andreassen, E.; A. Larsen; K. Nord-Varhaug; M. Skar, and H. Oysaed, "*Haze of polyethylene films - Effects of material parameters and clarifying agents." Polymer Engineering and Science*, **2002**. *42*: 1082-97.
3. Rudin, A., *The Elements of Polymer Science and Engineering*. 2nd ed. 1999, New York: Academic Press.
4. Bartczak, Z. and E. Martuscelli, "*Orientation and properties of sequentially drawn films of an isotactic polypropylene hydrogenated oligocyclopentadiene blend." Polymer*, **1997**. *38*: 4139-49.
5. Olmsted, P.D.; W.C.K. Poon; T.C.B. McLeish; N.J. Terrill, and A.J. Ryan, "*Spinodal-assisted crystallization in polymer melts." Physical Review Letters*, **1998**. *81*: 373-76.
6. Strobl, G., "*From the melt via mesomorphic and granular crystalline layers to lamellar crystallites: A major route followed in polymer crystallization?" European Physical Journal E*, **2000**. *3*: 165-83.
7. Lotz, B., "*What can polymer crystal structure tell about polymer crystallization processes?" European Physical Journal E*, **2000**. *3*: 185-94.
8. Cheng, S.Z.D.; C.Y. Li, and L. Zhu, "*Commentary on polymer crystallization: Selection rules in different length scales of a nucleation process." European Physical Journal E*, **2000**. *3*: 195-97.
9. Li, L.B. and W.H. de Jeu, "*Shear-induced smectic ordering and crystallisation of isotactic polypropylene." Faraday Discussions*, **2005**. *128*: 299-319.
10. Muthukumar, M., "*Commentary on theories of polymer crystallization." European Physical Journal E*, **2000**. *3*: 199-202.
11. Somani, R.H.; L. Yang; B.S. Hsiao, and H. Fruitwala, "*Nature of shear-induced primary nuclei in iPP melt." Journal of Macromolecular Science-Physics*, **2003**. *B42*: 515-31.
12. Seki, M.; D.W. Thurman; J.P. Oberhauser, and J.A. Kornfield, "*Shear-mediated crystallization of isotactic polypropylene: The role of long chain-long chain overlap." Macromolecules*, **2002**. *35*: 2583-94.
13. Keller, A. and H.W.H. Kolnaar, *Flow-Induced Orientation and Structure Formation*, in *Processing of Polymers*, H.E.H. Meijer, Editor. 1997, Wiley-VCH: New York. p. 189-268.
14. Duplay, C.; B. Monasse; J.M. Haudin, and J.L. Costa, "*Shear-induced crystallization of polypropylene: influence of molecular structure." Polymer International*, **1999**. *48*: 320-26.
15. Somani, R.H.; B.S. Hsiao; A. Nogales; S. Srinivas; A.H. Tsou; I. Sics; F.J. Balta-Calleja, and T.A. Ezquerra, "*Structure development during shear flow-induced crystallization of i-PP: In-situ small-angle X-ray scattering study." Macromolecules*, **2000**. *33*: 9385-94.
16. Vleeshouwers, S. and H.E.H. Meijer, "*A rheological study of shear induced crystallization." Rheologica Acta*, **1996**. *35*: 391-99.

17. Jerschow, P. and H. JaneschitzKriegl, "*The role of long molecules and nucleating agents in shear induced crystallization of isotactic polypropylenes." International Polymer Processing*, **1997**. *12*: 72-77.
18. Kulshreshtha, A.K. and S. Talapatra, *Competitive New Technologies in Polyolefin Synthesis and Materials*, in *Handbook of Polyolefins*, C. Vasile, Editor. 2000, Marcel Dekker, Inc.: New York. p. 1-69.
19. Hamielec, A.E. and J.B.P. Soares, "*Polymerization reaction engineering - Metallocene catalysts." Progress in Polymer Science*, **1996**. *21*: 651-706.
20. Fink, G.; B. Steinmetz; J. Zechlin; C. Przybyla, and B. Tesche, "*Propene polymerization with silica-supported metallocene/MAO catalysts." Chemical Reviews*, **2000**. *100*: 1377-90.
21. Yu, E.Y.; B.R. Choi, and H.J. Moon, "*Change of properties of polymer with polymerization modes in ethylene polymerization." Polymer-Korea*, **1996**. *20*: 260-70.
22. Spruiell, J.E.; F.M. Lu; Z. Ding, and G. Richeson, "*The influence of isotacticity, ethylene comonomer content, and nucleating agent additions on the structure and properties of melt-spun isotactic polypropylene filaments." Journal of Applied Polymer Science*, **1996**. *62*: 1965-75.
23. Koike, Y. and M. Cakmak, "*Atomic force microscopy observations on the structure development during uniaxial stretching of PP from partially molten state: Effect of isotacticity." Macromolecules*, **2004**. *37*: 2171-81.
24. Lustiger, A.; C.N. Marzinsky, and R.R. Mueller, "*Spherulite boundary strengthening concept for toughening polypropylene." Journal of Polymer Science Part B-Polymer Physics*, **1998**. *36*: 2047-56.
25. Bond, E.B. and J.E. Spruiell, "*The effects of atacticity, comonomer content, and configurational defects on the equilibrium melting temperature of monoclinic isotactic polypropylene." Journal of Applied Polymer Science*, **2001**. *81*: 229-36.
26. Bartczak, Z.; A. Galeski; E. Martuscelli, and H. Janik, "*Primary Nucleation Behavior in Isotactic Polypropylene Ethylene Propylene Random Copolymer Blends." Polymer*, **1985**. *26*: 1843-48.
27. Bartczak, Z. and A. Galeski, "*Homogeneous Nucleation in Polypropylene and Its Blends by Small-Angle Light-Scattering." Polymer*, **1990**. *31*: 2027-38.
28. Laihonen, S.; U.W. Gedde; P.E. Werner, and J. MartinezSalazar, "*Crystallization kinetics and morphology of poly(propylene-stat-ethylene) fractions." Polymer*, **1997**. *38*: 361-69.
29. D'Orazio, L. and G. Cecchin, "*Isotactic polypropylene/ethylene-co-propylene blends: effects of composition on rheology, morphology and properties of injection moulded samples." Polymer*, **2001**. *42*: 2675-84.
30. D'Orazio, L.; C. Mancarella; E. Martuscelli; G. Sticotti, and G. Cecchin, "*Isotactic polypropylene/ethylene-co-propylene blends: Influence of the copolymer microstructure on rheology, morphology, and properties of injection-molded samples." Journal of Applied Polymer Science*, **1999**. *72*: 701-19.
31. D'Orazio, L.; C. Mancarella; E. Martuscelli; G. Cecchin, and R. Corrieri, "*Isotactic polypropylene/ethylene-co-propylene blends: effects of the copolymer*

microstructure and content on rheology, morphology and properties of injection moulded samples." Polymer, **1999**. *40*: 2745-57.

32. Autran, J.P., *New polyolefin formulations for highly extensible nonwovens*. 2005: Cincinnati. p. Personal communication.
33. Zhang, D.; Q. Sun; G. Bhat, and L. Wadsworth, "*Structure and property characterization of spunbonded filaments and webs using thermal analysis." Journal of Applied Polymer Science*, **1998**. *69*: 421-34.
34. Bond, E.B. and J.E. Spruiell, "*Melt spinning of metallocene catalyzed polypropylenes. II. As-spun filament structure and properties." Journal of Applied Polymer Science*, **2001**. *82*: 3237-47.
35. Fatou, J.G., "*Melting Temperature and Enthalpy of Isotactic Polypropylene." European Polymer Journal*, **1971**. *7*: 1057.
36. Hoffman, J.D. and J.J. Weeks, "*Melting Process and Equilibrium Melting Temperature of Polychlorotrifluoroethylene." Journal of Research of the National Bureau of Standards Section a-Physics and Chemistry*, **1962**. *66*: 13.
37. Hoffman, J.D. and J.J. Weeks, "*Rate of Spherulitic Crystallization with Chain Folds in Polychlorotrifluoroethylene." Journal of Chemical Physics*, **1962**. *37*: 1723-&.
38. Aoki, A.; T. Hayashi, and T. Asakura, "*C-13 Nmr Chemical-Shift Assignments of Comonomer Sequences in a 1-Butene Propylene Copolymer." Macromolecules*, **1992**. *25*: 155-60.
39. Brandolini, A.J. and D.D. Hills, *NMR Spectra of Polymers and Polymer Additives*. 2000, Marcel Dekker: New York. p. 129.
40. Kumaraswamy, G.; A.M. Issaian, and J.A. Kornfield, "*Shear-enhanced crystallization in isotactic polypropylene. 1. Correspondence between in situ rheo-optics and ex situ structure determination." Macromolecules*, **1999**. *32*: 7537-47.
41. Kumaraswamy, G.; R.K. Verma; A.M. Issaian; P. Wang; J.A. Kornfield; F. Yeh; B.S. Hsiao, and R.H. Olley, "*Shear-enhanced crystallization in isotactic polypropylene Part 2. Analysis of the formation of the oriented "skin"." Polymer*, **2000**. *41*: 8931-40.
42. Kumaraswamy, G.; R.K. Verma; J.A. Kornfield; F.J. Yeh, and B.S. Hsiao, "*Shear-enhanced crystallization in isotactic polypropylene. In-situ synchrotron SAXS and WAXD." Macromolecules*, **2004**. *37*: 9005-17.
43. Decandia, F.; P. Iannelli; G. Staulo, and V. Vittoria, "*Crystallization of Oriented Smectic Polypropylene .1. Thermally Induced Crystallization." Colloid and Polymer Science*, **1988**. *266*: 608-13.
44. Saraf, R. and R.S. Porter, "*Considerations on the Structure of Smectic Polypropylene." Molecular Crystals and Liquid Crystals*, **1985**. *2*: 85-93.
45. Miller, R.L., "*On the Existence of near-Range Order in Isotactic Polypropylenes." Polymer*, **1960**. *1*: 135-43.
46. Zannetti, R.; G. Celotti; A. Fichera, and Francesc.R, "*Structural Effects of Annealing Time and Temperature on Paracrystal-Crystal Transition in Isotactic Polypropylene." Makromolekulare Chemie*, **1969**. *128*: 137-&.
47. Gailey, J.A. and R.H. Ralston, "*The Quenched State of Polypropylene." Spe Transactions*, **1964**. *4*: 29-33.

48. Corradini, P.; V. Petraccone; C. Derosa, and G. Guerra, "*On the Structure of the Quenched Mesomorphic Phase of Isotactic Polypropylene." Macromolecules*, **1986**. *19*: 2699-703.
49. Wunderlich, B. and J. Grebowicz, "*Thermotropic Mesophases and Mesophase Transitions of Linear, Flexible Macromolecules." Advances in Polymer Science*, **1984**. *60-1*: 1-59.
50. Bruckner, S.; S.V. Meille; V. Petraccone, and B. Pirozzi, "*Polymorphism in Isotactic Polypropylene." Progress in Polymer Science*, **1991**. *16*: 361-404.
51. Lotz, B.; J.C. Wittmann, and A.J. Lovinger, "*Structure and morphology of poly(propylenes): A molecular analysis." Polymer*, **1996**. *37*: 4979-92.
52. Paukkeri, R. and A. Lehtinen, "*Fractionation of Polypropylenes Using Soxhlet Extraction Methods." Polymer*, **1994**. *35*: 1673-79.
53. Lehtinen, A. and R. Paukkeri, "*Fractionation of Polypropylene According to Molecular-Weight and Tacticity." Macromolecular Chemistry and Physics*, **1994**. *195*: 1539-56.
54. Choi, D.M. and J.L. White, "*Crystallization and orientation development in fiber and film processing of polypropylenes of varying stereoregular form and tacticity." Polymer Engineering and Science*, **2004**. *44*: 210-22.
55. Bond, E.B. and J.E. Spruiell, "*Melt spinning of metallocene catalyzed polypropylenes. I. On-line measurements and their interpretation." Journal of Applied Polymer Science*, **2001**. *82*: 3223-36.
56. Peterlin, A., "*Molecular Model of Drawing Polyethylene and Polypropylene." Journal of Materials Science*, **1971**. *6*: 490.
57. Young, R.J.; P.B. Bowden; J.M. Ritchie, and J.G. Rider, "*Deformation Mechanisms in Oriented High-Density Polyethylene." Journal of Materials Science*, **1973**. *8*: 23-36.
58. Schmid, E. and W. Boas, *Plasticity of crystals with special reference to metals.* 1968, London: Chapman & Hall. 353.
59. Gahleitner, M.; P. Jaaskelainen; E. Ratajski; C. Paulik; J. Reussner; J. Wolfschwenger, and W. Neissl, "*Propylene-ethylene random copolymers: Comonomer effects on crystallinity and application properties." Journal of Applied Polymer Science*, **2005**. *95*: 1073-81.

APPENDIX A

We include a summary of additional rheo-optical data collected during investigation of L_{EP}/S and S/L_{EP} (Chapter 6). Figure captions denote shear-induced crystallization conditions.

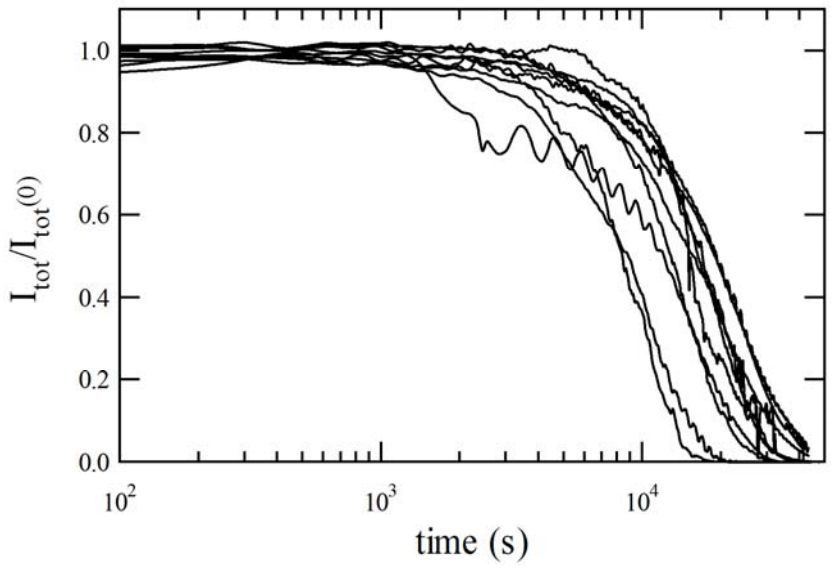

Figure A.1: Summary of total transmitted intensity for quiescent crystallization experiments of L/S_{EP} at T_c = 145 °C.

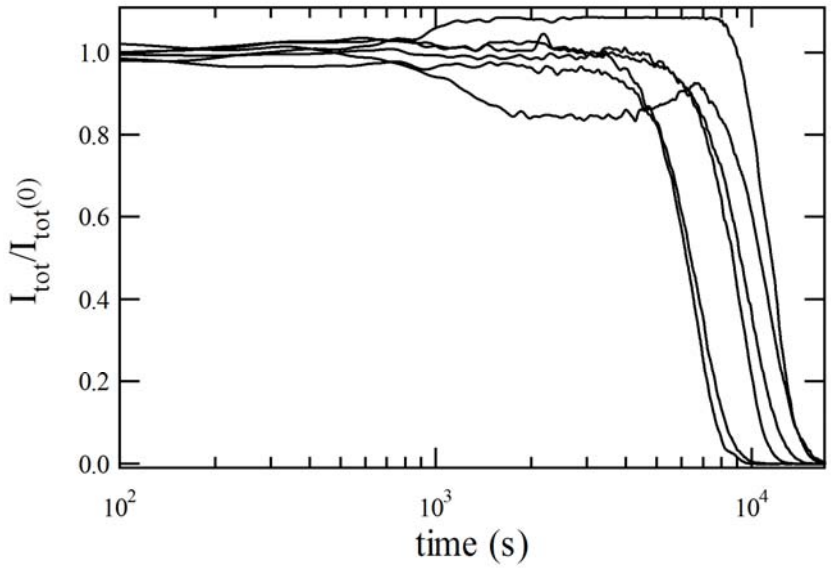

Figure A.2: Summary of total transmitted intensity of quiescent crystallization experiments for L_{EP}/S at T_c = 142 °C.

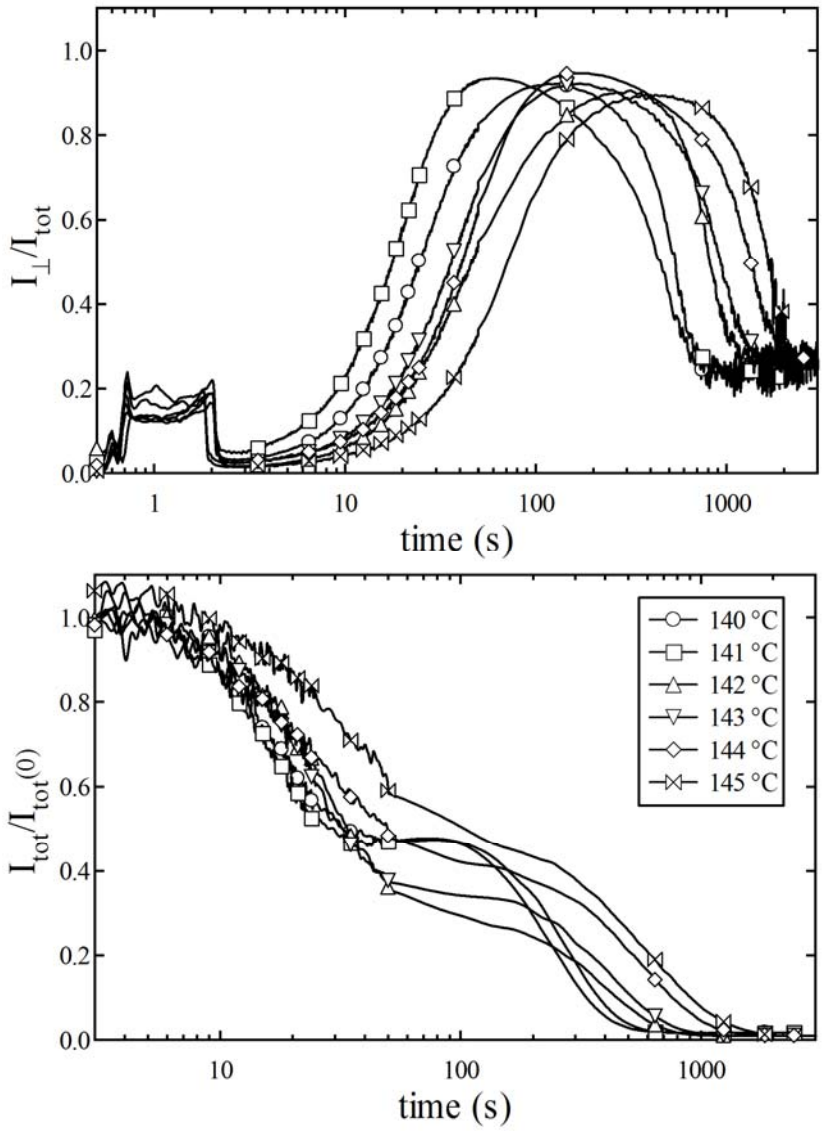

Figure A.3: Intensity through crossed polarizers scaled by total transmitted intensity ($I_\perp/I_{tot}$) and normalized total transmitted intensity ($I_{tot}/I_{tot}(0)$) for L/S_{EP} crystallized at a series of temperatures after shearing (σ_w = 0.102 ± 0.001 MPa) for 1.5 s. At 144 °C and 145 °C the shearing time was 1.3 s. Extruded mass was 100 ± 4 mg.

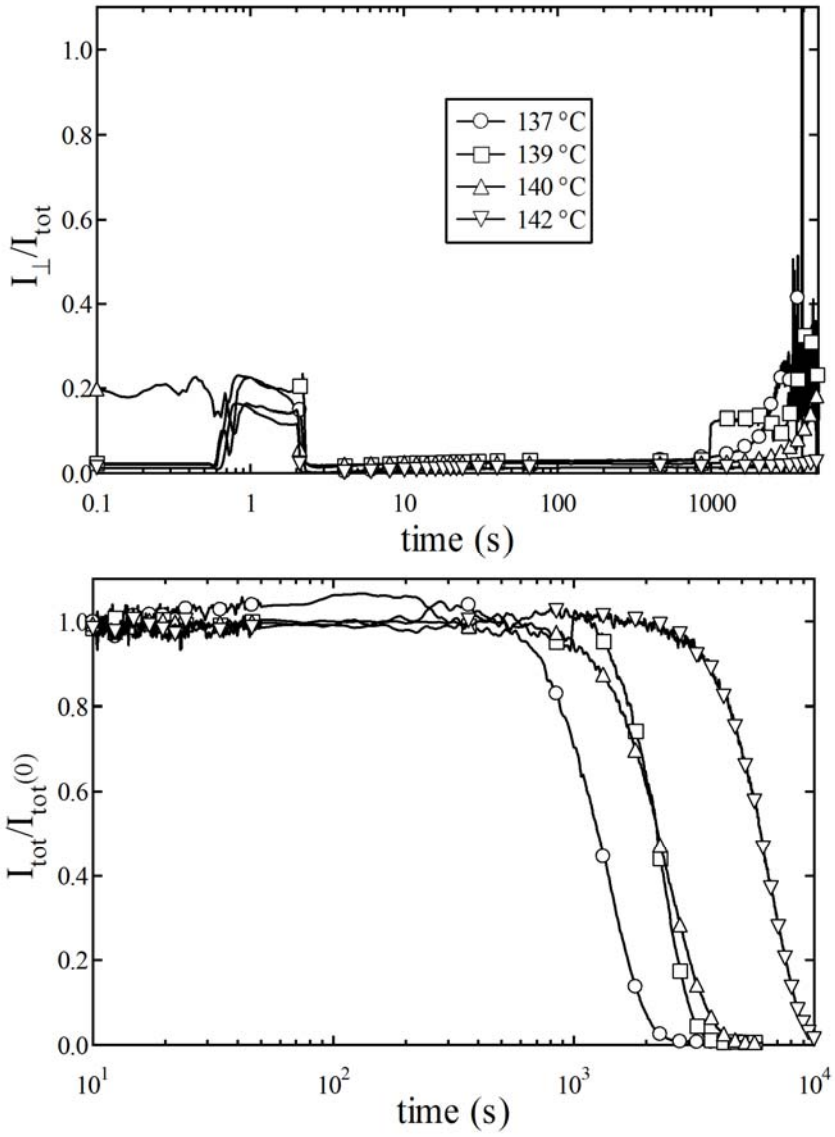

Figure A.4: Intensity through crossed polarizers scaled by total transmitted intensity ($I_\perp/I_{tot}$) and normalized total transmitted intensity ($I_{tot}/I_{tot}(0)$) for L_{EP}/S crystallized at a series of temperatures after shearing (σ_w = 0.10 ± 0.001 MPa). Conditions: 137 °C, t_s = 1.6 s; 139 °C, t_s = 1.6 s; 140 °C, t_s = 1.5 s; 142 °C, t_s = 1.5 s. Extruded mass, w_{ex} = 70 ± 2 mg (except for 140 °C; w_{ex} = 50 mg).

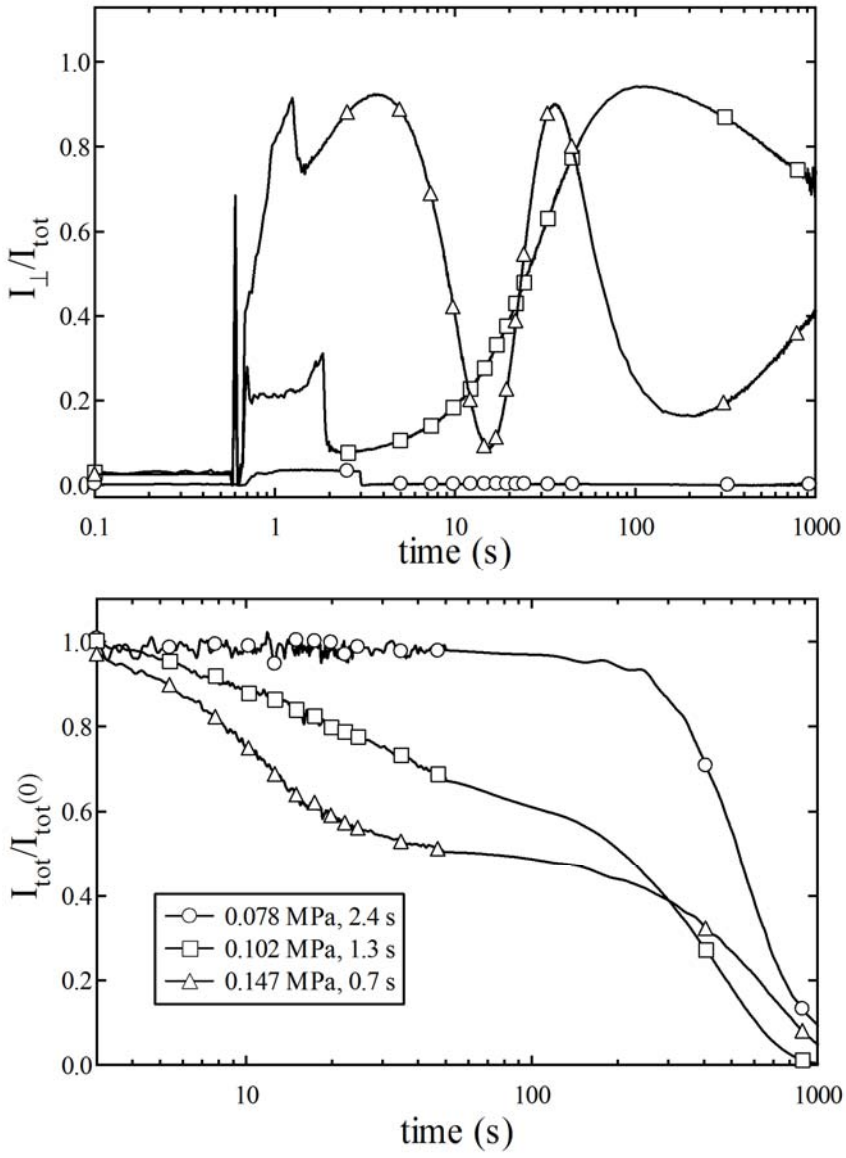

Figure A.5: Intensity through crossed polarizers scaled by total transmitted intensity ($I_\perp/I_{tot}$) and normalized total transmitted intensity ($I_{tot}/I_{tot}(0)$) for L/S_{EP} crystallized at T_c = 145 °C and various shearing stresses. Extruded mass, w_{ex} = 106 ± 2 mg.

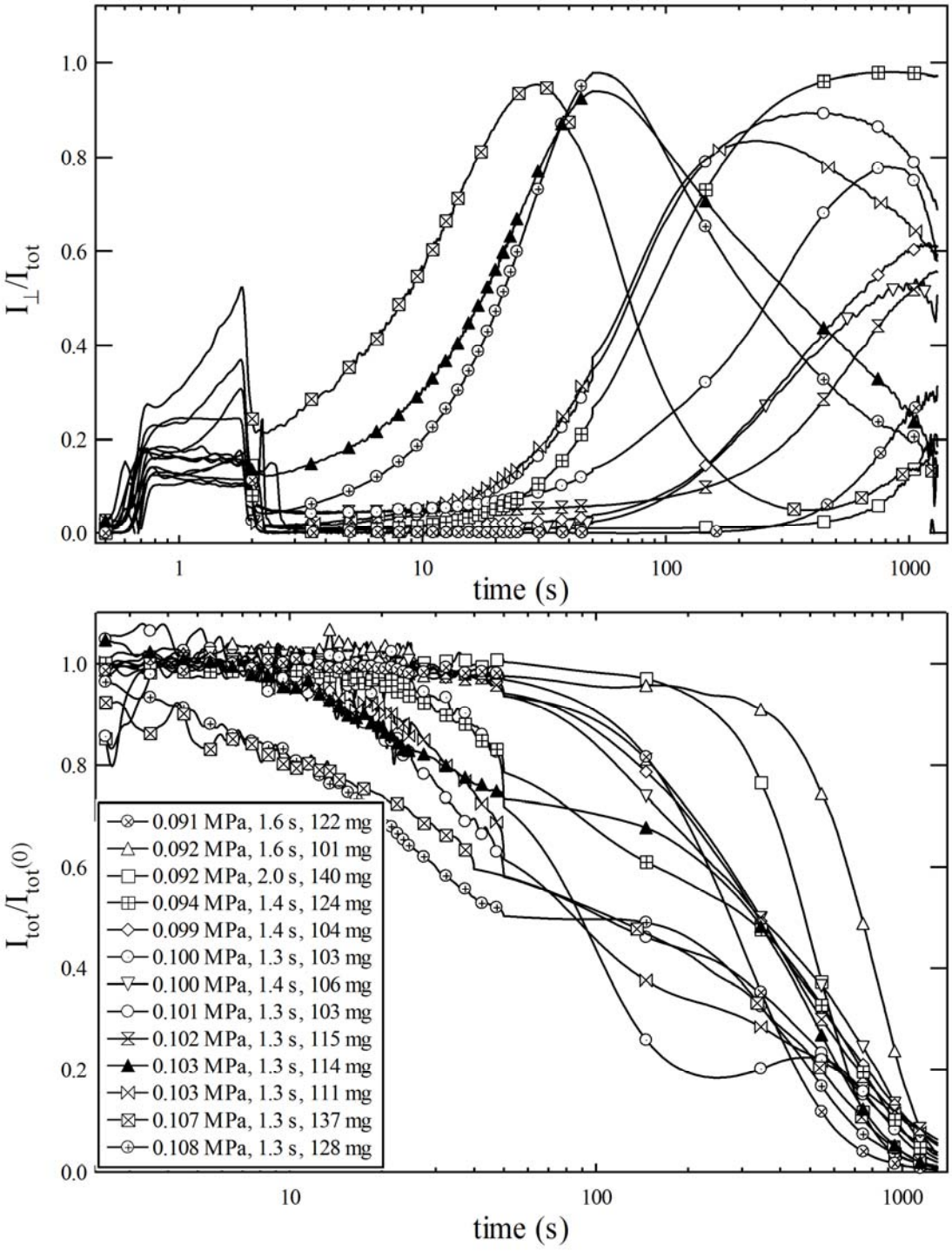

Figure A.6: Summary of intensity through crossed polarizers scaled by total transmitted intensity ($I_\perp/I_{tot}$) and normalized total transmitted intensity ($I_{tot}/I_{tot}(0)$) for L/S_{EP} crystallized at T_c = 145 °C and $\sigma_w \approx 0.10$ MPa. Precise stress, shearing time, and extruded mass indicated on legend.

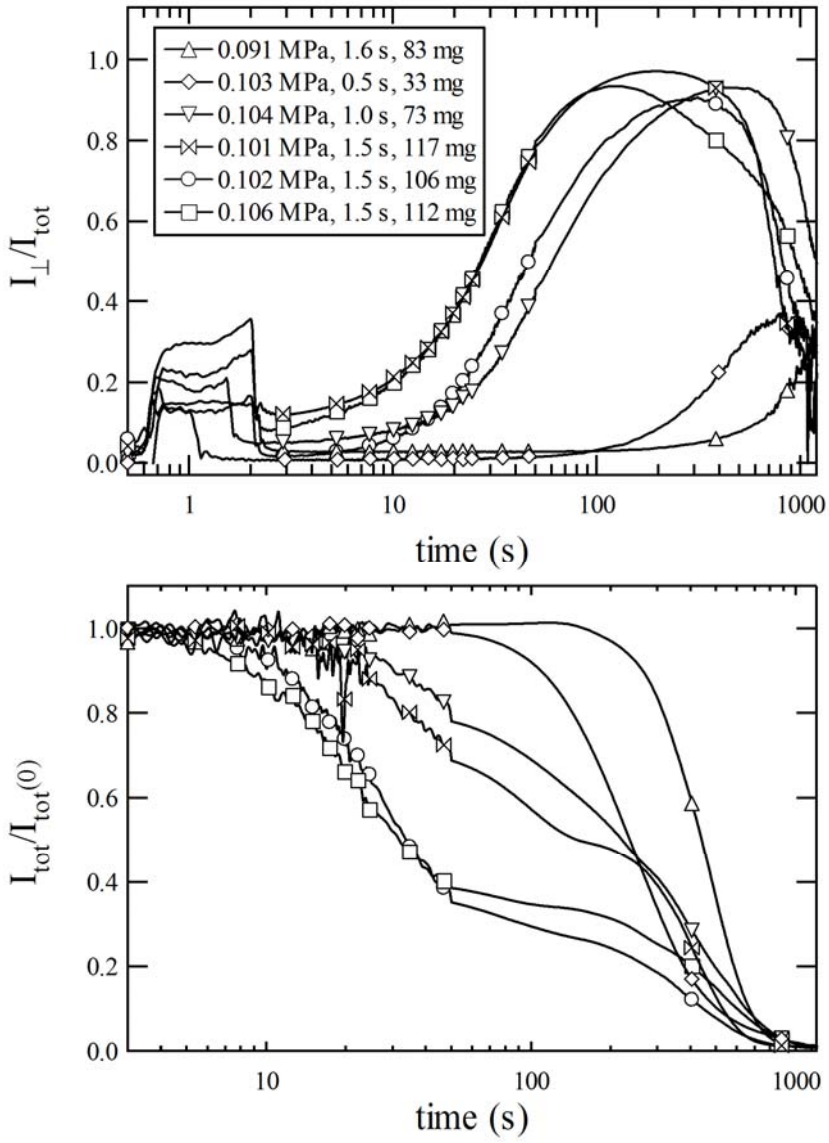

Figure A.7: Summary of intensity through crossed polarizers scaled by total transmitted intensity ($I_{\perp}/I_{tot}$) and normalized total transmitted intensity ($I_{tot}/I_{tot}(0)$) for L/S_{EP} crystallized at T_c = 142 °C and $\sigma_w \approx 0.10$ MPa. Precise stress, shearing time, and extruded mass indicated on legend.

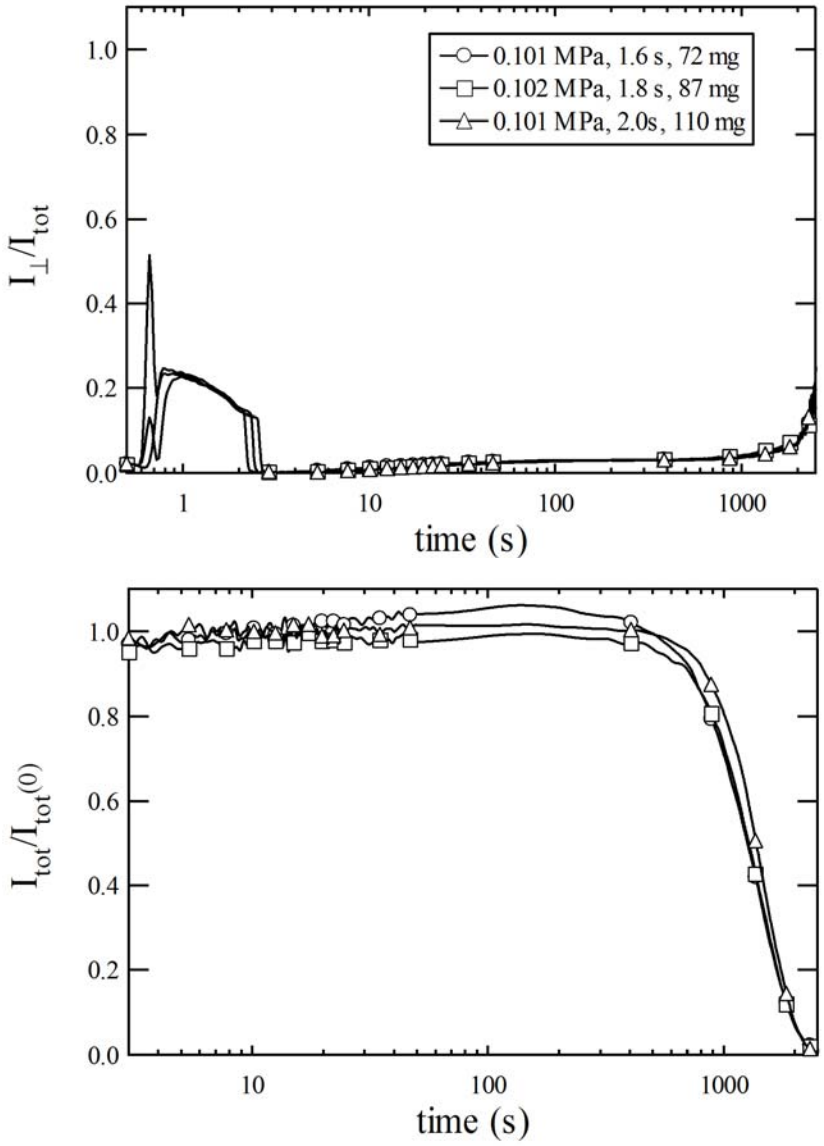

Figure A.7: Summary of intensity through crossed polarizers scaled by total transmitted intensity ($I_\perp/I_{tot}$) and normalized total transmitted intensity ($I_{tot}/I_{tot}(0)$) for L_{EP}/S crystallized at T_c = 137 °C and $\sigma_w \approx 0.10$ MPa. Precise stress, shearing time, and extruded mass indicated on legend.

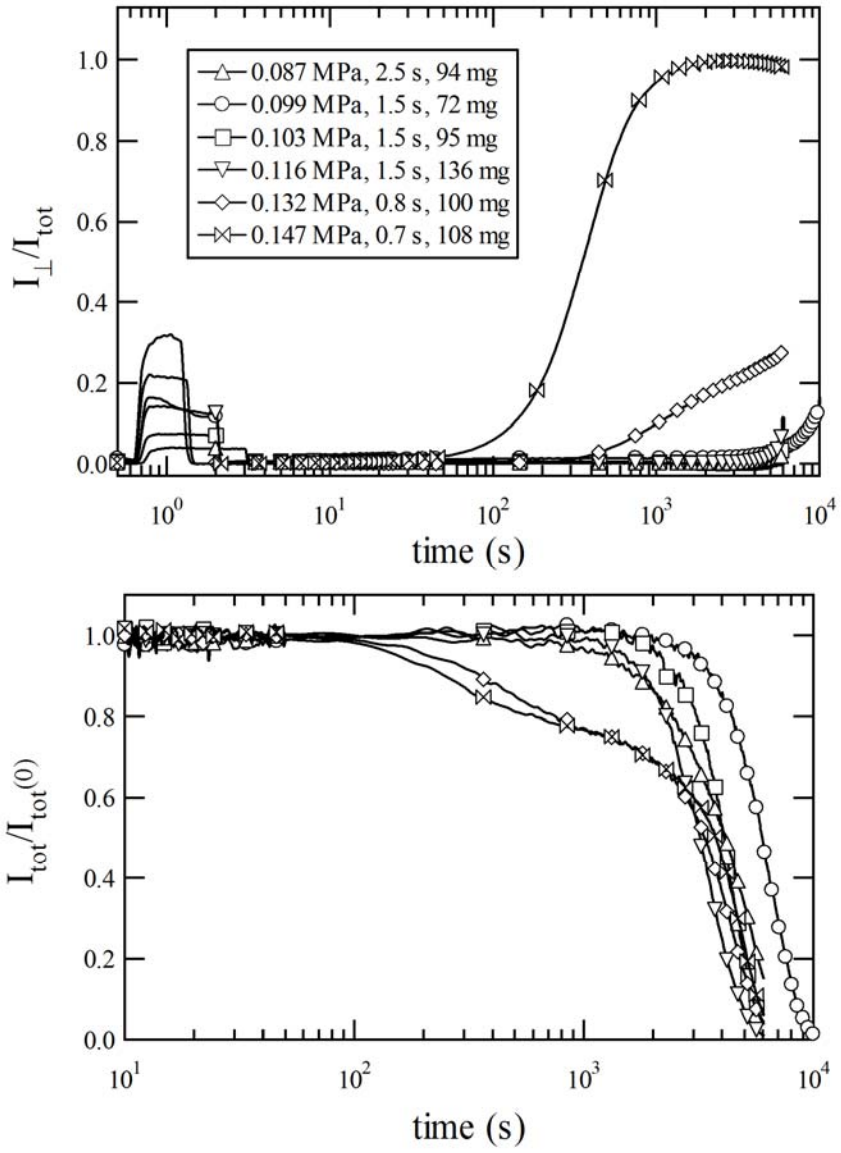

Figure A.9: Intensity through crossed polarizers scaled by total transmitted intensity ($I_{\perp}/I_{tot}$) and normalized total transmitted intensity ($I_{tot}/I_{tot}(0)$) for L_{EP}/S crystallized at T_c = 142 °C and various shearing stresses. Precise stress, shearing time, and extruded mass indicated on legend.